Interface Phenomena in Two-Dimensional Materials

Grenzflächenphänomene in
zweidimensionalen Materialien

Dissertation

zur Erlangung des Doktorgrades
der Naturwissenschaften
(Dr. rer. nat.)

vorgelegt von

Philip Klement

dem Fachbereich 07 der
Justus-Liebig-Universität Gießen

Gießen 2021

Vom Fachbereich 07 Mathematik und Informatik, Physik, Geographie der Justus-Liebig-Universität Gießen als Dissertation angenommen am 05.06.2021.

Erstgutachter: Prof. Sangam Chatterjee, Ph.D.

Zweitgutachter: Prof. Dr. Christian Heiliger

Datum der Disputation: 22.10.2021

Grenzflächenphänomene in zweidimensionalen Materialien

Philip Klement

Die technologischen Entwicklungen des 21. Jahrhunderts zielen darauf Materialien auf molekularer und atomarer Ebene nutzbar zu machen. Einer der Vorreiter ist die Halbleitertechnologie mit der Fertigung von Computerchips, Displays und Datenspeichern. Die fortschreitende Verkleinerung dieser Strukturen und die einhergehende Leistungssteigerung sind wesentliche Grundlagen der digitalen Revolution.

Das Verständnis von Grenzflächen – dem Übergang zweier Materialien – ist entscheidend für das Design und die Leistungsfähigkeit moderner elektronischer Bauelemente. Denn mit kleiner werdenden Strukturen wird der Einfluss der Grenzfläche auf die Materialeigenschaften immer größer. Zweidimensionale (2D) Materialien, wie die Modifikation des Kohlenstoffs Graphen, die quasi nur aus einer Atomlage bestehen, erfahren enormes Forschungsinteresse, da sie die Verkleinerung bis an die Grenze des einzelnen Atoms vorantreiben. Hier bestimmt der Einfluss zwischen Material und Umgebung an der jeweiligen Grenzfläche wesentlich die Materialeigenschaften. Das Verständnis dieses Einflusses und seiner Auswirkungen stehen jedoch noch am Anfang.

Diese Dissertation erweitert das Verständnis der Grenzflächen durch Untersuchungen des Einflusses zwischen 2D Material und der Umgebung.

Publikation 1 zeigt den starken Einfluss der chemischen Umgebung auf die elektronischen Eigenschaften zweidimensionaler Materialien. Die Sauerstoffadsorption an einer einzelnen Lage MoS_2 induziert einen Elektronentransfer über die Grenzfläche.

Auf diesen Erkenntnissen aufbauend zeigt Publikation 2 die Herstellung einer flachen Plattform (Substrat) für 2D Materialien zur Kontrolle der elektronischen Eigenschaften. Die Oberflächendiffusion der Adsorbate dominiert hier den Wachstumsprozess und ermöglicht es, auf einfache Weise, neuartige Nanostrukturen herzustellen.

Publikation 3 erweitert das Spektrum der 2D Materialien um organisch-anorganische Mischkristalle. In dem Material $[C_7H_{10}N]_3[BiCl_5]Cl$ existieren einzelne Lagen und der hier erstmals entdeckte Einfluss der Schichtdicke auf die Emissionswellenlänge könnte ein einfaches Einstellen der Farbe in zukünftigen Beleuchtungs- und Displaytechnologien ermöglichen.

Diese Ergebnisse eröffnen neue Möglichkeiten für die Forschung und deren Anwendungen. Der Einfluss auf die elektronischen Eigenschaften durch ein Substrat ermöglicht es auf innovative Weise interne Grenzflächen für kleinere und leistungsfähigere elektronische Bauelemente zu nutzen.

Interface Phenomena in Two-Dimensional Materials

Philip Klement

The unprecedented technology developments in the 21st century aim at harnessing materials on the molecular or atomic level. Among others, semiconductor technology is pioneering this effort by the fabrication of integrated circuits like computer chips, displays and memory. The continuous downsizing of these structures and resulting performance gains lay the foundation of the digital revolution.

The understanding of interfaces – junctions between materials – is crucial for the design and performance of modern electronic devices. The impact of interfaces on the materials properties increases as structures become smaller. Two-dimensional (2D) materials like Graphene that feature virtually only one atomic layer receive tremendous research interest as they push downsizing to the ultimate limit of atomic thickness. The influence between materials and their environment across interfaces now can even determine the properties. However, the understanding of this influence and its consequences remain in their infancy.

This dissertation extends the understanding of interfaces by investigations of the influence between 2D materials and their environment.

Publication 1 demonstrates the strong impact of the chemical environment on the electronic properties of 2D materials. Oxygen adsorption to a single layer of MoS_2 induces an electron transfer across the interface.

Publication 2 explores these observations further and establishes the controlled fabrication of flat nanometer-sized platforms (substrates) for 2D materials and the manipulation of their electronic properties. Surface diffusion of adsorbates dominates the growth process on these small scales and can be exploited to fabricate novel nanostructures.

Publication 3 extends the spectrum of 2D materials by organic-inorganic mixed crystals. Not deemed feasible before, $[C_7H_{10}N]_3[BiCl_5]Cl$ can be exfoliated to a single layer. The here-discovered novel influence of the crystal thickness on the emission wavelength of the material may enable color tuning in next-generation lighting and display technologies.

These results enable a magnitude of new developments and opportunities in research as well as for their applications. The influence on the electronic properties through substrates allows for the creation of internal interfaces that may be used for smaller and more powerful electronic devices.

Contents

Introduction 1

Two-Dimensional Materials 4

- Transition Metal Dichalcogenides 4
- Layered Organic-Inorganic Perovskites 6

Quasiparticles in Two-Dimensional Materials 8

- Excitons in Transition Metal Dichalcogenides 9
- Excitons in Layered Perovskites 10

Experimental Methods 14

- Sample Preparation 14
- Atomic Layer Deposition 15
- Optical Spectroscopy 17

Summary of Results 22

- Publication 1 22
- Publication 2 22
- Publication 3 23

Conclusion & Outlook 24

Individual Contributions 26

Publications 27

Other Publications 53

References 54

Abbreviations

1D, 2D, 3D	one-, two-, three-dimensional
AFM	atomic force microscopy
ALD	atomic layer deposition
AS-ALD	area-selective atomic layer deposition
CVD	chemical vapor deposition
DOS	density of states
FWHM	full-width-at-half-maximum
PL	photoluminescence
PLE	photoluminescence excitation
PMMA	poly (methyl methacrylate)
QW	quantum well
STE	self-trapped exciton
TRPL	time-resolved photoluminescence
TMDC	transition metal dichalcogenides

Introduction

The understanding of interface-related phenomena is one of the most pressing issues in current solid-state physics. All electronic devices are based on interfaces of different materials, where excitations like charge carriers are separated or transferred across. These interfaces may be formed by different semiconductors in hetero- or homojunctions, *i.e.*, by two different semiconductors, or by the same semiconductor typically featuring different doping levels, respectively. Such interfaces are harnessed as building blocks in diodes, transistors, solar cells, light-emitting diodes, solid-state lasers, and integrated circuits, among other applications. The miniaturization of semiconductor devices continues seemingly limitless: billions of transistors form a modern chip smaller than the size of a fingernail. Typical lateral extensions of transistor structures are just a few nanometer, which renders interfaces ever more important as their number and share in devices increase. The optical and electronic properties of the interface largely determine the functionality and performance of devices. This prompted the German-American Nobel laureate in physics Herbert Kroemer to the concise statement: "The interface is the device.".[1]

Novel phenomena emerge at interfaces and attract considerable research interest. New electronic states form that have no analogue in the bulk of both materials or their constituting atoms. Many fundamental excitations such as electron-hole pairs (excitons) and lattice vibrations (phonons) feature distinct properties in the two-dimensional interface compared to the three-dimensional bulk. Further, structural questions arise: what makes an interface abrupt, and how can that be controlled – if at all? As a consequence, the need for research and understanding is large. The continuing miniaturization demands a better understanding of interface phenomena. On top of that, new organic materials

complement existing inorganic materials by adding new functionalities and design capabilities. This forms a vivid, interdisciplinary scientific research environment at the interface of physics and chemistry.

The aim of this dissertation is to advance the understanding of interface-related phenomena at semiconductor-environment interfaces. More precisely, it features investigations of the interactions between two-dimensional (2D) materials and their chemical and dielectric environments.

Publication 1 demonstrates the strong impact of the chemical environment on the optical and electrical properties of 2D semiconductors. Adsorption of oxygen to a single layer of MoS_2 induces an electron transfer across the semiconductor-molecule interface. The results implicate that the chemical and dielectric environment of 2D materials can be used to manipulate the electronic properties.

Publication 2 elaborates on this idea and demonstrates the fabrication of flat nanometer-sized lateral heterostructures of two dielectrics that can be used as substrates for 2D materials. Surface diffusion of species across the interfaces of the growth areas and the no-growth areas dominates on these length scales and can be exploited to fabricate novel nanostructures.

Publication 3 extends the spectrum of available 2D materials to the emerging class of lower-dimensional organic-inorganic perovskites. Not thought possible before, the one-dimensional semiconductor $[C_7H_{10}N]_3[BiCl_5]Cl$ can be exfoliated to a single layer exhibiting novel exciton physics. This enables a simple process to tune the emission wavelength in these materials by changing the crystal thickness.

The presented results open up a magnitude of opportunities in fundamental research and applications. The flat dielectric substrates can be used to create internal lateral interfaces inside a 2D semiconductor sheet. The novel exciton physics in organic-inorganic perovskites serves as a starting point to explore fundamental structure-property relationships and

may advance next-generation lighting and display technologies with the possibility to easily tune the emission color.

This dissertation is written in cumulative form and organized as follows: First, it gives a short introduction to the investigated materials, important fundamental physical phenomena, and experimental techniques. The main findings are presented in concise abstracts followed by a conclusion and perspective for future works. This is completed by the original publications including a statement of my contributions.

Detailed results have been published in the following three peer-reviewed works:

(1) **P. Klement**, C. Steinke, S. Chatterjee, T. O. Wehling, and M. Eickhoff. Effects of the Fermi Level Energy on the Adsorption of O_2 to Monolayer MoS_2. *2D Materials* **5**, 045025 (2018), DOI: 10.1088/2053-1583/aadc24

(2) **P. Klement**, D. Anders, L. Gümbel, M. Bastianello, F. Michel, J. Schörmann, M. T. Elm, C. Heiliger, and S. Chatterjee. Surface Diffusion Control Enables Tailored-Aspect-Ratio Nanostructures in Area-Selective Atomic Layer Deposition. *ACS Applied Materials & Interfaces* **13**, 19398−19405 (2021), DOI: 10.1021/acsami.0c22121

(3) **P. Klement**, N. Dehnhardt, C.-D. Dong, F. Dobener, S. Bayliff, J. Winkler, D. M. Hofmann, P. J. Klar, S. Schumacher, S. Chatterjee, and J. Heine. Atomically Thin Sheets of Lead-Free 1D Hybrid Perovskites Feature Tunable White-Light Emission from Self-Trapped Excitons. *Advanced Materials* **33**, 2100518 (2021), DOI: 10.1002/adma.202100518

Two-Dimensional Materials

The discovery of graphene with its unique properties has sparked tremendous research interest in two-dimensional (2D) materials.[2–4] Ever after researchers have explored many other layered materials that form stable, atomically thin layers.[5] These include allotropes to graphene such as silicene, and binary or multinary compounds spanning from the insulating hexagonal boron nitride to semiconducting or metallic transition metal dichalcogenides.[5,6] They provide an excellent platform for fundamental research as well as promising applications including fundamental physical phenomena such as polaritons,[7] superconductivity,[8] and charge-density waves,[8] and applications such as water purification,[9] light-emitting diodes,[10] and photovoltaics.[11] In principle, any layered material with only weak van der Waals forces acting between its more strongly-bound layers can be exfoliated.[12] More recent additions to the class of 2D materials are covalent organic frameworks,[13] coordination polymers,[14,15] and layered organic-inorganic perovskites.[16–18]

Transition Metal Dichalcogenides

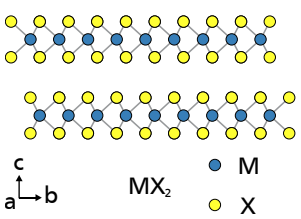

Figure 1 | TMDC Crystal Structure. One metal-atom layer (M) is sandwiched between two chalcogen-atom layers (X).

Semiconducting transition metal dichalcogenides (TMDCs) are presumably the best-studied 2D materials. The stoichiometry is MX_2, and they feature a layered crystal structure with one layer of transition metal atoms *M* sandwiched between two layers of chalcogen atoms *X* (**Figure 1**). *M* can be from groups 4–6, and *X* from group 16. The most-prominent compounds are MoS_2, WS_2, $MoSe_2$, and WSe_2 due to their direct band gaps as single layers.

The metal atom in the center is covalently bonded to six neighboring chalcogen atoms in the top and bottom layers. The complete layer is robust in-plane, and adjacent layers

bond together by weak Van der Waals forces. This allows for the separation of individual layers with one layer being three atoms (*X*–*M*–*X*) thick. One important feature of the crystal structure is the inversion symmetry breaking in uneven numbers of layers: one layer consists of hexagons with metal and chalcogen atoms located in alternating but inequivalent corners (K, K′), which together with the strong spin-orbit coupling gives rise to spin and valley physics.[19]

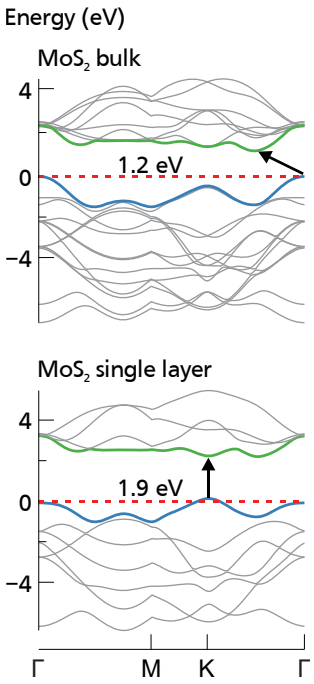

Figure 2 | TMDC Band Structure. Band structure of bulk and single-layer MoS_2 with arrows indicating the fundamental band gap. The figure was adapted with permission from Ref. 21. Copyrighted by the American Physical Society.

TMDCs with group-4 transition metal atoms (Mo, W, *etc.*) are semiconductors with band-gap energies in the red to near-infrared part of the optical spectrum. Their electronic properties strongly depend on the crystal thickness, especially for few layers (**Figure 2**). Generally, bulk TMDCs are indirect-band-gap materials, and become direct-band-gap materials of larger band-gap energies in the single-layer limit.[20,21] The indirect band gap lies between the maximum of the valence band at the Γ-point and the minimum of the conduction band halfway between the Γ-point and the K-points. The band-gap energies increase gradually as the crystal thickness decreases, and the band gap eventually becomes direct in the single-layer limit with valence band maxima and conduction band minima located at the K-points. The bands near the K-points remain almost unchanged, whereas those near the Γ-point change as the crystal thickness changes. This change originates from the orbital character of the bands at the high-symmetry points. In tight-binding approximation, the density of states (DOS) of the conduction band near the K-points is mainly contributed by *d* electron orbitals on the metal atoms that are localized in the *xy*-plane of the TMDC layer, and thus relatively unaffected by interlayer interactions. In contrast, the DOS near the Γ-point originates from the hybridization of p_z electron orbitals on the chalcogen atoms with *d* electron orbitals on the metals atoms, and are rather delocalized in the TMDC layer. The chalcogen atoms are located at the top and at the bottom of the TMDC layer, and are thus strongly affected by interlayer interactions. As a result, the indirect band gap increases significantly as the crystal thickness decreases, and the direct band gap remains relatively unchanged.

The indirect-to-direct band-gap transition in TMDCs is evident as a shift of the photoluminescence to higher energies and a large increase in the photoluminescence quantum efficiency: *e.g.*, the indirect band gap in bulk MoS_2 is $E_{g,bulk} = 1.2$ eV and transitions to a direct band gap of $E_{g,2D} = 1.9$ eV in the single-layer limit. This is accompanied by a 10^4-fold increase in the photoluminescence quantum efficiency.[22]

Layered Organic-Inorganic Perovskites

Layered organic-inorganic perovskites have recently been added to the class of 2D materials. They attract considerable research interests due to their potential for improving the long-term stability of perovskite solar cells while retaining high power-conversion efficiency. In addition, their chemical tunability allows for tailored electronic and optical properties on the one hand, and the investigation of fundamental structure-property relationships on the other.[23,24]

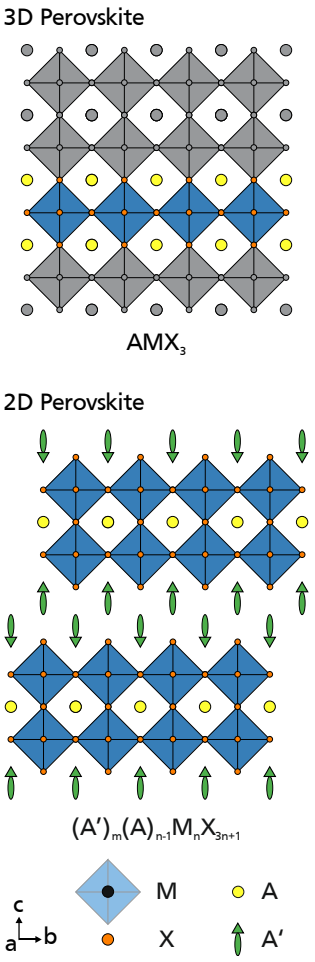

Figure 3 | Perovskite Crystal Structure. Schematic of the 3D and 2D perovskite crystal structure showing two inorganic perovskite layers sandwiched between two organic layers.

In general, 2D organic-inorganic perovskites derive from the three-dimensional (3D) parent perovskite as cut-outs across different crystallographic directions (**Figure 3**). The stoichiometry of 3D parents is AMX_3, where A is a small organic or inorganic cation, M a divalent metal, and X a halogen. The 3D crystal structure involves corner-sharing MX_6 octahedra. The space filling of the cation A between the octahedra imposes rigid structural constraints. 2D perovskites lift those constraints by cutting the 3D perovskite structure into slices. This is achieved by using large organic cations like primary alkyl- or aryl ammonium ions. The stoichiometry of 2D perovskites is $(A')_m(A)_{n-1}M_nX_{3n+1}$, where A' is a mono- or divalent ($m = 1,2$) organic cation that forms a layer between the inorganic $(A)_{n-1}M_nX_{3n+1}$ sheets. The integer n indicates the inorganic layer thickness with $n = 1$ representing 2D, and $1 < n \leq 5$ quasi-2D materials. This crystal structure with stacked alternating organic and inorganic layers resembles that of conventional 2D materials such as TMDCs. Whereas 2D materials bond covalently, 2D perovskites are

more ionic.[25] The flexibility in choosing the constituents provides many opportunities for the preparation of crystal structures with varying physical properties.

Currently known 2D organic-inorganic perovskites are direct-gap semiconductors and the band gap is located at the Γ-point in the band structure. The band-gap energy can be tuned continuously across the optical spectrum by adjusting the composition of the inorganic layer.[16] In contrast to conventional semiconductors, the valence band maximum in 2D perovskites is mainly contributed by the hybridization of *p* electron orbitals on the halides with *s* electron orbitals on the metals atoms, and the conduction band minimum forms from *p* electron orbitals on the metal atoms.[26] The organic cations do not contribute to the band extrema expect when there is a relatively close overlap between energy levels. This leads to complexity in the conduction band structure: the electronic states at the conduction band minimum are degenerate and the incorporation of relatively heavy metal atoms (Pb, Bi, *etc.*) generates significant spin-orbit coupling. This, in principle, allows the manipulation of spin-states.[27]

The freedom in combining many inorganic and organic components in one material offers a rich chemical, structural, and optical tunability. This paves the way to the design of 2D materials as their building blocks can be chosen deliberately. However, reports of single layers similar to those of TMDCs are scarce, despite 2D perovskites exhibiting a similar 2D structure.[16–18] The problems in the investigation of single layers of such 2D perovskites have been manifold:

(1) Early reports suggested that the properties of the single layer and bulk crystal should be the same, because the inorganic layer is effectively isolated by the organic layers.[28]
(2) Strong in-plane covalent bonds, were thought to be mandatory for the formation of single layers.
(3) The technical difficulty of separating and analyzing single layers has led to only few reports.[17]

Quasiparticles in Two-Dimensional Materials

Strong quantum effects and the dielectric confinement in 2D materials give rise to strong Coulomb interactions resulting in extraordinary many-body phenomena such as strongly bound electron-hole pairs, or excitons, and their charged counterparts, trions. The exciton binding-energy is one to two orders of magnitude larger than in conventional semiconductors and is commonly assigned to the range of 150–550 meV.[27,29] Thus, such excitons are stable at room temperature and dominate the optical properties of 2D materials.

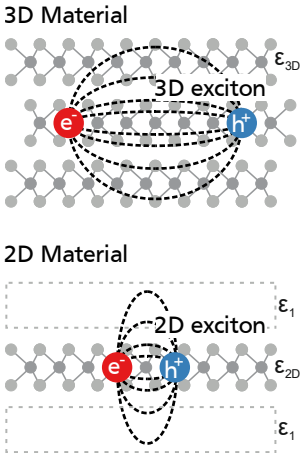

Figure 4 | Dielectric Screening in 2D Materials. Real-space representation of excitons (one electron e^- and one hole h^+) in 3D bulk and single-layer 2D materials. The different dielectric environment is shown by the dielectric constants ε_{3D}, ε_{2D}, and ε_1. The figure was redrawn from Ref. 35.

The electrons and holes forming excitons in 2D materials are strongly confined to one layer and additionally experience altered dielectric screening due to the different dielectric environment compared to the 3D material (**Figure 4**). This has three major implications for the electronic and exciton properties of the material:

(1) Quantum confinement in one dimension increases the quasiparticle band-gap as it shifts the conduction and valence bands by $\hbar^2\pi^2 / 2m_{e,h}d^2$, where d is the confinement length-scale, and $m_{e,h}$ is the electron or hole mass, respectively.[30]

(2) Quantum confinement increases the electron-hole interaction, and thus the exciton binding-energy of the 1s exciton such that

$$E_{b,2D} = 4E_{b,3D} = \frac{2}{\mu}\left(\frac{\hbar}{a_0}\right)^2$$

where μ is the reduced exciton mass, and a_0 is the exciton Bohr radius.[31]

(3) Dielectric confinement in a 2D material with the dielectric constant ε_{2D} occurs when the electric field lines connecting the electron and hole begin to extend outside of the core material into the surrounding material with the dielectric constant ε_1. (Figure 4). This "image-charge effect" increases the Coulomb

interaction in the material, which leads to renormalization of the energy levels increasing the exciton binding-energy and the quasiparticle band-gap energy even further.[32,33] The change of the exciton binding-energy can be approximated by

$$\Delta E_b \approx 2\left(\frac{\epsilon_{2D} - \epsilon_1}{\epsilon_{2D} + \epsilon_1}\right)\frac{e^2}{\epsilon_0 \epsilon_{2D} d} I$$

where ε_0 is the vacuum dielectric constant, and I is a dimensionless quantity.[34]

This set of phenomena and equations provides the framework for understanding confinement effects in 2D materials. The following sections highlight important exciton characteristics in TMDCs and 2D perovskites.

Excitons in Transition Metal Dichalcogenides

The strong Coulomb interaction in TMDCs leads to the formation of excitons as well as higher-order quasiparticles such as trions and biexcitons.[29] The optical spectra of TMDCs show two pronounced resonances denoted as A and B excitons, which originate from the spin-splitting of the valence and conduction bands. The splitting is relatively small in the conduction band and large in the valence band, where it is approximately 0.2 eV in Mo-based and 0.4 eV W-based TMDCs, respectively. The two optical transitions involve holes in the upper-energy and lower-energy spin states.

Excitons in TMDCs have some of both, Wannier-Mott and Frenkel characteristics: the exciton Bohr radius a_0 is rather large, *i.e.*, on the order of 1 nm (Wannier type), while the exciton binding-energy E_b is also large, *i.e.*, in the range of 0.3–0.55 eV (Frenkel type).[29] Quantum confinement and weak dielectric screening in the dielectric environment of the material result in large exciton binding-energies. Screening effects are strong and allow to tune the exciton binding-energy by several hundreds of meV through the surrounding dielectric.[33,35,36] This allows to locally tune the exciton binding-energy and design in-plane electronic interfaces.[37]

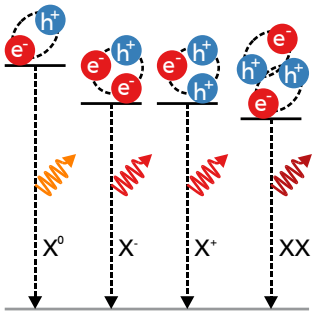

Figure 5 | Quasiparticle Transitions in TMDCs. Excitons, (X^0), trions ($X^{\pm}$) and biexcitons (XX) form from excited electrons (e^-) and holes (h^+). The figure was redrawn from Ref. 38.

Higher-order quasiparticles such as trions and biexcitons form in TMDCs (**Figure 5**). The neutral exciton (one excited electron and one corresponding hole) is the ground state of the charge-neutral system. Positively-charged or negatively-charged trions (one electron and two holes, or two electrons and one hole) form in the presence of excess charge. The trion binding-energy is one order of magnitude smaller than the exciton binding-energy, *i.e.*, on the order of several tens of meV.[38] The trion appears as an additional transition at energies below the neutral-exciton transition. Often, both exciton and trion peaks emerge in the photoluminescence spectra of TMDCs as samples are seldom electrically neutral: defects and adsorbates contribute additional charges to the material.[39] Further, excitons and trions can be tuned by electrostatic gating, *i.e.*, by introducing excess electrons or holes to the material.[40] Thus, the relative intensities of the exciton and trion transitions can serve as a probe for the doping of the material.

Biexcitons composed of two electrons and two holes form when the excitation density of appropriate states is high. Its binding energy is several tens of meV, and it appears as an additional transition at energies below the trion transition.[41] Many more quasiparticles such as dark, spin- and momentum-forbidden, localized and interlayer excitons further extend the versatile exciton landscape.[29]

Excitons in Layered Perovskites

Quantum confinement and the dielectric confinement result in strong Coulomb interaction and the formation of excitons in layered perovskites. Typical optical spectra show one narrow exciton resonance that is well separated from the band-gap energy. The 2D structure forms an ideal quantum well (QW) of one or more inorganic layers sandwiched between two organic barriers. The optical properties of such QWs can be tuned in various ways through the organic and inorganic constituents: Engineering the thickness of the inorganic layer n alters the quantum confinement and the

dielectric confinement effects, consequently changing the band-gap energy E_g and the exciton binding-energy E_b. In $BA_2MA_{n-1}Pb_nI_{3n+1}$ with $n = 1–5$, E_g decreases from 2.42 to 1.85 eV, and E_b from 0.38 to 0.22 eV as the inorganic layer number n increases.[42] Further, adjusting the length of the organic cation during the synthesis tunes the separation between individual QWs, but has negligible effects on the band-gap energy and exciton binding-energy when the cation is longer than 15 Å.[28] However, modifying the dielectric confinement by changing the dielectric constant of the organic cation significantly affects the exciton binding-energy: choosing aromatic amines with a higher dielectric constant (ε_1) instead of alkyl amines with a lower dielectric constant decreases the band-gap energy and exciton binding-energy.[43] Additionally, halide and metal substitution, the cross-sectional area of organic cations, diammonium cations, and mixed-cation systems offer a virtually limitless variety of possibilities to tune the optical properties of layered perovskites.[27]

The nature of excitons in layered perovskites is under debate as they feature some of both, Wannier-Mott and Frenkel characteristics: The exciton binding-energy E_b is large and in the range of 0.15–0.38 eV (Frenkel type), while exciton Bohr radii a_0 in the range of a single to several unit cells have been reported (Frenkel and Wannier-Mott type).[27] Even in a single material, different exciton Bohr radii and consequently both Wannier-Mott excitons and Frenkel excitons have been reported.[27] It is possible that excitons in layered perovskites are intermediates between both categories as it is the case for TMDCs. The softness of the lattice may complicate the matter as it gives rise to dynamic localization effects of excitons as outlined in the next paragraph.

In contrast to inorganic TMDCs, layered perovskites feature a soft lattice with strong electron-phonon coupling that can be directly observed in optical spectra due to the large exciton binding-energy. Many layered perovskites show an additional broad, low-energy feature below the strong, narrow exciton resonance, that is caused by self-trapped

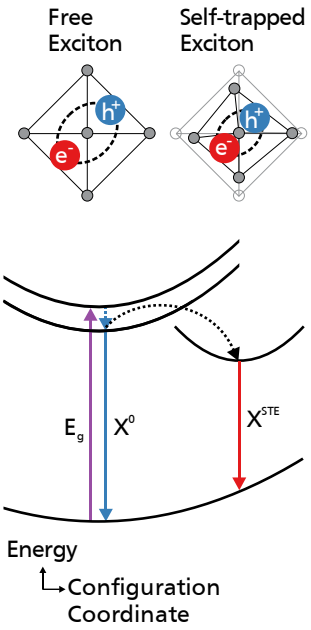

Figure 6 | Exciton Self-Trapping. Schematic and configuration coordinate diagram of self-trapped- (X^{STE}) and free-exciton (X^0) formation. Arrows represent lattice relaxations and optical transitions.

excitons (STE). Self-trapping occurs when excited electrons and holes cause an elastic distortion of the lattice surrounding them (**Figure 6**). Such excitons are trapped by their own lattice deformation potential and localized to a single unit cell. The trapped states are more stable than quasiparticles moving in mobile states while dragging the lattice distortion along. Importantly, STE photoluminescence exhibits a Stokes shift several times of the exciton binding-energy, and the materials have no optical absorption near the STE emission-energy. Another key characteristic may be the existence of a barrier to self-trapping in the form of a narrow photoluminescence with small Stokes shift and a very broad photoluminescence with large Stokes shift. However, the existence of a barrier to self-trapping depends on the dimensionality of the system. It typically vanishes in quasi one-dimensional (1D) systems.[44] Consequently, self-trapping increases from 3D to 2D to the 1D perovskite and the narrow exciton luminescence vanishes.

The softness of the lattice and the strong electron-phonon coupling lead to self-trapping in 2D perovskites. The resulting optical properties can be interpreted within a configuration coordinate model,[45] and the Huang-Rhys factor S quantifies the strength of the electron-phonon coupling.[46] S can be derived from the temperature dependence of the full-width-at-half-maximum (FWHM) of the photoluminescence

$$\mathrm{FWHM} = 2.36\sqrt{S}\hbar\Omega_{\mathrm{e}}\sqrt{\coth\frac{\hbar\Omega_{\mathrm{e}}}{2k_{\mathrm{B}}T}}$$

where Ω_e is the phonon frequency of the excited state.[47] No functional relationship exists between S and STE formation, but large S certainly do facilitate STE formation.[48] Consequently, a large S promotes broadband emission that is of interest for white-light emitters as this characteristic is rare for intrinsic luminescence. However, a large S also leads to a crossing of the excited-state and ground-state curves in the configuration coordinate diagram, which means that excited charge-carriers can recombine nonradiatively by emitting phonons. This nonradiative recombination deteriorates the efficiency of the radiative emission process. As a result, the

strength of the electron-phonon coupling should be just right to enable efficient STE emission. The understanding of the relationship between structure and STE formation in perovskites is just at the beginning.

Experimental Methods

This chapter covers the most important experimental techniques that I used within the scope of this thesis. It is divided into three sections: the first section covers the preparation of atomically thin 2D materials used for the experiments in Publication 1 and Publication 3. The following section covers the preparation of thin films by atomic layer deposition (ALD) used for the experiments in Publication 2. Finally, the last section covers the measurements of the optical properties used for the experiments in Publication 1 and Publication 3. It includes a brief description of linear absorption measurements and reflectance spectroscopy, continuous-wave photoluminescence (PL) spectroscopy, time-resolved photoluminescence (TRPL) spectroscopy and photoluminescence excitation (PLE) spectroscopy.

Sample Preparation

2D materials featuring a layered crystal structure have been investigated in Publication 1 and Publication 3. Monolayer and ultrathin samples can be produced by mechanical exfoliation of bulk single-crystals.[3] In a typical procedure, a small bulk crystal of approximately 1 mm^2 is placed on the sticky side of blue wafer-processing tape. Then, the sticky side with the bulk crystal on it is folded and unfolded several times cleaving the bulk crystal. This produces pristine crystal surfaces that are free of contamination. The tape is pressed on the surface of a heavily *p*-type doped Si substrate with a 275 nm-thick oxide-layer. For MoS_2, mild heating to 100 °C for 60 s on a hot plate facilitates the adhesion of individual layers to the substrate.[49] The tape is subsequently removed leaving a variety of samples of different thicknesses attached to the substrate.

Ultrathin samples are identified by optical contrast imaging as the contrast between the sample and the substrate changes as a function of the sample thickness.[50] The thickness is confirmed by atomic force microscopy (AFM, AIST-NT SmartSPM 1000). Non-contact tapping-mode is used to avoid sample damage from the tip. For MoS_2, the thickness is additionally confirmed by Raman and PL spectroscopy as the relations between the phonon frequencies, the PL intensity and the sample thickness are well-known.[22,51] Lateral sizes of MoS_2 single- and few-layer samples range from 5–10 µm, whereas ultrathin 2D perovskite samples featured lateral sizes of less than 1 µm, which reflects the mechanically-brittle structure originating from the comparably soft crystal-lattice.

Atomic Layer Deposition

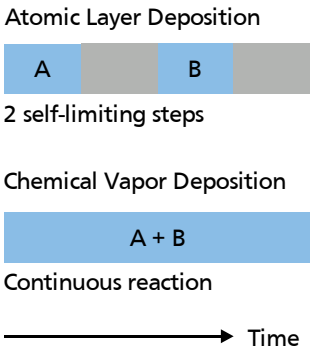

Figure 7 | Distinction of ALD & CVD. Whereas ALD features two self-limiting precursor-reaction-steps, CVD operates continuously with both precursors A + B.

Atomic layer deposition (ALD) is a thin-film deposition technique which adds atoms or small inorganic compounds sequentially (*i.e.*, layer-by-layer) to a substrate. It is a strongly modified chemical vapor deposition (CVD) process, which relies on the cyclic and alternate exposure of the substrate to two or more precursors (**Figure 7**). Those precursors react with the surface in a self-limiting reaction forming a thin film.

Surface Reaction Mechanism. In a typical ALD process, the substrate is sequentially exposed to two gaseous precursors A and B. First, precursor A is inserted into the reactor, and the precursor molecules react with the reactive sites on the substrate surface. The reaction stops once all reactive sites are occupied making this step self-limited. Excess precursor molecules and by-products are purged from the reactor by inert gas. Then precursor B is inserted into the reactor and reacts with precursor A on the substrate surface forming the target compound. Importantly, the surface of the product is active to the reaction mechanism of precursor A. The reaction stops once all precursor A molecules have reacted making this step self-limited as well. In the final step, excess precursor molecules and by-products are purged from the reactor by inert gas. Repeating the alternate exposure of A and B

deposits a thin film of the target compound on the substrate. Those four steps constitute an ALD reaction cycle, and the precursor exposure steps are referred to as half-reaction cycles.[52] This cyclic exposure ensures atomic-level thickness-control as only one layer of precursor molecules forms on the substrate in each half-reaction, subsequently reacting with each other forming one layer of the target compound. The details of the reaction mechanisms in the two half-reactions depend on the specific ALD process, *i.e.*, on the precursors, the reactor temperature and the substrate surface chemistry.

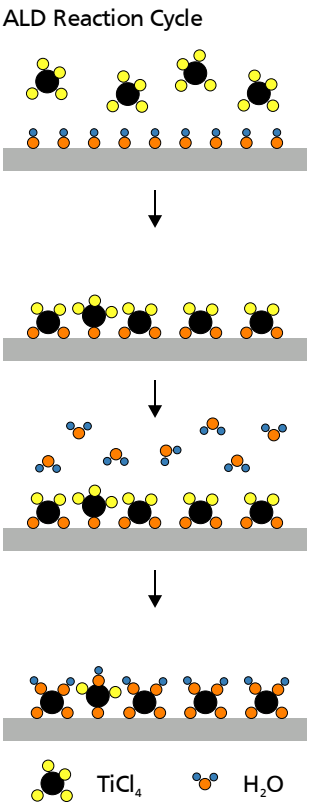

Figure 8 | TiO_2 ALD Process. Reaction cycle of the TiO_2 deposition from $TiCl_4$ and H_2O in 4 steps. The figure was redrawn from Ref. 53.

Titanium oxide (TiO_2) was selected for the experiments in Publication 2 because of its high dielectric constant and its chemical and physical stability. Ultimately, the goal of these experiments is to extrinsically manipulate the electronic properties through dielectric screening effects (*cf.* page 8). The synthesis of TiO_2 from titanium tetrachloride ($TiCl_4$) and water (H_2O) is a well-known ALD process (**Figure 8**).[53,54] During the first half-reaction, $TiCl_4$ adsorbs to the substrate and reacts with one surface hydroxyl group forming titanium trichloride ($TiCl_3$) and gaseous hydrochloric acid (HCl). Excess $TiCl_4$ and HCl are purged from the reactor, and the surface is exposed to H_2O. During the second half-reaction, H_2O reacts with three chlorine ligands forming hydroxlated TiO_2 and gaseous HCl. Excess H_2O and HCl are purged from the reactor, and the ALD reaction cycle begins anew.

Area-Selective ALD on Polymers. The application of ALD in self-aligned fabrication schemes for modern microelectronics mandates that the deposition is limited to specific areas.[55] Area-selective atomic layer deposition (AS-ALD) implements spatial control of the growth area by locally tailoring the surface chemistry. Typically, parts of the substrate are either activated, *i.e.*, made reactive to the chemistry of the ALD process, or deactivated, *i.e.*, made inert to the chemistry of the ALD process. Thus, a substrate surface in AS-ALD features at least two materials with distinct surface chemistries, and the ALD process is selective to one of these materials.

One possibility for area deactivation is the use of poly (methyl methacrylate) (PMMA) as in the experiments in Publication 2.

It is a well-established polymer that allows to readily generate nanometer-sized patterns on a substrate. It features methyl (−CH_3) and carbonyl (−C=O) groups on the surface in contrast to hydroxlated (−OH) surfaces in conventional ALD processes. This makes PMMA unreactive towards most ALD chemistries as precursor adsorption is at least inhibited or even blocked.[56] However, precursor adsorption in the form of physisorption is always possible, and adsorbed species diffuse on the surface until they reach a reactive site and chemisorb. The surface diffusion may occur during either half-reaction cycle: precursor A may diffuse on the substrate during the first half-cycle, and the target compound may diffuse during the second half-cycle. An exact differentiation remains difficult.[57] Publication 2 investigates this surface diffusion process in AS-ALD.

Optical Spectroscopy

Linear Absorption Spectroscopy. Absorption is the conversion of light (photon) energy into other forms of energy like heat, chemical energy or the excitation of particles into higher states. In semiconductors, linear absorption measurements access dipole-allowed transitions from occupied states in the valence band to unoccupied states in the conduction band. The intensity of light I propagating in a medium in this fundamental absorption process decreases exponentially with increasing distance d according to the Beer-Lambert law

$$I = I_0 \, \mathrm{e}^{-\alpha d}.$$

Here, α is the extinction coefficient, and d denotes the sample thickness of the bulk material.[30] Note that the law may be questioned for 2D systems as the conditions for its validity hold no longer. Among others, radiative coupling and a thickness-dependent refractive index complicate the absorption process.[58]

Extinction α comprises both the above-mentioned absorption and the scattering of light (α_{scat}). The absorption coefficient

(α_{abs}) is a function of the photon energy: it is small below and large above the band-gap energy. Usually, scattering is neglected because it is weak and approximately wavelength-independent. The absorption A may be calculated from the transmittance T and reflectance R of the sample according to $1 = A + T + R$ by either measuring the transmittance of the sample neglecting reflectance, or measuring the reflectance of the sample on an opaque substrate neglecting transmittance. The measurements are always three-step processes: first, a background measurement with no light source and sample corrects for stray light in the experimental setup. Second, a reference measurement gives the 100 % baseline. This corresponded to the experimental setup without the sample in transmission measurements, and to a polished silicon surface or a metallic/dielectric mirror in reflection measurements. Finally, the sample transmission or reflection spectrum is measured, and A and α_{abs} are calculated from the equations above. In most cases, the product αd was evaluated as the exact sample thickness was unknown, and this is the relevant quantity for 2D systems.

Photoluminescence Spectroscopy. Photoluminescence (PL) is the light emission of a material after photoexcitation. Photon absorption creates an electron-hole pair by exciting an electron from an occupied state in the valence band to an unoccupied state in the conduction band leaving a hole. Various energy- and momentum-relaxation processes occur, and both charge carriers move to the respective band extrema. Finally, electron and hole recombine emitting a photon. Thus, PL probes occupied states and allows comprehensive insight into the electronic structure of the material. **Time-Resolved Photoluminescence Spectroscopy** (TRPL) adds information on the relaxation dynamics of the emissive state by probing the luminescence decay-time τ, whose reciprocal is the sum of the reciprocals of the radiative and non-radiative decay-times.[30] It can be used to identify individual radiative recombination channels from their decay behavior. If the external quantum-efficiency is known, the radiative and non-radiative decay-times can be calculated.[30] **Photo-luminescence Excitation Spectroscopy** (PLE) monitors the

PL intensity of a certain luminescence feature as a function of the excitation energy. It provides an absorption-like spectrum with peaks at energies of strong absorption. However, it is not identical with absorption as it includes other processes like the relaxation of excited carriers to the respective band extrema.[30] A comparison of PLE and absorption spectra yields information on the coupling between absorbing and emitting states. Further, PLE allows to measure higher states above the band-gap energy that cannot be accessed by linear absorption spectroscopy due to the large absorption coefficient. It is also very useful when the substrate is opaque in the spectral region of interest or the absorption coefficient is very low like in single quantum wells.

Experimental Setups. The optical measurements performed within the scope of this thesis utilize different experimental setups, each customized to the specific requirements of the sample and spectroscopic technique. This section presents the mutual concept of all setups instead of describing each experimental setup separately. The latter can be found in the experimental sections of the publications. All samples investigated by optical spectroscopy in Publication 1 and Publication 3 feature very small dimensions, *i.e.*, lateral dimensions of 0.5–10 μm and thicknesses of 0.6–250 nm. This requires experimental setups with small spot sizes to selectively probe a single sample, optical feedback to monitor the position of the sample, and a positioning system to align the laser spot and the sample. The experimental setup may be divided into three parts: excitation, microscope, and detection (**Figure 9**).

The excitation sources differ depending on the sample requirements and spectroscopic technique. Linear absorption spectroscopy in Publication 3 utilizes a combined deuterium and tungsten lamp delivering a continuous spectrum from 280–825 nm (4.4.–1.5 eV). PL spectroscopy in Publication 1 and Publication 3 uses a continuous-wave 488 nm (2.5 eV) Ar-ion laser and a 266 nm (4.7 eV) frequency-quadrupled Nd:YAG laser, respectively. TRPL spectroscopy in Publication 3 employs a tunable titanium-sapphire laser

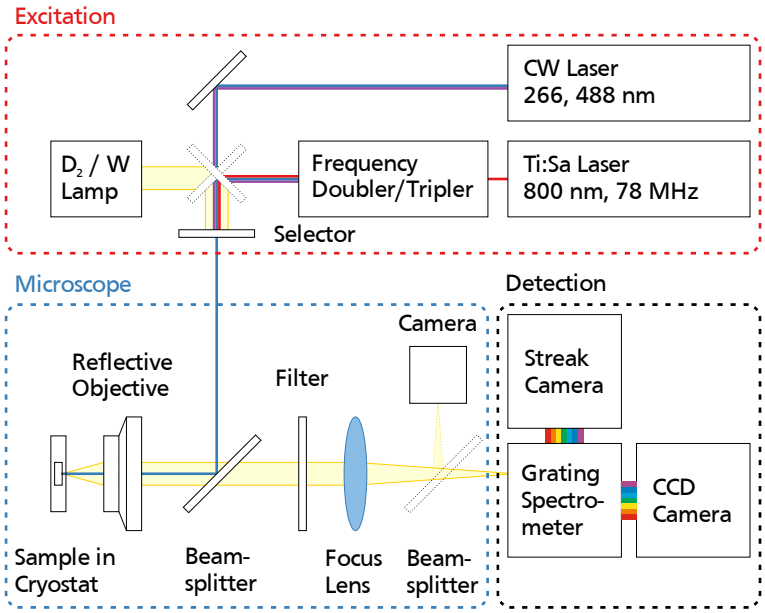

Figure 9 | Optical Spectroscopy Setups. Schematic of the self-build setups for absorption, PL and TRPL spectroscopy. This assembly enables measurements with high spatial, spectral and temporal resolutions over a broad range of excitation energies.

emitting approximately 100 fs long pulses at 800 nm (1.55 eV) and 78 MHz repetition rate. The excitation energy increases through a combined frequency-doubling and frequency-tripling unit delivering pulses at 266 nm (4.7 eV). PLE spectroscopy uses a titanium-sapphire regenerative amplifier at 5 kHz repetition rate and 50 fs pulse length in combination with an optical parametric amplifier delivering an excitation range from 240–650 nm (5.2–1.9 eV).

The excitation light is coupled into a self-build microscope with a beam splitter customized to the excitation wavelength. Alternatively, a small (5 x 5 mm) Al mirror is used to avert wave interference from the front and back surfaces of the beam splitter. However, this may increase the complexity of operation as the field-of-view is partly shadowed. The excitation light is focused through a reflective 36-fold Schwarzschild objective into an almost diffraction-limited spot of 1 µm diameter. The beam path is confocal, which means that the excitation and detection beam paths have the same foci. The use of exclusively reflective optics allows low power losses over the entire excitation range and low temporal pulse distortions. The microscope benefits from the long working distance of the objective (8.6 mm), which allows mounting the sample in a He-flow cryostat. The temperature ranges from 3.6–300 K. The sample signal is collected in backscattering geometry by the same objective and focused

with an achromatic lens on the entrance slit of the spectrometer. The lens images the sample surface onto the entrance slit and is the sole transmissive optical component of the microscope. An optional beam splitter between the lens and the spectrometer couples the light to an imaging camera. This allows to monitor the relative positions of the excitation light-spot and the sample. A motorized stage below the cryostat allows to align the sample with the excitation light-spot with 4 nm precision.

The detection consists of a spectrometer for selecting a narrow band of wavelengths and a subsequent charge-coupled device camera for detection. The spectrometer is a standard Czerny-Turner-type model with different diffraction gratings, each optimized to a spectral range and required spectral resolution. In linear absorption, PL, and PLE spectroscopy, the signal is detected by a Si charge-coupled device camera with high sensitivity that allows the detection of low levels of light. The camera is thermoelectrically-cooled to −60 °C to reduce the dark current and noise level. In TRPL spectroscopy, the signal is recorded by a streak camera equipped with a S20 photocathode yielding a time resolution better than 1 ps (Hamamatsu C10910 and Orca Flash).

Summary of Results

Publication 1

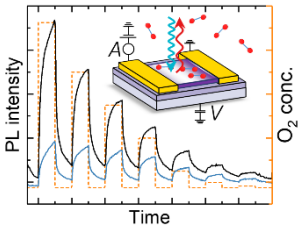

Ultrathin two-dimensional materials offer large surface-to-volume ratios that make them ideal for sensing applications as interactions on the surface significantly change the materials properties. However, most interaction mechanisms remain unclear, even for common environments such as O_2. In this work, we investigate O_2 adsorption on single-layer MoS_2 and the influence of the Fermi-level energy in this process. We find an increase of the photoluminescence intensity and a reduction of the electrical conductivity upon O_2 adsorption, and identify an electron transfer from MoS_2 to O_2. Further, we show that the adsorption process can be manipulated by the Fermi-level energy, and only occurs if free carriers are available in the conduction band of MoS_2. Our work highlights the strong interactions across the 2D material-gas interface and offers new opportunities to manipulate materials properties.[59]

Publication 2

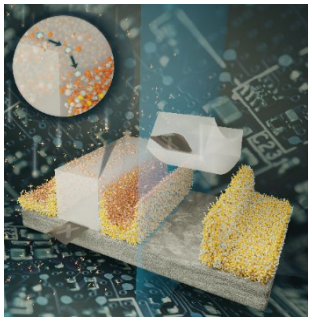

Area-selective atomic layer deposition is a key technology for modern microelectronics as it eliminates alignment errors inherent to conventional approaches by enabling material deposition only in specific areas. Typically, the selectivity originates from surface modifications of the substrate that allow or block precursor adsorption. The control of the deposition process currently remains a major challenge as the selectivity of the no-growth areas is lost quickly. Here, we show that surface modifications of the substrate strongly manipulate the surface diffusion. The selective deposition of TiO_2 on poly (methyl methacrylate) and SiO_2 yields localized

nanostructures with tailored aspect-ratios. Controlling the surface diffusion allows to tune such nanostructures as it boosts the growth rate at the interface of the growth and no-growth areas. Kinetic Monte-Carlo calculations reveal that species move from high to low diffusion areas. Further, we identify the catalytic activity of $TiCl_4$ during the formation of carboxylic acid on poly (methyl methacrylate) as the reaction mechanism responsible for the loss of selectivity, and show that process optimization leads to higher selectivity. Our work enables the precise control of area-selective atomic layer deposition on the nanoscale, and offers new strategies in area-selective deposition processes by exploiting surface diffusion effects.[60]

Publication 3

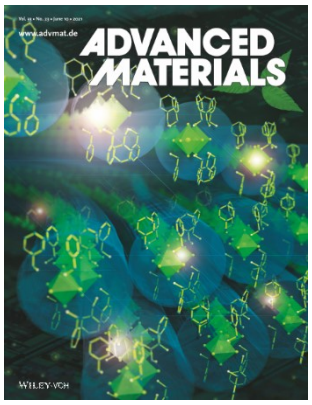

Low-dimensional organic-inorganic perovskites synergize the virtues of two unique classes of materials featuring intriguing possibilities for next-generation optoelectronics: they offer tailorable building blocks for atomically thin, layered materials while providing the enhanced light-harvesting and -emitting capabilities of hybrid perovskites. Here, we go beyond the paradigm that atomically thin materials require in-plane covalent bonding and report single layers of the one-dimensional organic-inorganic perovskite $[C_7H_{10}N]_3[BiCl_5]Cl$. Its unique 1D-2D structure enables single layers and the formation of self-trapped excitons which show white-light emission. The thickness dependence of the exciton self-trapping causes an extremely strong shift of the emission energy. Thus, such two-dimensional perovskites demonstrate that already 1D covalent interactions suffice to realize atomically thin materials and provide access to unique exciton physics. These findings enable a much more general construction principle for tailoring and identifying two-dimensional materials that are no longer limited to covalently bonded 2D sheets.[61]

Conclusion & Outlook

This dissertation successfully advances the understanding of interface-related phenomena at the semiconductor-environment interface. The results pave the way to creating and investigating internal lateral interfaces in 2D materials.

Publication 1 demonstrates the strong impact of the chemical environment on the optical and electrical properties of two-dimensional semiconductors. The electron-transfer from MoS_2 to O_2 across the 2D material-gas interface and the resulting change in dielectric screening offer new opportunities to manipulate materials properties and possibly create internal lateral interfaces.

Publication 2 carries this idea forward and demonstrates the fabrication of flat, nanometer-sized heterostructures of two dielectrics. Surface diffusion of species across the interface of the growth and no-growth areas in area-selective ALD emerges on small scales and dominates the growth process. It can be exploited to fabricate novel nanostructures that serve as substrates to 2D materials.

Publication 3 expands the universe of two-dimensional materials by the emerging and promising class of lower-dimensional organic-inorganic perovskites. They offer excellent semiconductor properties while increasing the stability compared to conventional perovskites. Not thought possible before, $[C_7H_{10}N]_3[BiCl_5]Cl$ can be exfoliated to a single layer exhibiting novel exciton physics. This phenomenon may enable a simple way to tune the emission color in next-generation lighting technologies.

The presented results open up a magnitude of new developments and opportunities in research as well as for their applications. The flat dielectric hetero-substrates can be used to create internal lateral interfaces inside 2D

semiconductors thereby circumventing the problem of lattice mismatch, which usually hinders device performance (**Figure 10**).[33,62] Our preliminary studies on dielectric screening effects in monolayer WSe_2 on such SiO_2-TiO_2 hetero-substrates reveal the intended band-gap variation as well as a distinct exciton physics with spin-split excitons experiencing different dielectric screening.[63] The latter is highly remarkable and underlines the richness of scientific opportunities in this approach.

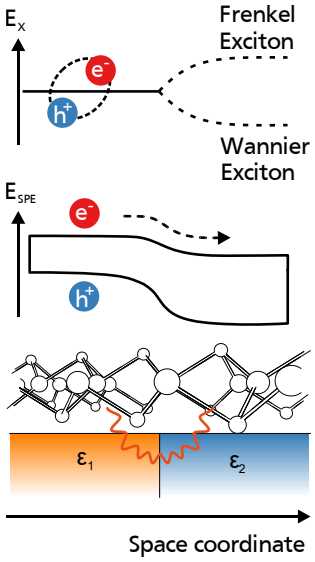

Figure 10 | Internal Interface Creation. Dielectric screening effects from the hetero-substrate with the dielectric constants $\varepsilon_1 > \varepsilon_2$ create an internal electronic interface in the 2D material. Additionally, the single- and two-particle energy landscapes are shown.

The next key result is the comprehensive characterization of internal lateral interfaces in inorganic 2D semiconductors such as TMDCs on dielectric hetero-substrates. In principle, carriers can be optically injected on one side of the interface and diffuse across the lateral interface.[64] These currents can be monitored through ultrafast reflection changes of the material by imaging a line across the lateral interface in a pump-probe experiment. The band alignment of the interface as well as the nature of diffusing (quasi-)particles (charge carriers or excitons) are central scientific questions. Further, the transport across the lateral interface can be restricted by an appropriate hetero-substrate: the width of one dielectric strap with the dielectric constant ε_2 bordered on both sides by another dielectric with $\varepsilon_1 > \varepsilon_2$ defines a transport channel for (quasi-)particles in the 2D semiconductor. Reducing the width could lead to additional quantum mechanical states similar to those observed in semiconductor quantum wells. Even further, dielectric quantum dots could offer the possibility of controlling the exciton motion similar to an exciton funnel and manipulate the emission of light.[65]

Lower-dimensional organic-inorganic perovskites add a multitude of opportunities as their constituents can be chosen deliberately. Uniaxial covalent bonds as in $[C_7H_{10}N]_3[BiCl_5]Cl$ offer the potential for 1D conductance without using hetero-substrates. Additionally, they exhibit self-trapped excitons whose fundamental structure-property relationships have been only briefly explored but offer great potential for next-generation lighting and display technologies.

Individual Contributions

This section emphasizes my contributions to the publications.

Publication 1

M. Eickhoff and I conceived the experiments. I developed and implemented the MoS_2 field-effect transistor fabrication and the electrical-optical experimental design. I performed the Raman and photoluminescence spectroscopy and conductivity measurements, and analyzed the results. I discussed the results with all co-authors and co-wrote the bulk of the manuscript. Finally, I was responsible for the publication process.

Publication 2

S. Chatterjee and I conceived the experiments. I fabricated the samples by electron-beam lithography and performed the X-ray reflectivity, infrared spectroscopy, and atomic force microscopy measurements, assisted by D. Anders, M. Bastianello, and L. Gümbel. I analyzed and interpreted the results. I discussed the results with all co-authors and co-wrote the bulk of the manuscript. Finally, I was responsible for the publication process.

Publication 3

J. Heine and S. Chatterjee conceived the study. I developed and implemented the experimental design for the nanoscale optical experiments. I prepared the ultrathin samples and performed the atomic force microscopy, absorption, reflectance, photoluminescence, time-resolved photo-luminescence and Raman spectroscopy measurements. S. Chatterjee and I analyzed and interpreted the results. I discussed the results with all co-authors and co-wrote the bulk of the manuscript

Publications

Publication 1

Effects of the Fermi Level Energy on the Adsorption of O_2 to Monolayer MoS_2

Philip Klement, Christina Steinke, Sangam Chatterjee,
Tim O. Wehling, and Martin Eickhoff

2D Materials **5**, 045025 (2018), DOI: 10.1088/2053-1583/aadc24

2D Materials

ACCEPTED MANUSCRIPT

Effects of the Fermi level energy on the adsorption of O_2 to monolayer MoS_2

To cite this article before publication: Philip Klement *et al* 2018 *2D Mater.* in press https://doi.org/10.1088/2053-1583/aadc24

Manuscript version: Accepted Manuscript

Accepted Manuscript is "the version of the article accepted for publication including all changes made as a result of the peer review process, and which may also include the addition to the article by IOP Publishing of a header, an article ID, a cover sheet and/or an 'Accepted Manuscript' watermark, but excluding any other editing, typesetting or other changes made by IOP Publishing and/or its licensors"

This Accepted Manuscript is **© 2018 IOP Publishing Ltd**.

During the embargo period (the 12 month period from the publication of the Version of Record of this article), the Accepted Manuscript is fully protected by copyright and cannot be reused or reposted elsewhere.
As the Version of Record of this article is going to be / has been published on a subscription basis, this Accepted Manuscript is available for reuse under a CC BY-NC-ND 3.0 licence after the 12 month embargo period.

After the embargo period, everyone is permitted to use copy and redistribute this article for non-commercial purposes only, provided that they adhere to all the terms of the licence https://creativecommons.org/licences/by-nc-nd/3.0

Although reasonable endeavours have been taken to obtain all necessary permissions from third parties to include their copyrighted content within this article, their full citation and copyright line may not be present in this Accepted Manuscript version. Before using any content from this article, please refer to the Version of Record on IOPscience once published for full citation and copyright details, as permissions will likely be required. All third party content is fully copyright protected, unless specifically stated otherwise in the figure caption in the Version of Record.

View the article online for updates and enhancements.

This content was downloaded from IP address 134.176.16.224 on 24/08/2018 at 10:10

IOP Publishing 2D Materials
Journal **XX** (XXXX) XXXXXX https://doi.org/XXXX/XXXX

Effects of the Fermi Level Energy on the Adsorption of O_2 to Monolayer MoS_2

Philip Klement[1], Christina Steinke[3], Sangam Chatterjee[1], Tim O. Wehling[3], and Martin Eickhoff[2,*]

[1] Institute of Experimental Physics I and Center for Materials Research (ZfM), Justus Liebig University Giessen, D-35392 Giessen, Germany
[2] Institute of Solid State Physics, University of Bremen, D-28359 Bremen, Germany
[3] Institute for Theoretical Physics and Bremen Center for Computational Material Sciences, University of Bremen, D-28359 Bremen, Germany

*E-mail: eickhoff@ifp.uni-bremen.de

Received xxxxxx
Accepted for publication xxxxxx
Published xxxxxx

Abstract

Two-dimensional transition metal dichalcogenides possess large surface-to-volume ratios that make them ideal candidates for sensing applications such as detecting the surface adsorption of specific gas molecules. The resulting changes of the electrical and optical properties allow for detection and analysis of interaction mechanisms at the sensing interface. Specifically, we investigate the influence of O_2 adsorption on monolayer MoS_2 and the role of the Fermi level energy in this process. We record the response in photoluminescence and transport properties of monolayer MoS_2 upon O_2 adsorption and the impact of external electric gating. We find an increase of the photoluminescence intensity and a reduction of the conductivity upon O_2 adsorption, and show that the adsorption can be enhanced by an increase of the Fermi level energy. These results demonstrate that ionosorption of O_2 on MoS_2 by charge transfer only occurs if free carriers are available in the conduction band of MoS_2. This free-carrier-supported adsorption-mechanism is corroborated by density functional calculations. Furthermore, the resulting reduction in screening of the Coulomb interaction between photo-excited electron-hole pairs amplifies the effect of the electron transfer on the excitonic recombination, causing a strong change of the photoluminescence intensity and rendering photoluminescence recording advantageous for sensing applications.

Keywords: transition metal dichalcogenides, MoS_2, adsorption, Fermi level, photoluminescence, conductivity

1. Introduction

Two-dimensional transition metal dichalcogenides (2D TMDs) and their prototype MoS_2 consist of atomically thin layers. In recent years, these materials have received great attention due to their thickness-dependent band structure [1] and favorable electrical properties for applications in field-effect transistors (FETs) [2], chemical sensors [3−5], and optoelectronic devices [6]. Their large surface-to-volume ratios and the presence of different active surface sites such as sulfur vacancies and edge sites of MoS_2 make their electrical and optical properties subject to changes in different dielectric and chemical environments [7−9]. In monolayers of 2D materials, all atoms are exposed to ambiance rendering possible chemical reactions between gaseous species and the surface of fundamental interest. Indeed, the photoluminescence (PL) characteristics of such materials are strongly affected by the presence of specific gas molecules, that can interact with the electronic system upon adsorption [9]. Consequently, different studies regarding the detection of various gaseous species such as NO_2, NH_3, acetone, and other solvents utilizing MoS_2 electrical devices have been reported [3−5,10−12]. Although the gas-sensing performance could be improved through gate voltage or surface functionalization

Accepted Manuscript

 © xxxx IOP Publishing Ltd

[13,14], most reports demonstrate interactions with ambient gases as a proof of principle. A comprehensive understanding of the interactions between 2D TMD surfaces with their gaseous environment is desirable to facilitate sensing and optoelectronic applications. These issues and concepts for the manipulation of the underlying interaction mechanisms at the surface are of great interest for the application of MoS_2 in optoelectronic or sensing devices.

In this work, we report on the influence of a variation of the Fermi level energy in monolayer MoS_2 on the adsorption behavior of oxygen as a model system for the interactions between 2D TMDs and oxidizing gases. The experimental analysis was carried out using monolayer MoS_2 FETs on conductive SiO_2/Si substrates, the latter acting as back gates. These device structures allow for the concurrent characterization of the electrical and optical responses of monolayer MoS_2 in terms of the channel current in the FET, PL, and photocurrent (PC) to the exposure to oxygen. The variation of the Fermi level energy thus allows for the investigation of the underlying mechanisms. We find an oxygen-induced reversible increase of the PL intensity and a concurrent decrease of the conductivity of monolayer MoS_2 that allows us to identify a charge transfer between MoS_2 and O_2 upon adsorption. These effects are attenuated upon reduction of the surface Fermi-level, i. e., for surface depletion of majority carriers by application of a negative back gate bias. This observation is confirmed by first-principles calculations that reveal that an electron transfer from MoS_2 to O_2, required for the ionosorption of O_2^-, only takes place when the system is sufficiently *n*-doped. Further, we find that the manipulation of the PL by external gating strongly depends on the gaseous environment, indicating that the charge transfer between oxygen and MoS_2 is more important than sole electrostatic doping by back gate bias, shedding new light on earlier reports [15,16]. Our work demonstrates that the screening of the Coulomb interaction amplifies the effect of the electron transfer on the PL compared to the conductivity change, which renders PL recording advantageous for sensing applications and processes that involve a charge transfer in 2D TMDs.

2. Methods

Monolayer MoS_2 flakes were prepared by mechanical exfoliation of natural bulk crystals [17] and deposited onto a heavily *p*-type doped Si substrate with a 275 nm thick wet thermal oxide layer. Monolayer samples were identified by optical contrast imaging and confirmed by Raman and PL spectroscopy. Standard electron beam lithography (JEOL JSM 7001F) was used to pattern source and drain contacts in a 300 nm PMMA resist. Ti/Au (5/50 nm) was deposited on top by electron beam evaporation.

Electrical characterization was performed using a Keithley Model 4200-SCS semiconductor characterization system in ambient conditions. A Renishaw inVia Raman microscope equipped for PL detection was used for Raman & PL spectroscopy. A 488 nm Ar-ion laser illuminated the active channel, and the PL was recorded continuously. The spot size was 1.1 µm, and the excitation power was 20 µW.

Devices were placed in a gas-tight chamber that was equipped with an electrical feed-through, an optical window and gas in- and outlets. Electrical and optical properties were monitored in-situ and simultaneously using the characterization systems mentioned above. N_2 and O_2 were injected to the chamber at room temperature. The gaseous environment was controlled by mass flow controllers, and the concentrations were adjusted by the flow rates of each gas. The total flow rate was kept constant at 200 sccm.

We performed density functional theory (DFT) calculations within the local spin density approximation (LSDA) utilizing the Vienna ab-initio simulation package (VASP) [18,19] to simulate the adsorption of O_2 on a monolayer of MoS_2. The Projector-augmented wave approach (PAW) [20,21] with a cutoff energy of 400 eV for the plane wave basis set was used. To avoid interactions between different periodic images of the MoS_2 monolayers we chose a vacuum distance of 15 Å between adjacent periodic images. To model the gas adsorption, we use a 4 x 4 supercell of monolayer MoS_2 hosting one O_2 molecule, which results in a distance larger than 12 Å between two gas molecules. The supercell Brillouin zone integrations are performed with a Γ-centered Monkhorst-Pack mesh [22] of 12 x 12 x 1 k-points. Structures were relaxed until the forces acting on each ion were less than 0.02 eV/Å. We found an optimized lattice constant for monolayer MoS_2 of a = 3.12 Å. As it was suggested by Yue *et al.* [23], the most favorable adsorption sites for the gas molecules are the so called H-sites, where the center of mass of the molecule is positioned on top of the hexagon, and the TM site, where the center of mass is on top of a Mo atom. We investigated two different initial molecular orientations of O_2 with the molecular axis parallel ($\parallel$) or perpendicular ($\perp$) to the monolayer. For different Sulfur-O distances h, we relaxed all structures and found the most favorable configuration as the TM$\parallel$ site with h = 2.8 Å, which is in accordance with Yue *et al.* [23]. Further information on the structure can be found in the Supplementary Information (figure S4). We discuss the charge transfer in terms of the Fermi level position relative to the density of states as it links directly to the experimentally relevant quantity of free charge carriers, and allows us to investigate the effects of doping. To simulate electrostatic *n*-doping of MoS_2 due to a gate bias and with that to allow for a gate controlled manipulation of the Fermi level, we artificially increased the number of electrons in the system while adding homogenous positive background charge to ensure overall charge neutrality of the system.

Accepted Manuscript

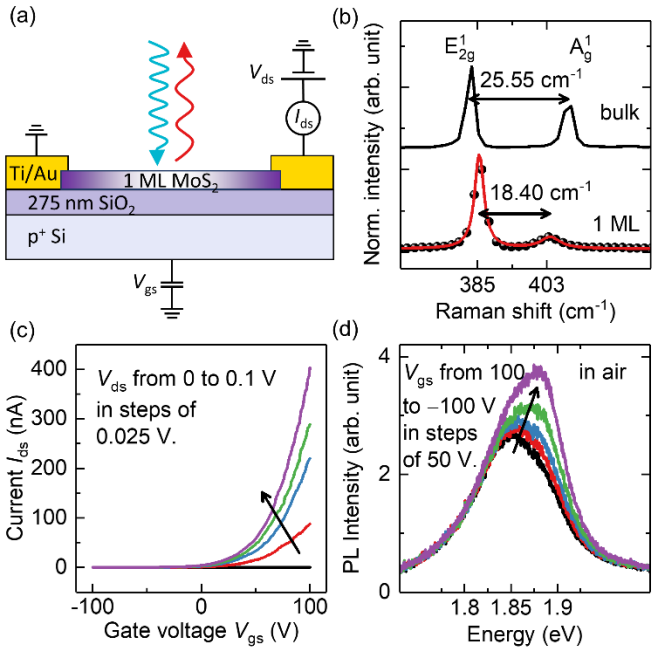

Figure 1. (a) Schematic of a back-gated MoS_2 device and the measurement configuration. (b) Raman spectra of monolayer and bulk MoS_2 and the approximation by two Lorentzian functions (red line). (c) Transfer characteristics I_{ds}-V_{gs} of a monolayer MoS_2 device with the drain-to-source voltage V_{ds} from 0 to 0.1 V. (d) Photoluminescence spectra of a monolayer MoS_2 device for different V_{gs} from -100 to +100 V in air.

3. Results and Discussion

In the measurement configuration, the source contact is grounded, and the drain-to-source voltage V_{ds} is applied to the drain contact resulting in a drain-to-source current I_{ds} (figure 1(a)). The p^+-Si-substrate acts as a back gate that enables the manipulation of the Fermi level energy in the MoS_2 monolayer by application of the gate-to-source voltage V_{gs}. PL is recorded by illumination of the region between both contacts. In Raman spectra of monolayer MoS_2 that form the active device region (figure 1(b)), two peaks are observed near 385 and 403 cm^{-1}, corresponding to the in-plane phonon mode E^1_{2g}, and the out-of-plane phonon mode A^1_g, respectively [24]. The Raman peaks were approximated by two Lorentzian functions, and the peak positions were extracted. We observe that the peak position of the E^1_{2g} mode red shifts and that of the A^1_g mode blue shifts with increasing number of layers. The peak position difference of the monolayer is 18.40 cm^{-1}, which confirms our thickness determination [16,25]. Electrical characteristics of a monolayer device were measured in ambient conditions (figure 1(c)). The transfer characteristics exhibit the typical behavior of an *n*-type channel FET with an on/off-ratio of more than 10^4 and a current of some tens of pA in the off-state, consistent with earlier reports [10,26,27]. The current at V_{ds} = 0 V can be attributed to gate leakage and measurement errors. The average field-effect mobility μ estimated from the slope of the transfer curve (figure S1(a)) [2] is 7 cm^2/Vs and in the upper range of the values of monolayer MoS_2 FETs with metal contacts published in earlier reports [10,28,29]. The PL spectra of monolayer MoS_2 at room temperature and different back gate biases exhibit one broad emission near 1.85 eV. Significant changes in the spectral shape and intensity occur when a negative back gate bias is applied (figure 1(d)). The peak center shifts to 1.88 eV, and the intensity increases by 40 % when monolayer MoS_2 is electrically depleted by a negative gate bias. The high-energy peak at 1.88 eV can be attributed to recombination of the neutral exciton X^0, and the low-energy peak at 1.85 eV to the negatively charged trion X^- (figure 3) [15]. Trions emerge at high densities of free electrons (positive gate bias), when excess electrons are introduced to MoS_2 to bind to photo-generated electron-hole pairs. Spectral weight is transferred to the trion, accompanied by a reduction in excitonic PL. In contrast, less X^- form and the X^0 PL is enhanced when monolayer MoS_2 is depleted of free electrons for negative gate bias.

We have studied the PL and PC of monolayer MoS_2 in O_2/N_2 gaseous atmospheres of different O_2-concentrations and gate biases to investigate the effect of the Fermi level energy on the adsorption and desorption processes. The resulting transients of the PL intensity were obtained by integration of

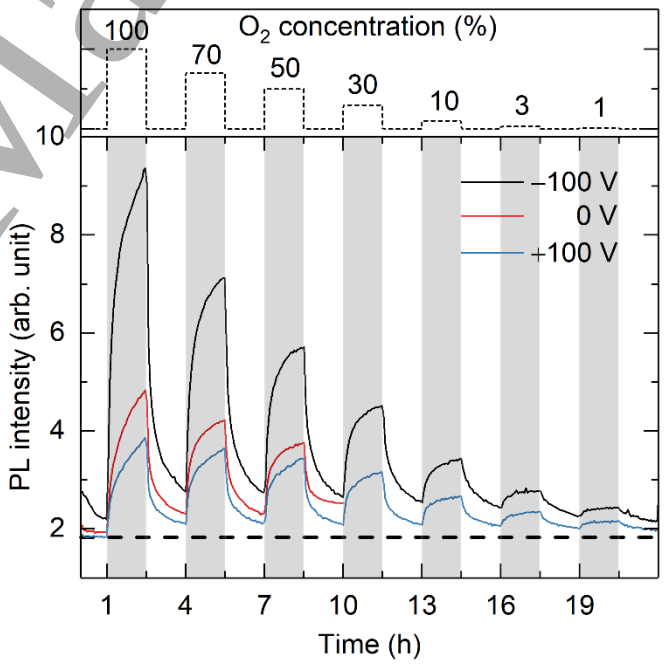

Figure 2. Modulation of the photoluminescence intensity of a monolayer MoS_2 device as a function of the O_2 concentration and back gate bias V_{gs}. The dashed black line indicates the stable base level. The grey background indicates the O_2 intervals and interval timings and concentrations are shown in the upper panel and range from 100 to 1 %. For V_{gs} = 0 V (red line), the gas input failed after 10 h.

Accepted Manuscript

the PL spectra between 1.7 and 2.0 eV (figure 2). A reversible increase in PL intensity whose magnitude scales with the oxygen concentration is observed upon exposure to O_2-containing atmospheres. It can still be resolved for concentrations below 1 %. In each intermediate N_2 interval (white background in figure 2), the PL intensity decreases to approximately the same value indicating a full recovery of the sample. Consistent with Figure 1(d), the PL intensity is increased for negative gate bias compared to positive ones, independent of the gas composition. As this difference is much more pronounced in the presence of O_2, it results in a significant enhancement of the O_2 response. This indicates that the position of the Fermi level significantly influences adsorption and desorption processes of oxygen molecules to the surface. As O_2 is a more electronegative molecule than N_2, it is expected to attract electrons from the MoS_2 layer by charge transfer [7,9].

The spectral shape of individual PL spectra was quantitatively analyzed to assign the change in PL intensity to the contribution of exciton and trion recombination. Their respective ratio yields information about the free electron density in the active channel of the material. PL spectra of monolayer MoS_2 for selected gate biases and gaseous environments were approximated by two Voigt functions corresponding to the neutral exciton (X^0) recombination at 1.88 eV and the trion (X^-) recombination at 1.85 eV (figure 3). It can be seen that both, a variation in gate bias and the change in chemical environment, control the PL intensity and the relative spectral weight distribution between X^0 and X^-. The change in the chemical environment has a significantly stronger impact. As a general observation, the effect of a gate bias variation is more pronounced in oxygen-containing environment. The relative spectral weight of X^0 increases for negative gate bias, i.e., for the case that the material is depleted of free electrons. At the same time, the PL intensity increases due to reduced charge screening and the resulting increase in binding energies of X^0 and X^- [30]. Whereas the exciton PL varies in intensity by a factor of up to 4, the trion PL shows only a weak gate bias dependence.

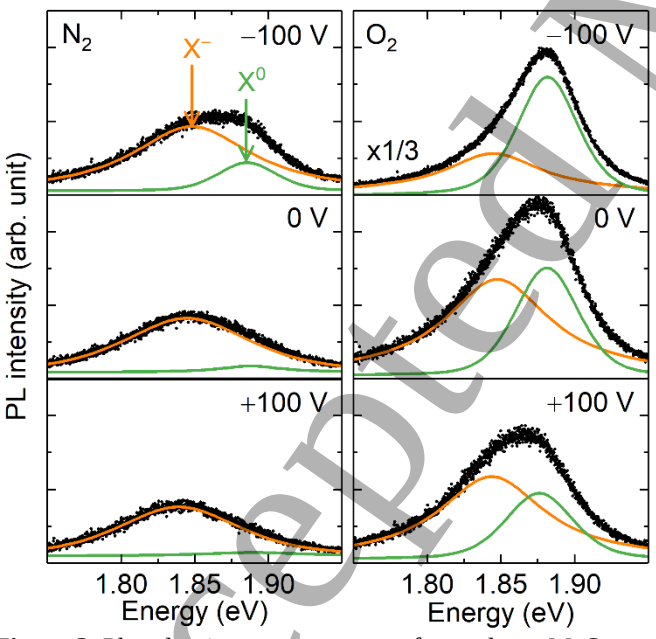

Figure 3. Photoluminescence spectra of monolayer MoS_2 at different back gate biases in N_2 and O_2. The spectra are approximated by two Voigt functions for the exciton X^0 (green line) and trion X^- (orange line) recombination.

The change in PL properties upon exposure to oxygen is similar to that resulting from the application of a negative bias but significantly more pronounced. When the gate is tuned negative or when oxygen is added to the atmosphere, relative spectral weight shifts from X^- to X^0 and the PL intensity increases. This latter observation can be attributed to a depletion of electrons which in this case is of chemical origin. As O_2 is more electronegative than N_2, the ionosorption of O_2 as O_2^- results in the depletion of free electrons due to charge transfer to O_2 molecules. Consequently, X^0 and X^- are generally stabilized due to reduced screening of the Coulomb interaction by free charge carriers, and the PL intensity increases. At the same time, as fewer electrons are available for trion formation, the X^- recombination is attenuated, which partially compensates the stabilization from reduced screening. The changes in PL properties are a result of the competition between screening of the Coulomb interaction and trion formation [9].

In addition to the proposed transition from trion to exciton recombination, the suppression of non-radiative recombination of excitons at defect sites is another possible mechanism to explain some of the observed changes in the PL [7]. To distinguish between both proposed mechanisms, a simultaneous measurement of the source-to-drain current I_{ds} provides further insight as it is directly related to the density of free carriers. Electrical current was converted to sheet conductivity $\sigma = I_{ds}/V_{ds}$, to normalize for a higher V_{ds}, which was used at negative gate bias. The transients of the sheet conductivity σ were recorded concurrently with the PL transients (figure 4(a)). Initially, we focus on the transient recorded at $V_{gs} = +100$ V (blue line). In contrast to the PL, the sheet conductivity under illumination decreases when O_2 is added to the atmosphere. For relatively high O_2 concentrations between 100 and 30 %, σ decreases to an approximately constant base level of 3 µS. For lower O_2 concentrations between 10 and 1 %, σ does not decrease to this base level but to a higher value in each subsequent interval. The reduction in σ upon O_2 exposure confirms the proposed interpretation of a reduction in the free electron concentration due to charge transfer between MoS_2 and O_2. The decreasing response of σ for lower O_2 concentrations (below 30 %) is a consequence of fewer adsorbates available, which results in reduced depletion of MoS_2. The O_2 desorption in the subsequent interval results in a re-increase of the sheet conductivity. During N_2 intervals,

Accepted Manuscript

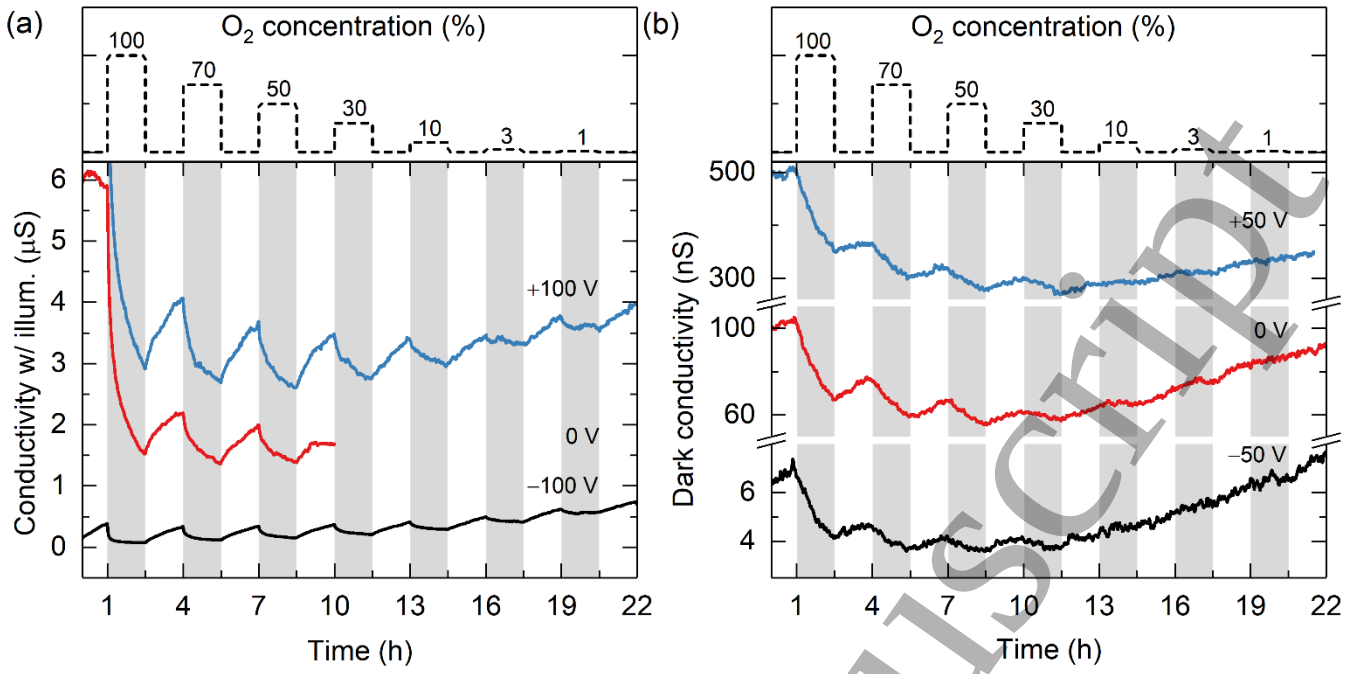

Figure 4. Modulation of the sheet conductivity σ of a monolayer MoS_2 device as a function of the O_2 concentration (100, 70, 50, 30, 10, 3 and 1 %) and back gate bias V_{gs} (−100 to +100 V). (a) with the active channel illuminated and (b) in the dark. For V_{gs} = 0 V (red line), the gas input failed after 10 h.

σ increases, but does not fully recover to its initial value before O_2 exposure, which was observed earlier and is referred to as 'poisoning' [4,29,31]. This indicates chemisorption of O_2 molecules to MoS_2 at room temperature, which desorb on a long time scale. In contrast, the PL response completely recovers within the investigated time intervals, as it is caused by a different mechanim. Whereas the response in conductivity is determined by the modulation in the density of majority carriers (electrons), the PL response is determined by the density of photo-generated minority carriers (holes) which decay on a significantly shorter time scale compared to chemisorption processes. Consequently, the latter effect does not influence PL recovery. A full recovery of the conductivity can be achieved by either long N_2 purging intervals, which was employed between two consecutive measurement cycles or vacuum annealing at higher temperatures, as it was shown for graphene [31].

A similar argumentation that employs the free electron concentration applies when the transients of σ were recorded at different gate biases (black and red lines in figure 4(a)). As already shown above, the number of free electrons in the channel can be tuned by gate bias, which results in different levels of σ. When the gate bias is tuned positive, i.e. the density of electrons is increased in the channel, the absolute change in conductivity upon O_2 exposure increases. This can be understood from basic electrostatics [4] or electronic theory. In the former case, the electric field that builds up at the SiO_2-MoS_2 interface either attracts or repels electrons to or from O_2 depending on the polarity. Utilizing electronic theory, we show that the charge transfer between MoS_2 and O_2 increases with *n*-doping, i. e. for positive back gate bias.

In addition to the effects of external gating, visible-light illumination of oxygen-sensitive devices can increase the sensitivity to O_2 and shorten the recovery time as reported for other materials [32]. The effect of visible-light illumination was analyzed by comparing the transient under illumination σ to that in the dark σ_{drk} (figure 4(b)). First of all, the sheet conductivity is significantly lower for all biases, indicating the dominant contribution of photo-generated carriers to the drain-to-source current I_{ds}. A change in the gaseous environment affects the electrical properties similarly to the illuminated case. When O_2 is added, σ_{drk} decreases, and it recovers in N_2 intervals. In contrast to the illuminated case, the effect of O_2 is observable only for relatively high concentrations above 30 %. Below that, σ_{drk} increases on a long time scale. The effect of O_2 adsorption cannot be observed in σ_{drk}, and it recovers to its initial value in N_2 atmosphere. It can be concluded that visible-light illumination not only increases the channel current through photo-generated carriers, but it also results in a higher sensitivity. Similar explanations apply to the effects of external gating in the illuminated and dark case, and are given above. In the dark, the conductivity decreases even further towards negative biases, and only a small effect can be observed at V_{gs} = −50 V, indicating a vanishing charge transfer between MoS_2 and O_2. This further emphasizes the importance of free carriers and the relative position of der Fermi level in MoS_2 for O_2 adsorption processes.

Accepted Manuscript

This conception is supported by theoretical calculations of the density of states (DOS) of MoS_2 in absence (upper panels) and presence (lower panels) of oxygen as adsorbates for different free electron concentrations controlled by the gate bias (figure 5). The corresponding band structures can be found in the Supplementary Information (figure S5). The doping of 0.01 electrons/unit cell corresponds to approximately 10^{13} electrons/cm². In the undoped system without surface adsorbates, the band gap of MoS_2 is clearly visible in the DOS and the Fermi level energy is located inside the gap, as expected for a pristine semiconductor (figure 5(a)). When the number of electrons in the system increases, the Fermi level shifts to energies within the conduction band of MoS_2 (figure 5(b)). The oxygen adsorbates change the DOS by contributing a fully occupied molecular orbital in the spin up channel below the valence band edge and an orbital with spin down character within the gap of MoS_2 (figure 5(c)). Without additional doping of MoS_2, the spin down orbital remains empty. Thus, in absence of free electrons in the conduction band of MoS_2, the number of free carriers remains zero. Hence, there is no charge transfer from the extended MoS_2 electronic states to those states localized predominantly in the oxygen orbitals. This situation changes for gate-induced *n*-doping (figure 5(d)). The Fermi level is now above the MoS_2 conduction band edge. Electron transfer from MoS_2 to O_2 occurs and oxygen depletes the MoS_2 conduction band. This is why the effect of oxygen adsorption on the measured current in the "dark state" is stronger for *n*-doped systems. The fact that the conductivity under illumination shows a strong response to oxygen irrespective of the gate doping level

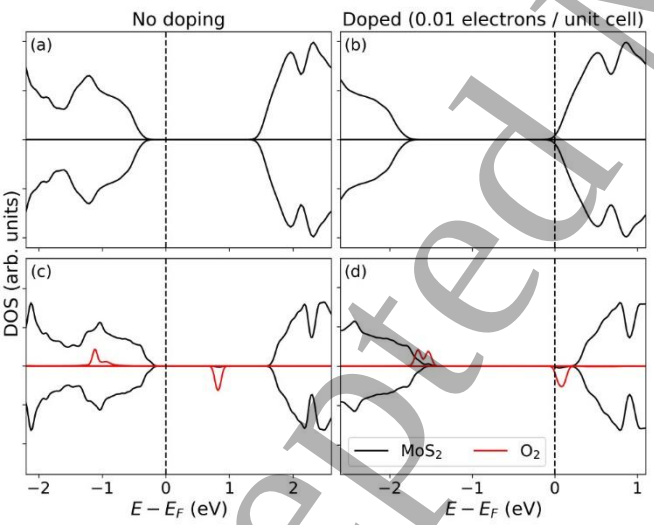

Figure 5. Density of states of MoS_2 ((a), (b)) and in presence of oxygen ((c), (d)). The black (red) line shows the local density of states of MoS_2 (at the O_2 molecules). Different charge doping levels are accounted for: ((a), (c)), no doping and ((b), (d)), 0.01 electrons per unit cell. The density of states at the positive (negative) ordinate corresponds to spin up (down) states.

signals that also photo-excited electrons can be transferred from the conduction band of MoS_2 to the O_2 adsorbates and even dominate this effect.

Finally, we emphasize that the effect of O_2-adsorption is significantly stronger on the PL intensity (figure 2) compared to the conductivity (figure 4). This manifests in a greater sensitivity of the PL intensity. Further, in PL intensity, the effect of O_2 adsorption is significantly stronger than that of a variation of the gate bias. These observations support the assignment of the increase in PL intensity to a reduction in screening of the Coulomb interaction and the related increase in exciton binding energy mentioned above: The number of excitons that contribute to the PL intensity scales linearly with the number of electrons and holes, and superlinearly with the screening of the Coulomb interaction. This results in a superlinear dependence of the PL intensity on the number of free carriers. In contrast, the conductivity scales linearly with the number of free carriers. This screening of the Coulomb interaction is responsible for the much higher sensitivity of the PL to changes in the number of free carriers. This "sensitivity amplification" by screening of the Coulomb interaction makes PL superior to conductivity measurements when charge carrier transfers are involved.

4. Conclusions

In conclusion, we demonstrate that a variation of the Fermi level of MoS_2 controls the adsorption of O_2 molecules. Concurrent measurements of the PL and conductivity of MoS_2 FETs allow us to identify an electron transfer from MoS_2 to O_2 on adsorption, which was proposed earlier [7,9]. The Fermi level controls this electron transfer, which decreases when the surface Fermi level is reduced. This is confirmed by first-principles calculations that reveal that an electron transfer only takes place when the system is sufficiently *n*-doped. The effects of O_2 adsorption are significantly stronger in the PL intensity compared to the conductivity. We ascribe this sensitivity enhancement to an amplification of the PL by screening of the Coulomb interaction. Further, the manipulation of the PL by external gating strongly depends on the gaseous environment. This indicates that the electron transfer between MoS_2 and O_2 is more important than sole electrostatic doping by back gate bias and explains earlier results on gated configurations [16]. These findings expand the knowledge on the interactions between gaseous adsorbates and 2D TMDs that are relevant for fundamental research as well as future optoelectronic applications of 2D TMDs. Future work should elucidate how the sensitivity amplification by the Coulomb interaction could make optical detection of adsorption processes superior to the electrical detection.

Acknowledgements

This work was supported by the European Graphene Flagship and the DFG via Grant No. GRK 2247 and through

Accepted Manuscript

computing resources at the North German Supercomputing Alliance (HLRN). SC acknowledges financial support by the German Science Foundation (DFG) through Projects B2 of the Collaborative Research Center 1083 and the Heisenberg Programme (CH660/2).

References

[1] Mak K F, Lee C, Hone J, Shan J and Heinz T F 2010 Atomically Thin MoS_2: A New Direct-Gap Semiconductor *Phys. Rev. Lett.* **105** 136805

[2] Radisavljevic B, Radenovic A, Brivio J, Giacometti V and Kis A 2011 Single-layer MoS_2 transistors *Nat. Nanotechnol.* **6** 147-150

[3] Perkins F K, Friedman A L, Cobas E, Campbell P M, Jernigan G G and Jonker B T 2013 Chemical Vapor Sensing with Monolayer MoS_2 *Nano Lett.* **13** 668-673

[4] Late D J *et al.* 2013 Sensing Behavior of Atomically Thin-Layered MoS_2 Transistors *ACS Nano* **7** 4879-4891

[5] Samnakay R, Jiang C, Rumyantsev S L, Shur M S and Baladin A A 2015 Selective chemical vapor sensing with few-layer MoS_2 thin-film transistors: Comparison with graphene devices *Appl. Phys. Lett.* **106** 023115

[6] Ross J S *et al.* 2014 Electrically tunable excitonic light-emitting diodes based on monolayer WSe_2 p-n junctions *Nat. Nanotechnol.* **9** 268-272

[7] Nan H *et al.* Strong Photoluminescence Enhancement of MoS_2 through Defect Engineering and Oxygen Bonding *ACS Nano* **8** 5738-5745

[8] Qiu H, Pan L, Yao Z, Li J, Shi Y and Wang X 2012 Electrical characterization of back-gated bi-layer MoS_2 field-effect transistors and the effect of ambient on their performances *Appl. Phys. Lett.* **100** 123104

[9] Tongay S, Zhou J, Ataca C, Liu J, Kang J S, Matthewst T S, You L, Li J, Crossman J C and Wu J 2011 Broad-Range Modulation of Light Emission in Two-Dimensional Semiconductors by Molecular Physisorption Gating *Nano Lett.* **13** 2831-2836

[10] Liu B, Chen L, Liu G, Abbas A N, Fathi M and Zhou C 2014 High-Performance Chemical Sensing Using Schottky-Contacted Chemical Vapor Deposition Grown Monolayer MoS_2 Transistors *ACS Nano* **8** 5304-5314

[11] He Q, Zeng Z, Yin Z, Li H, Wu S, Huang X and Zhang H 2012 Fabrication of Flexible MoS_2 Thin-Film Transistor Arrays for Practical Gas-Sensing Applications *Small* **8** 2994-2999

[12] Donarelli M, Prezioso S, Perrozzi F, Bisti F, Nardone M, Giancaterini L, Cantalini C and Ottaviano L 2015 Response to NO_2 and other gases of resistive chemically exfoliated MoS_2-based gas sensors *Sens. Actuators, B* **207** 602-613

[13] Tong Y, Lin Z, Thong J T L, Chan D S H and Zhu C 2015 MoS_2 oxygen sensor with gate voltage stress induced performance enhancement *Appl. Phys. Lett.* **107** 123105

[14] Ko K Y *et al*. 2016 Improvement of Gas-Sensing Performance of Large-Area Tungsten Disulfide Nanosheets by Surface Functionalization *ACS Nano* **10** 9287-9296

[15] Mak K F, He K, Lee C, Lee G H, Hone J, Heinz T F and Shan J 2013 Tightly bound trions in monolayer MoS_2 *Nat. Mater.* **12** 207-211

[16] Newaz A K M, Prasai D, Ziegler J I, Caudel D, Robinson S, Hadlund Jr R F and Bolotin K I 2013 Electrical control of optical properties of monolayer MoS_2 *Solid State Commun.* **155** 49-52

[17] Huang Y, Sutter E, Shi N N, Zheng J, Yang T, Englund D, Gao H and Sutter P 2015 Reliable Exfoliation of Large-Area High-Quality Flakes of Graphene and Other Two-Dimensional Materials *ACS Nano* **9** 10612-10620

[18] Kresse G and Hafner J 1993 Ab *initio* molecular dynamics for liquid metals *Phys. Rev. B* **47** 558

[19] Kresse G and Furthmüller J 1996 Efficiency of ab-initio total energy calculations for metals and semiconductors using a plane-wave basis set *Comput. Mater. Sci.* **6** 15-50

[20] Blöchl P E 1994 Projector augmented-wave method *Phys. Rev. B* **50** 17953

[21] Kresse G and Joubert J 1999 From ultrasoft pseudopotentials to the projector augmented-wave method *Phys. Rev. B* **59** 1758

[22] Monkhorst H J and Pack J D 1976 Special points for Brillouin-zone integrations *Phys. Rev. B* **13** 5188

[23] Yue Q, Shao Z, Chang S and Li J 2013 Adsorption of gas molecules on monolayer MoS_2 and effect of applied electric field *Nanoscale Res. Lett.* **8**:425

[24] Molina-Sanchez A and Wirtz L 2011 Phonons in single-layer and few-layer MoS_2 and WS_2 *Phys. Rev. B* **84** 155413

[25] Lee C, Yan H, Brus L E, Heinz T F, Hone J and Ryu S 2010 Anomalous Lattice Vibrations of Single- and Few-Layer MoS_2 *ACS Nano* **4** 2695-2700

[26] Qi L, Wang Y, Shen L and Wu Y 2016 Chemisorption-induced n-doping of MoS_2 by oxygen *Appl. Phys. Lett.* **108** 063103

[27] Park W, Park J, Jang J, Lee H, Jeong H, Cho K, Hong S and Lee T 2013 Oxygen environmental and passivation effects on molybdenum disulfide field effect transistors *Nanotechnology* **24** 095202

[28] Shih F, Wu Y, Shih Y, Shih M, Wu T, Ho P, Chen C, Chen Y, Chiu Y and Wang W 2017 Environment-insensitive and gate-controllable photocurrent enabled by bandgap engineering of MoS_2 junctions *Sci. Rep.* **7** 44768

[29] Li H, Yin Z, He Q, Li H, Huang X, Lu G, Fam D W H, Tok A I Y, Zhang Q and Zhang H 2012 Fabrication of Single- and Multilayer MoS_2 Film Based Field-Effect Transistors for Sensing NO at Room Temperature *Small* **8** 63-67

[30] Lin Y, Ling X, Yu L, Huang S, Hsu A L, Lee Y, Kong J, Dresselhaus M S and Palacios T 2014 Dielectric Screening of Excitons and Trions in Single-Layer MoS_2 *Nano Lett.* **14** 5569-5576

[31] Schedin F, Geim A K, Morozov S V, Hill E W, Blake P, Katnelson M I and Novoselov K S 2007 Detection of individual gas molecules adsorbed on graphene *Nat. Mater.* **6** 652-655

[32] Fan S, Srivastava A and Dravid V 2009 UV-activated room-temperature gas sensing mechanism of polycrystalline ZnO *Appl. Phys. Lett.* **95** 142106

Accepted Manuscript

Publication 2

Surface Diffusion Control Enables Tailored-Aspect-Ratio Nanostructures in Area-Selective Atomic Layer Deposition

Philip Klement, Daniel Anders, Lukas Gümbel, Michele Bastianello, Fabian Michel, Jörg Schörmann, Matthias T. Elm, Christian Heiliger, and Sangam Chatterjee

ACS Applied Materials & Interfaces **13**, 19398−19405 (2021), DOI: 10.1021/acsami.0c22121

You can view the full text of this article at
http://pubs.acs.org/articlesonrequest/AOR-UH9TTJCVBUDEQ7WSZIV5
to download this article.

ACS APPLIED MATERIALS & INTERFACES

www.acsami.org

Research Article

Surface Diffusion Control Enables Tailored-Aspect-Ratio Nanostructures in Area-Selective Atomic Layer Deposition

Philip Klement, Daniel Anders, Lukas Gümbel, Michele Bastianello, Fabian Michel, Jörg Schörmann, Matthias T. Elm, Christian Heiliger, and Sangam Chatterjee*

Cite This: *ACS Appl. Mater. Interfaces* 2021, 13, 19398–19405

Read Online

ACCESS | Metrics & More | Article Recommendations | Supporting Information

ABSTRACT: Area-selective atomic layer deposition is a key technology for modern microelectronics as it eliminates alignment errors inherent to conventional approaches by enabling material deposition only in specific areas. Typically, the selectivity originates from surface modifications of the substrate that allow or block precursor adsorption. The control of the deposition process currently remains a major challenge as the selectivity of the no-growth areas is lost quickly. Here, we show that surface modifications of the substrate strongly manipulate surface diffusion. The selective deposition of TiO_2 on poly(methyl methacrylate) and SiO_2 yields localized nanostructures with tailored aspect ratios. Controlling the surface diffusion allows tuning such nanostructures as it boosts the growth rate at the interface of the growth and no-growth areas. Kinetic Monte-Carlo calculations reveal that species move from high to low diffusion areas. Further, we identify the catalytic activity of $TiCl_4$ during the formation of carboxylic acid on poly(methyl methacrylate) as the reaction mechanism responsible for the loss of selectivity and show that process optimization leads to higher selectivity. Our work enables the precise control of area-selective atomic layer deposition on the nanoscale and offers new strategies in area-selective deposition processes by exploiting surface diffusion effects.

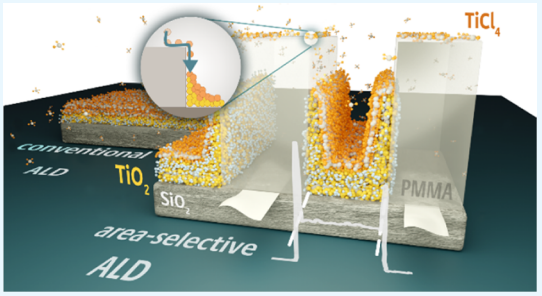

KEYWORDS: *nanofabrication, self-aligned fabrication, atomic layer deposition (ALD), area-selective deposition, surface diffusion*

INTRODUCTION

The downscaling of integrated circuits in semiconductor technology currently relies almost completely on top-down processing featuring a complex combination of many material depositions, extreme ultraviolet lithography, and etching steps. Approaching sub-5 nm device scales makes perfect alignment in nanopatterning for reliable processing extremely challenging as it mandates virtually atomic-scale precision.[1] In particular, alignment-related edge placement errors have become a major issue in downscaling.[2] Consequently, new bottom-up schemes for the most demanding processing steps are required to circumvent challenges or even avoid inherent deficiencies of top-down fabrication.

Atomic layer deposition (ALD) is such a bottom-up thin film deposition technique where atoms or small units grow on a substrate layer-by-layer. It relies on exposing the substrate to the alternating cyclic exposure of two or more vapor-phase precursors that react in self-limiting surface reactions between functional groups and vapor-phase precursors. This leads to growth with atomic-level thickness control and high conformity.[3] However, the bottom-up, self-aligned fabrication by ALD mandates the deposition processes limited to specific areas. As a result, area-selective atomic layer deposition (AS-ALD) emerged over recent years.[4] This approach enacts spatial control of the growth areas by locally tailoring the specific surface chemistry. It enables bottom-up fabrication schemes that offer the potential to significantly reduce the number of required device processing steps. AS-ALD typically includes a substrate-patterning step before the area-selective ALD process. This reflects the reality of self-aligned fabrication schemes where prepatterned and preprocessed materials serve as starting substrates. Such patterning-centered reasoning classifies two main routes for AS-ALD: (A) AS-ALD by area passivation. Parts of the substrate surface are deactivated, *i.e.*, made inert to the chemistry of the ALD process; and (B) AS-ALD by area activation. Here, parts of the inert substrate surface are made reactive to the chemistry of the ALD process. Thus, a sample surface in AS-ALD features several materials. ALD deposition needs to be selective to one of these materials.

Previous work in the field of AS-ALD has covered dielectric-on-dielectric[5−7] and metal-on-dielectric[8−13] deposition as those are industrially most relevant. AS-ALD by area activation has been achieved by deposition of a metallic or oxidic seed

Received: December 14, 2020
Accepted: April 1, 2021
Published: April 15, 2021

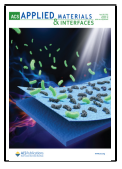

ACS Publications

© 2021 The Authors. Published by American Chemical Society

https://doi.org/10.1021/acsami.0c22121
ACS Appl. Mater. Interfaces 2021, 13, 19398−19405

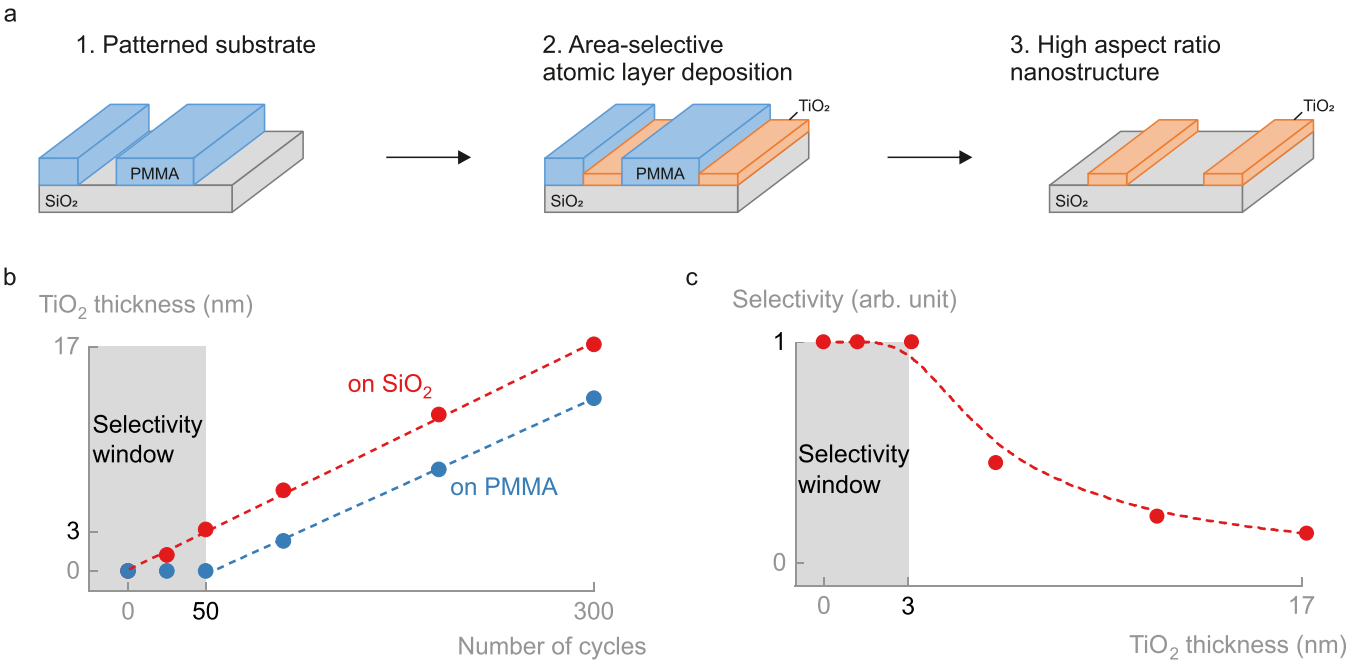

Figure 1. Schematic and selectivity of the area-selective ALD approach. (a) PMMA patterns on SiO_2 serve as starting substrates. TiO_2 is deposited in an area-selective ALD process, and mask removal yields high-aspect-ratio nanostructures. (b) TiO_2 film thickness on SiO_2 and PMMA substrates as a function of the number of cycles. On SiO_2, the TiO_2 film thickness increases linearly, whereas a nucleation delay of 50 cycles occurs on PMMA. The dashed lines indicate the linear regime of the fit. (c) Selectivity of the TiO_2 deposition on PMMA as a function of the deposited thickness on SiO_2. The selectivity window is 3.1 nm or 50 cycles. The dashed line serves as a guide to the eye.

layer,[5,9] whereas in AS-ALD by area deactivation, the substrate surface has been chemically modified by self-assembled monolayers (SAM)[7,8,13] and polymers.[6,10,12] Most AS-ALD studies focused on the demonstration of selectivity in a specific ALD process and the improvement of the selectivity toward thicker layers. Promising approaches such as the introduction of correction steps in so-called supercycles have been developed and enable high selectivity,[11,14] but the general problem of a loss of selectivity persists. Those studies have shown that the loss of selectivity involves nucleation on the no-growth area, but the nucleation process and limiting factors have not been clarified yet. They mandate the need for a better understanding of the fundamental interactions between precursors and reactants with specific surfaces in AS-ALD processes to enable higher selectivity.[2,4]

In this work, we successfully control the surface diffusion in the model system TiO_2 on poly(methyl methacrylate) (PMMA) to achieve selectively high-aspect-ratio nanostructures and show that surface diffusion boosts the growth rate and leads to an accumulation at the growth to the no-growth interface. We use PMMA for area deactivation, which is a widely used and well-established polymer and allows for nanometer-scale structures with ease of preparation. Further, it serves as a model system for AS-ALD processes based on blocking layers including SAMs and ABC-type supercycles with inhibitors as it features the same CH_3 groups that block precursor adsorption and thus are unreactive toward most ALD chemistries.[11,14,15] In the patterning step, a small lateral pattern establishes the basis for the AS-ALD process (Figure 1a). The use of electron-beam lithography with its ability to generate sub-10 nm lateral patterns meets the resolution requirement of modern semiconductor device fabrication. We analyze the key factors in AS-ALD in terms of nucleation delay and selectivity measured by X-ray reflectivity (XRR) and find a selectivity window of 50 cycles or 3.1 nm with selectivity of 1 for TiO_2 on PMMA. Further, we identify the catalytic activity of $TiCl_4$ during the formation of carboxylic acid on PMMA as the chemical reaction responsible for the loss of selectivity. We then elaborate on the selectivity on a molecular-scale level by atomic force microscopy (AFM) and find small islands of TiO_2 growing on PMMA beyond the selectivity window. On prepatterned substrates, diffusion of species on the surface of PMMA results in a strongly increased growth per cycle (GPC) on SiO_2 compared to unpatterned substrates and an accumulation at the growth to the no-growth interface. A kinetic Monte-Carlo (KMC) model for particle diffusion excellently reproduces our experimental observations and identifies surface diffusion of species as the physical origin of both, the strongly increased GPC and the accumulation in AS-ALD. Finally, we control the surface diffusion of species through the purge times in the ALD process to enable the preparation of nanostructures with tailored aspect ratios and film thicknesses beyond the inherent selectivity of the AS-ALD process.

EXPERIMENTAL SECTION

Substrate Preparation and Patterning Step. Si substrates with a 275 nm thick wet-thermal oxide layer were cleaned with acetone, isopropanol (IPA), and deionized (DI) water and coated with a 300 nm thick PMMA (950K molecular weight, 4% dissolved in anisole) layer. Microscale patterns were defined by electron-beam lithography (JEOL JSM 7001F electron microscope equipped with a XENOS XeDraw high-speed writer system) followed by the development in a mixture of IPA/DI water (ratio 2:1). For some experiments, a trench was formed by reactive Ar-ion etching on the patterned PMMA substrate. SiO_2 was etched in the uncovered regions creating an 8.9 nm deep trench.

Atomic Layer Deposition and Lift-off. TiO_2 was deposited in a commercial thermal ALD system (Picosun R200 Standard) at 120 °C

https://doi.org/10.1021/acsami.0c22121
ACS Appl. Mater. Interfaces 2021, 13, 19398−19405

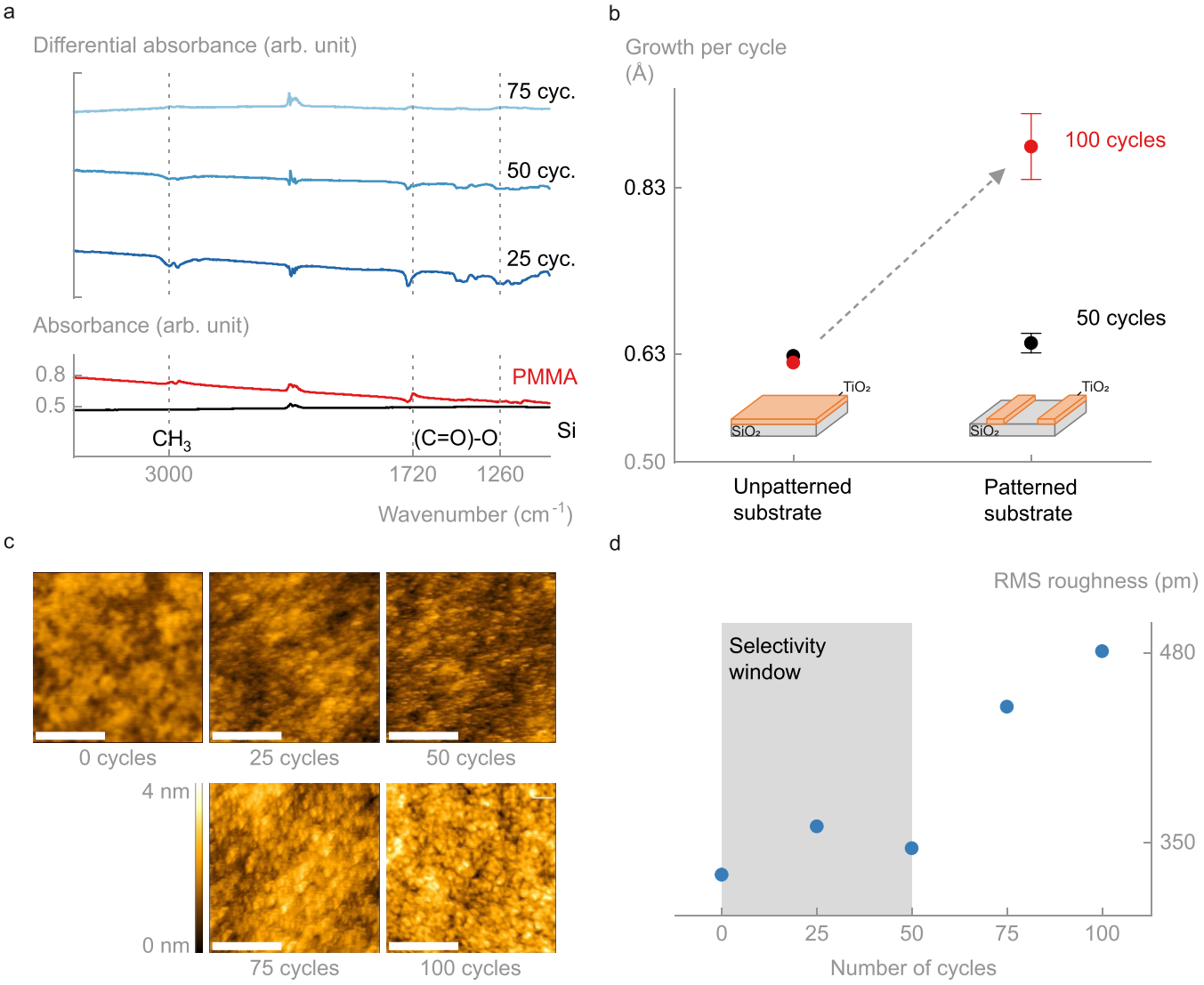

Figure 2. FTIR, topography, and growth per cycle (GPC) in area-selective ALD. (a) Infrared differential absorbance spectra of TiO_2 films grown on PMMA. The disappearance of the characteristic CH_3 and C═O vibrations near 3000 and 1720 cm^{-1} indicates the nucleophilic attack of H_2O on the C═O group of PMMA catalyzed by $TiCl_4$. (b) GPC of TiO_2 in AS-ALD on (un-)patterned substrates. The GPC on patterned substrates increases significantly when the number of cycles is beyond the selectivity window. (c) Topography of TiO_2 on PMMA as a function of the number of cycles. TiO_2 islands appear on the surface at 75 cycles and form a complete film at 100 cycles. The scale bar is 200 nm. (d) The roughness of TiO_2 on PMMA as a function of the number of cycles increases likewise.

to prevent the PMMA patterns from reflowing. Titanium tetrachloride and water were used as precursors and pulsed for 0.1 and 3 s, respectively (Figure S1). The system was purged with nitrogen for 10 s after each precursor pulse. After ALD, samples were immersed in 50 °C hot acetone for PMMA lift-off followed by cleaning with IPA and O_2 plasma for 3 min to remove the residual polymer.

Analytical Methods. The nucleation and selectivity of TiO_2 ALD on PMMA in the first part of this work were analyzed in terms of TiO_2 thicknesses, which were determined by X-ray reflectivity with a Siemens/Bruker D5000 X-ray diffraction system and a subsequent fit of the reflectivity (Figure S2). The fit of the linear regime in the plot of the TiO_2 thickness as a function of the number of cycles yields the growth per cycle (GPC). We use the generally accepted definition of the selectivity S from the field of area-selective chemical vapor deposition

$$S = \frac{\theta_{GA} - \theta_{NGA}}{\theta_{GA} + \theta_{NGA}} \quad (1)$$

where θ_{GA} and θ_{NGA} are the amounts of the material deposited (*i.e.*, in terms of film thickness, coverage, etc.) on the growth and no-growth areas, respectively.[16] Infrared (IR) absorption spectra were recorded on IR-transparent Si substrates with a Bruker Equinox 55 FTIR spectrometer equipped with a reflectance-measuring unit and converted to absorbance. We calculate the differential absorbance following

$$\Delta A_{n+25,n} = \frac{A_{n+25} - A_n}{A_n} \quad (2)$$

where A_n is the absorbance of the sample with n cycles of TiO_2 (Figure S4). The combination of PMMA patterning, area-selective ALD, and PMMA lift-off results in TiO_2 patterns on SiO_2. The topography of these TiO_2 patterns prepared by AS-ALD was analyzed with an AIST-NT SmartSPM 1000 AFM in a noncontact tapping mode to prevent sample damage. The GPC in the AS-ALD process on patterned substrates was calculated from the TiO_2 edge height as measured by AFM and the number of cycles. We define the area ratio (AR) as

$$AR = \frac{A_{NGA}}{A_{GA}} \quad (3)$$

https://doi.org/10.1021/acsami.0c22121
ACS Appl. Mater. Interfaces 2021, 13, 19398−19405

where A_{GA} and A_{NGA} are the absolute areas of the growth and no-growth areas, respectively.

Kinetic Monte-Carlo Methods. All molecular dynamics calculations were performed using a kinetic Monte-Carlo (KMC) approach. The model derives from a Markov-chain approach and considers particle collision and occupied sites. Input parameters are lattice dimensions, iteration time, number of precursor molecules, size, the proportion of different diffusion areas, and the ratio of different diffusion velocities.

RESULTS AND DISCUSSION

Selectivity of TiO_2 ALD on PMMA. The selectivity of TiO_2 on PMMA determines the potential applications of the AS-ALD process, as each application requires different film thicknesses or the number of cycles. Therefore, we study the nucleation delay of TiO_2 on PMMA. Figure 1b shows the TiO_2 film thickness as a function of the number of ALD cycles. We observe a nucleation delay of 50 cycles on PMMA. The TiO_2 film thickness is negligible in the transient regime,[17] and linear growth with a growth per cycle (GPC) of 0.54 Å $cycle^{-1}$ sets in after 50 cycles. In contrast, no nucleation delay occurs on SiO_2, where the growth is linear over the whole range with an average GPC of 0.57 Å $cycle^{-1}$. We use the generally accepted definition of the selectivity S from the field of area-selective chemical vapor deposition (eq 1).[16] Figure 1c shows the accordingly calculated selectivity of the TiO_2 ALD process on PMMA. The selectivity is 1 for up to 50 cycles (3.1 nm), decreases rapidly thereafter, and eventually, deposition occurs on both surfaces. These results indicate that the difference in nucleation delays on the two surfaces causes AS-ALD of TiO_2. The selectivity window is 50 cycles or 3.1 nm of TiO_2 on SiO_2. The absolute size of the selectivity window is not readily comparable as it depends, among others, on the chemical process reaction, surface chemistry of the substrate, and the deposition parameters. Nevertheless, similar sizes in terms of thicknesses and number of ALD cycles have been observed for dielectric-on-dielectric[5,14,18,19] and metal-on-dielectric[8,11] processes.

The specific surface chemistry of SiO_2 and PMMA explains the microscopic nature of the selectivity window in the ALD process as they feature different surface groups with distinct reactivities. SiO_2 is primarily −OH-terminated and $TiCl_4$ reacts readily in the first self-limiting half-reaction

$$Si - OH^* + TiCl_4 \rightarrow Si - O - TiCl_3^* + H_2O \quad (4)$$

where the asterisks denote the surface species. In contrast, PMMA features methyl ester as a functional group bond to its backbone but no −OH groups. The ALD surface chemistry is more complex with several possible reaction mechanisms: (1) precursor molecules can infiltrate the polymer and participate in surface−interface reactions, (2) permeate to interstitial spaces and react with the second precursor, or (3) react with other functional groups.[20]

Previous works on the ALD deposition of Al_2O_3 and TiO_2 on PMMA have found indications for surface−interface reactions,[21] subsurface diffusion,[22,23] reaction with the polymer,[23,24] or full growth inhibition.[6] It is critical to understand the prevalent mechanism to be able to enhance the selectivity of the TiO_2 on PMMA during the AS-ALD process. Choosing an appropriate, sufficiently thick polymer film suppresses surface−interface reactions by preventing precursors from reaching the interface.[25] Also, prolonging the purge steps removes adsorbed and diffused precursors and decreases the subsurface diffusion.[23] Although we use 300 nm thick PMMA films and relatively long purge times, we detected Ti species on the surface of PMMA in X-ray photoelectron spectroscopy (XPS, Figure S3). This indicates that a reaction of $TiCl_4$ with PMMA is the prevalent mechanism for the loss of selectivity. It has been suspected early on that $TiCl_4$ may be complexed by the carbonyl group in PMMA.[25] Indeed, it is well known that hard Lewis acids can easily be coordinated by carbonyl compounds.[26,27] We perform infrared spectroscopy to identify the chemical mechanism for the loss of selectivity on PMMA (Figure 2a), and calculate the differential absorbance to visualize small changes in absorbance (Figure S4). The PMMA film before AS-ALD shows characteristic peaks attributed to the CH_3 asymmetric and symmetric stretching at 3000 and 2950 cm^{-1}, and the C═O ester and carbonyl stretching features at 1720 and 1260 cm^{-1}, respectively. After 25 cycles of alternating $TiCl_4$ and H_2O pulses, the peak intensity of the C═O ester stretching feature at 1720 cm^{-1} decreases significantly indicating the reaction between $TiCl_4$ and PMMA. The peak intensities of the CH_3 stretching features at 3000 and 2950 cm^{-1} decrease likewise but less pronounced. Furthermore, a mode appears near 1400 cm^{-1} that belongs to the lattice vibration of TiO_2 (Ti−O−Ti stretching).[28] The reaction of $TiCl_4$ with the PMMA surface can be separated into two different mechanisms. The adsorbed $TiCl_4$ acts catalytically like a Lewis acid activating the ester group to favor the nucleophilic attack of H_2O on the C═O carbon, yielding $HO-CH_3$ and the carboxylic acid.

$$COOCH_3^* + H_2O \rightarrow COOH^* + HOCH_3 \quad (5)$$

Here, the asterisks denote the surface species. The mass effect of the water pulse is the main driving force of the reaction. Consequently, the growth is zero in this phase as $TiCl_4$ acts as a catalyst (*cf.* selectivity window, Figure 1b). Second, the reaction proceeds with the same mechanism displayed on SiO_2 once the hydroxyl on the carboxylic acid has formed

$$COOH^* + TiCl_4 \rightarrow COO - TiCl_3^* + HCl \quad (6)$$

i.e., TiO_2 grows on PMMA similar to SiO_2 explaining the identical GPC (Figure 1b).

One important feature of PMMA is that the carbonyl group is not located in the backbone of the polymer. Thus, the chain will not dissociate when reacting with $TiCl_4$, making it a robust choice for area deactivation in the AS-ALD processes. The appearance of an additional $TiCl_x$ species on PMMA in XPS supports this interpretation (Figure S3).

Surface Diffusion in Area-Selective ALD. The complex surface chemistry in AS-ALD on polymers yields very different results compared to inorganic substrates. Typically, the topography of the thin film changes,[19] effects like swelling of the polymer[29] or delamination of the thin film occur,[30] and the GPC can change upon patterning.[31] These issues make a precise process control challenging and underline the need for a systematic understanding of the fundamental processes. Therefore, we study the topography and GPC to facilitate the control of the AS-ALD process.

We measured the topography of TiO_2 on PMMA as a function of the number of cycles to examine the formation of TiO_2 during the area-selective process (Figure 2c,d). The surface of PMMA is smooth, virtually free of defects, and the roughness is low (330−360 pm) as long as the number of cycles is within the selectivity window (0−50 cycles). The

https://doi.org/10.1021/acsami.0c22121
ACS Appl. Mater. Interfaces 2021, 13, 19398−19405

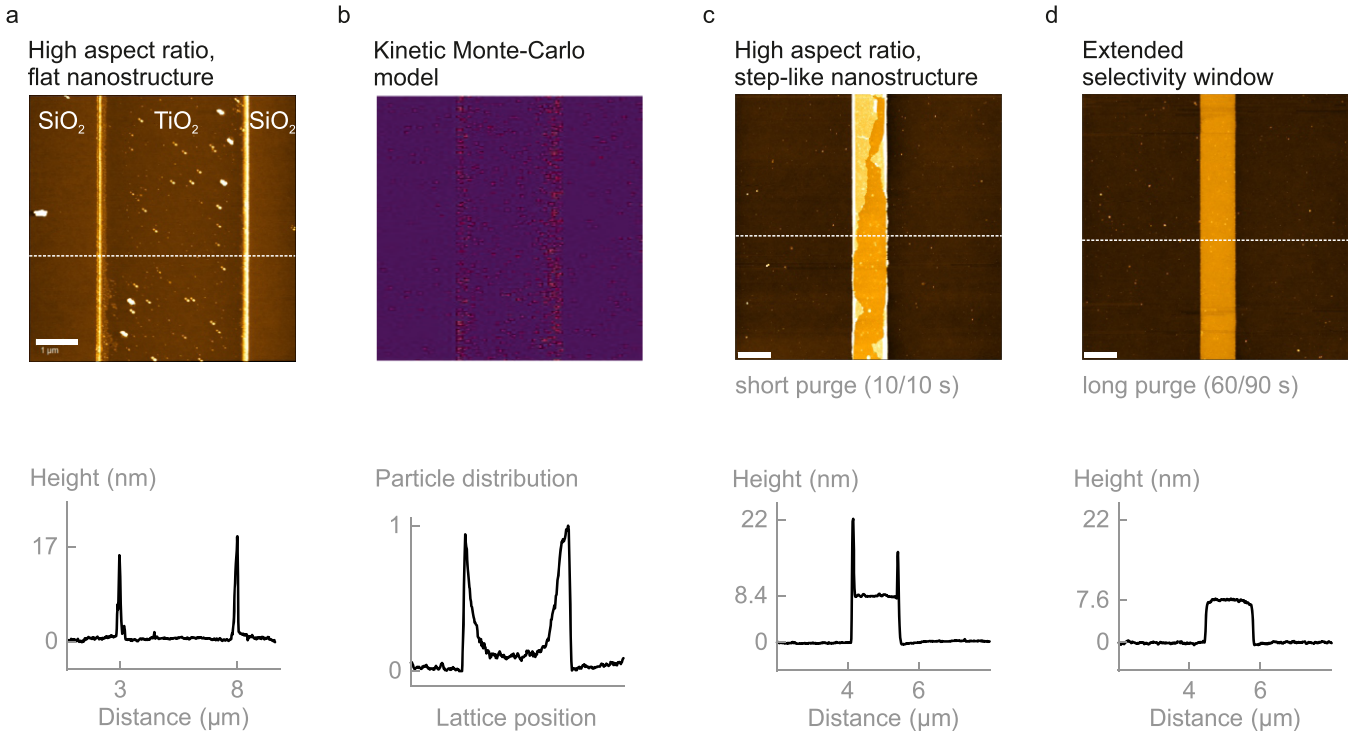

Figure 3. Surface diffusion control in area-selective ALD. (a) AFM image of a flat TiO_2 and SiO_2 nanostructure showing accumulation at the edges of the growth and no-growth areas, and the corresponding height profile. (b) Particle distribution from the kinetic Monte-Carlo model. (c) AFM image of a TiO_2 strap on SiO_2 after 100 cycles with short purge times (10/10 s $TiCl_4/H_2O$) showing accumulation at the edges and corresponding height profile. (d) AFM image of a TiO_2 strap on SiO_2 after 100 cycles with long purge times (60/90 s $TiCl_4/H_2O$) and corresponding height profile. The scale bar is 1.5 μm.

surface structure starts to change once the number of cycles reaches the end of the selectivity window. Beyond the selectivity window, the sample surface appears slightly granular, and the roughness increases, *e.g.*, to 440 pm at 75 cycles. The small grains indicate island growth of TiO_2 on PMMA. Eventually, the sample surface becomes clearly granular as the grains grow in size and begin to form a complete film (100 cycles). Here, the PMMA roughness increases to 480 pm, which is nearly double that of TiO_2 grown on SiO_2 (280 pm, *cf.* Figure S5). The topography of the thickest TiO_2 film appears globular with small grains. These results are a consequence of the nucleation mechanism of TiO_2 on PMMA. During the first 50 cycles, carboxylic acid forms under the catalytic activity of $TiCl_4$ and no apparent growth of TiO_2 on PMMA occurs. Beyond the selectivity window, the carboxylic acid presents a reactive site for nucleation and the small grains indicate the onset of TiO_2 crystallization. The formation of small grains and their density correlate with the film crystallinity.[32] Similar surface features occur for Al_2O_3 (grown from trimethylaluminum and water) and TiO_2 (grown from titanium tetrachloride and water) on other polymer surfaces.[19]

One major potential application of AS-ALD is the self-aligned fabrication of prepatterned and preprocessed devices. A reasonable target film thickness in these applications is 10 nm.[33] However, typical selectivity windows in AS-ALD are lower.[5,8,11,14,18,19] Growing thin films significantly beyond the selectivity window results in unusable structures, *e.g.*, a comparatively rough film forms on the prepatterned surface making a lift-off virtually impossible. Therefore, it is interesting to study the influence of the patterning step on the final thin film structure, especially when the film thickness is beyond the selectivity window. We prepared a series of different-sized PMMA patterns on SiO_2 (Figure S6), deposited 50 and 100 cycles of $TiCl_4/H_2O$ (*i.e.*, within and beyond the selectivity window) on the patterned substrates, followed by the lift-off of PMMA. We examined the resulting TiO_2 patterns on SiO_2 under an AFM and determined the GPC from the topography. We define the area ratio (AR) as the ratio of the no-growth to the growth area to generalize the discussion of the widths of the growth and no-growth areas (Figure S6). We find that the GPC strongly increases upon patterning (Figure 2b) and is approximately independent of the area ratio in the investigated range (Figure S7). The GPC on unpatterned substrates (bare SiO_2), which has been determined by XXR, is 0.63 Å cycle^{-1} and independent of the number of cycles. The difference to the results from Figure 1b is based on the fit of all GPC values vs. individual GPC calculations. Unexpectedly, the GPC depends on the number of cycles on patterned substrates. It is 0.63 Å cycle^{-1} when the number of cycles is 50 (black dots) and increases by 1/3 to 0.83 Å cycle^{-1} when the number of cycles is 100 (red dots). This observation is highly remarkable as the GPC should be independent of the number of cycles in an ALD process operating with saturation characteristics. Commonly, the GPC saturates because of steric hindrance of the ligands or the number of reactive surface sites.[34] In the latter case, when the growth is substrate-inhibited, the GPC is low in the beginning before settling to a constant value. This has been observed in the selective deposition of metallic platinum and ruthenium dots on silicon: the GPC decreases on patterned substrates, which is typically attributed to the polymer residue on the substrate.[31] However, this explanation does not hold here as the GPC increases on patterned substrates. Another possible process to be considered is the

https://doi.org/10.1021/acsami.0c22121
ACS Appl. Mater. Interfaces 2021, 13, 19398−19405

surface diffusion of species as the chemical nature of the PMMA and SiO_2 substrates are different.[35,36]

We analyze the topography of the patterns to gain further insight into the growth mechanism reported here. ALD processes operating with saturation characteristics typically yield large degrees of uniformity. Deviations in the form of gradients may indicate diffusion processes[36,37] and explain the increase in GPC. We etched an 8.9 nm deep trench in SiO_2 and deposited 100 cycles of $TiCl_4/H_2O$ to fill the trench. The AFM image of the resulting structure reveals a flat geometry, *i.e.*, a filled trench, with sharp spikes of up to 17 nm running vertically along the interface of the growth and no-growth areas (Figure 3a). Additionally, small grains appear on the surface. The species seem to propagate from the no-growth area toward the growth area and pile up at the interface. To analyze the particle distribution in AS-ALD processes, we employ a kinetic Monte-Carlo model of the surface diffusion of particles. The model assumes a uniform particle distribution in the growth and no-growth areas and allows the particles to diffuse until the distribution is in a steady state. The final particle distribution from the kinetic Monte-Carlo model strongly resembles the topography of the patterned samples (Figure 3b). A large number of particles accumulate in the growth area, while only a small number of particles remain in the no-growth area where they form small islands. The accumulation occurs preferably at the interface of the growth to the no-growth area, where the distribution exhibits localized spikes in agreement with the experimental findings. The accumulation of particles in the growth area explains the strongly increased GPC on patterned substrates and the accumulation at the edges. Particles diffuse from the no-growth area toward the growth area where they remain near the edges producing sharp spikes. The remaining particles in the no-growth area act as nucleation centers in the following cycles contributing to a decrease of selectivity. We further examine the influence of the model parameters on the final particle distribution and find that an increase in the number of iteration steps leads to more particles in the growth area (Figure S8). As the kinetic Monte-Carlo model reproduces the experimental observations, we conclude particle diffusion to be the origin of the increased GPC and accumulation at the interface.

A discussion of the nature of the diffusing particle is essential, as it is not obvious from an ALD process operating with saturation characteristics. In the static model, the first precursor chemisorbs at the surface in the first half-reaction and then reacts with the second precursor in the second half-reaction forming the product. All participating species chemisorb at the surface and thus are immobile. In reality, the first precursor may physisorb and diffuse on the substrate during the first half-cycle, and the product may diffuse during the second half-cycle. However, an exact differentiation of the diffusing species still remains difficult.[35]

Control of Surface Diffusion and Selectivity in Area-Selective ALD. One important issue in the application of AS-ALD for the self-aligned fabrication of integrated circuits is the size of the selectivity window. To date, no clear target thickness has been defined[4] but 10 nm appears to be reasonable.[33] Further, our results indicate that species bond only weakly to the substrate at the beginning of the ALD process. Consequently, we examine the variation of the precursor purge times as a route to control the surface diffusion of species and improve the process toward larger selectivity. We choose 100 cycles, which is outside of the inherent selectivity window of the ALD process, and vary the purge times from short (10/10 s $TiCl_4/H_2O$) to long (60/90 s). Short purge times lead to surface diffusion of weakly bonded species, which results in an accumulation at the growth to the no-growth interface (Figure 3c). The AFM image reveals a vertical strap of TiO_2 on SiO_2. The strap is 1.5 μm wide and exhibits a layered topography, which is evident from the brighter areas. The base of the strap is 8.4 nm thick and sharp spikes of up to 22 nm appear at the edges (Figure 3c). Uniform planes of larger thickness seem to propagate from these edges. One remarkable feature of those structures is the high aspect ratio of the accumulation. Fabrication of such structures in modern integrated circuits like the fins in FinFET devices requires many processing steps. Exploiting the surface diffusion in area-selective ALD enables the facile fabrication of high-aspect-ratio nanostructures. Long purge times result in a significantly extended selectivity window (Figure 3d). The TiO_2 strap is 7.6 nm thick and exhibits few defects and no accumulation at the growth to the no-growth interface. The film thickness and GPC are slightly reduced by prolonging the purge times due to reduced surface diffusion, but still significantly boosted compared to the unpatterned substrate (Figure 2b). This means that surface diffusion of species occurs, and the purge gas removes weakly bonded species on the surface such as physisorbed precursor or product molecules. An extension of the precursor purge times improves the selectivity of the AS-ALD process.

CONCLUSIONS

In conclusion, surface modifications of the substrate strongly manipulate the surface diffusion of species in area-selective deposition. The area-selective atomic layer deposition of TiO_2 on poly(methyl methacrylate) (PMMA) and SiO_2 yields localized nanostructures with tailored aspect ratios. Controlling surface diffusion enables such nanostructures as it facilitates the growth rate at the interface of the growth and no-growth areas. This straightforward strategy may enable new self-aligned fabrication schemes in area-selective deposition. Substrates can be designed to control the surface diffusion and thus deposition. Further, surface modifications accelerate the growth in the entire growth area by 1/3 as species diffuse from the no-growth to the growth areas contradicting a commonly assumed static ALD model. The inherent selectivity of the process of 50 cycles or 3.1 nm is limited by the catalytic activity of $TiCl_4$ during the formation of the carboxylic acid on PMMA. Prolonging the purge times allows the preparation of microstructures with film thicknesses well beyond the inherent selectivity of these process parameters by removing weakly adsorbed species and prolonging the diffusion time. This allows improving the selectivity toward high selectivity processes. Future work should explore the new opportunities that arise from controlling the surface diffusion of species in AS-ALD.

ASSOCIATED CONTENT

Supporting Information

The Supporting Information is available free of charge at https://pubs.acs.org/doi/10.1021/acsami.0c22121.

Growth per cycle of TiO_2 on PMMA as a function of the $TiCl_4$ and H_2O pulse times; X-ray reflectivity of TiO_2 thin films on PMMA; X-ray photoelectron spectroscopy of TiO_2 on PMMA and SiO_2; infrared absorbance of

https://doi.org/10.1021/acsami.0c22121
ACS Appl. Mater. Interfaces 2021, 13, 19398−19405

TiO_2 thin films; AFM of TiO_2 on SiO_2; PMMA patterns; growth per cycle of TiO_2 as a function of the area ratio; and particles in the growth area as a function of iteration steps (PDF)

AUTHOR INFORMATION

Corresponding Author

Sangam Chatterjee − *Institute of Experimental Physics I and Center for Materials Research (ZfM/LaMa), Justus Liebig University Giessen, Giessen D-35392, Germany;* orcid.org/0000-0002-0237-5880; Email: sangam.chatterjee@physik.uni-giessen.de

Authors

Philip Klement − *Institute of Experimental Physics I and Center for Materials Research (ZfM/LaMa), Justus Liebig University Giessen, Giessen D-35392, Germany;* orcid.org/0000-0001-7044-713X

Daniel Anders − *Institute of Experimental Physics I and Center for Materials Research (ZfM/LaMa), Justus Liebig University Giessen, Giessen D-35392, Germany*

Lukas Gümbel − *Institute of Experimental Physics I and Center for Materials Research (ZfM/LaMa), Justus Liebig University Giessen, Giessen D-35392, Germany*

Michele Bastianello − *Institute of Experimental Physics I and Center for Materials Research (ZfM/LaMa), Justus Liebig University Giessen, Giessen D-35392, Germany*

Fabian Michel − *Institute of Experimental Physics I and Center for Materials Research (ZfM/LaMa), Justus Liebig University Giessen, Giessen D-35392, Germany*

Jörg Schörmann − *Institute of Experimental Physics I and Center for Materials Research (ZfM/LaMa), Justus Liebig University Giessen, Giessen D-35392, Germany*

Matthias T. Elm − *Institute of Experimental Physics I and Center for Materials Research (ZfM/LaMa), Justus Liebig University Giessen, Giessen D-35392, Germany; Institute of Physical Chemistry, Justus Liebig University Giessen, Giessen D-35392, Germany;* orcid.org/0000-0001-7014-5772

Christian Heiliger − *Institute of Theoretical Physics and Center for Materials Research (ZfM/LaMa), Justus Liebig University Giessen, Giessen D-35392, Germany*

Complete contact information is available at: https://pubs.acs.org/10.1021/acsami.0c22121

Author Contributions

P.K. and S.C. conceived the experiments. P.K. fabricated the samples and performed the measurements, assisted by D.A., M.B., and L.G., D.A., and C.H. developed the KMC model, performed the calculations, and analyzed the results. F.M. performed the XPS measurements and analyzed the results. P.K., M.B., D.A., and S.C. co-wrote the paper. All authors discussed the results and gave approval to the final version of the manuscript.

Funding

This work is funded by the German Research Foundation (DFG) *via* the collaborative research center SFB 1083. P.K., M.B., and M.T.E. thank the German Federal Ministry of Education and Research (BMBF) for funding the Nano-MatFutur project NiKo (03XP0093). S.C. acknowledges financial support by the Heisenberg program (CH660/8).

Notes

The authors declare no competing financial interest.

ACKNOWLEDGMENTS

The authors thank Elisa Monte for the preparation of the graphical material.

ABBREVIATIONS USED

AFM, atomic force microscope
ALD, atomic layer deposition
AS, area-selective
AR, area ratio
DI, deionized
GA, growth area
GPC, growth per cycle
IPA, isopropanol
IR, infrared
KMC, Kinetic Monte-Carlo
NGA, no-growth area
PMMA, poly(methyl methacrylate)
S, selectivity
SAM, self-assembled monolayer
XPS, X-ray photoelectron spectroscopy
XRR, X-ray reflectivity

REFERENCES

(1) Parsons, G. N.; Clark, R. D. Area-Selective Deposition: Fundamentals, Applications, and Future Outlook. *Chem. Mater.* **2020**, *32*, 4920−4953.

(2) Lee, H. B. R.; Bent, S. F. A Selective Toolbox for Nanofabrication. *Chem. Mater.* **2020**, *32*, 3323−3324.

(3) George, S. M. Atomic Layer Deposition: An Overview. *Chem. Rev.* **2010**, *110*, 111−131.

(4) Mackus, A. J. M.; Merkx, M. J. M.; Kessels, W. M. M. From the Bottom-Up: Toward Area-Selective Atomic Layer Deposition with High Selectivity. *Chem. Mater.* **2019**, *31*, 2−12.

(5) Mameli, A.; Karasulu, B.; Verheijen, M. A.; Barcones, B.; Macco, B.; Mackus, A. J. M.; Kessels, W. M. M. E.; Roozeboom, F. Area-Selective Atomic Layer Deposition of ZnO by Area Activation Using Electron Beam-Induced Deposition. *Chem. Mater.* **2019**, *31*, 1250−1257.

(6) Haider, A.; Yilmaz, M.; Deminskyi, P.; Eren, H.; Biyikli, N. Nanoscale Selective Area Atomic Layer Deposition of TiO_2 Using E-Beam Patterned Polymers. *RSC Adv.* **2016**, *6*, 106109−106119.

(7) Minaye Hashemi, F. S.; Prasittichai, C.; Bent, S. F. Self-Correcting Process for High Quality Patterning by Atomic Layer Deposition. *ACS Nano* **2015**, *9*, 8710−8717.

(8) Chen, R.; Bent, S. F. Chemistry for Positive Pattern Transfer Using Area-Selective Atomic Layer Deposition. *Adv. Mater.* **2006**, *18*, 1086−1090.

(9) Mackus, A. J. M.; Mulders, J. J. L.; Van De Sanden, M. C. M.; Kessels, W. M. M. Local Deposition of High-Purity Pt Nanostructures by Combining Electron Beam Induced Deposition and Atomic Layer Deposition. *J. Appl. Phys.* **2010**, *107*, No. 116102.

(10) Vervuurt, R. H. J.; Sharma, A.; Jiao, Y.; Kessels, W. M. M.; Bol, A. A. Area-Selective Atomic Layer Deposition of Platinum Using Photosensitive Polyimide. *Nanotechnology* **2016**, *27*, No. 405302.

(11) Vos, M. F. J.; Chopra, S. N.; Verheijen, M. A.; Ekerdt, J. G.; Agarwal, S.; Kessels, W. M. M.; Mackus, A. J. M. Area-Selective Deposition of Ruthenium by Combining Atomic Layer Deposition and Selective Etching. *Chem. Mater.* **2019**, *31*, 3878−3882.

(12) Zyulkov, I.; Madhiwala, V.; Voronina, E.; Snelgrove, M.; Bogan, J.; O'Connor, R.; De Gendt, S.; Armini, S. Area-Selective ALD of Ru on Nanometer-Scale Cu Lines through Dimerization of Amino-Functionalized Alkoxy Silane Passivation Films. *ACS Appl. Mater. Interfaces* **2020**, *12*, 4678−4688.

(13) Bobb-Semple, D.; Nardi, K. L.; Draeger, N.; Hausmann, D. M.; Bent, S. F. Area-Selective Atomic Layer Deposition Assisted by Self-

Assembled Monolayers: A Comparison of Cu, Co, W, and Ru. *Chem. Mater.* **2019**, *31*, 1635−1645.
(14) Mameli, A.; Merkx, M. J. M.; Karasulu, B.; Roozeboom, F.; Kessels, W. E. M. M.; Mackus, A. J. M. Area-Selective Atomic Layer Deposition of SiO_2 Using Acetylacetone as a Chemoselective Inhibitor in an ABC-Type Cycle. *ACS Nano* **2017**, *11*, 9303−9311.
(15) Lee, H.-B.-R.; Bent, S. Nanopatterning by Area-Selective Atomic Layer Deposition. In*Atomic Layer Deposition of Nanostructured Materials*; Wiley-VCH Verlag GmbH & Co. KGaA, 2012; pp 193−225.
(16) Gladfelter, W. L. Selective Metallization by Chemical Vapor Deposition. *Chem. Mater.* **1993**, *5*, 1372−1388.
(17) Puurunen, R. L.; Vandervorst, W. Island Growth as a Growth Mode in Atomic Layer Deposition: A Phenomenological Model. *J. Appl. Phys.* **2004**, *96*, 7686−7695.
(18) Atanasov, S. E.; Kalanyan, B.; Parsons, G. N. Inherent Substrate-Dependent Growth Initiation and Selective-Area Atomic Layer Deposition of TiO_2 Using "Water-Free" Metal-Halide/Metal Alkoxide Reactants. *J. Vac. Sci. Technol., A* **2016**, *34*, No. 01A148.
(19) Kemell, M.; Färm, E.; Ritala, M.; Leskelä, M. Surface Modification of Thermoplastics by Atomic Layer Deposition of Al_2O_3 and TiO_2 Thin Films. *Eur. Polym. J.* **2008**, *44*, 3564−3570.
(20) Guo, H. C.; Ye, E.; Li, Z.; Han, M. Y.; Loh, X. J. Recent Progress of Atomic Layer Deposition on Polymeric Materials. *Mater. Sci. Eng. C* **2017**, *70*, 1182−1191.
(21) Sinha, A.; Hess, D. W.; Henderson, C. L. Area-Selective ALD of Titanium Dioxide Using Lithographically Defined Poly (Methyl Methacrylate) Films. *J. Electrochem. Soc.* **2006**, *153*, G465−G469.
(22) Wilson, C. A.; Grubbs, R. K.; George, S. M. Nucleation and Growth during Al_2O_3 Atomic Layer Deposition on Polymers. *Chem. Mater.* **2005**, *17*, 5625−5634.
(23) Sinha, A.; Hess, D. W.; Henderson, C. L. Transport Behavior of Atomic Layer Deposition Precursors through Polymer Masking Layers: Influence on Area Selective Atomic Layer Deposition. *J. Vac. Sci. Technol., B: Microelectron. Nanometer Struct.* **2007**, *25*, 1721−1728.
(24) Gong, B.; Parsons, G. N. Quantitative in Situ Infrared Analysis of Reactions between Trimethylaluminum and Polymers during Al_2O_3 Atomic Layer Deposition. *J. Mater. Chem.* **2012**, *22*, 15672−15682.
(25) Sinha, A.; Hess, D. W.; Henderson, C. L. Area Selective Atomic Layer Deposition of Titanium Dioxide: Effect of Precursor Chemistry. *J. Vac. Sci. Technol., B: Microelectron. Nanometer Struct.* **2006**, *24*, 2523−2532.
(26) Assfeld, X.; García, J.; García, J. I.; Mayoral, J. A.; Proietti, M. G.; Ruiz-López, M. F.; Sánchez, M. C. X-Ray Absorption Spectroscopy Investigation on the Structure of Methyl Acrylate-$TiCl_4$ Complexes in Solution. *J. Chem. Soc. Chem. Commun.* **1994**, 2165−2166.
(27) Shambayati, S.; Crowe, W. E.; Schreiber, S. L. On the Conformation and Structure of Organometal Complexes in the Solid State: Two Studies Relevant to Chemical Synthesis. *Angew. Chem., Int. Ed.* **1990**, *29*, 256−272.
(28) Rao, B. V. J. Properties and Structure of Glasses in the Binary Systems Alkali—TiO_2. *J. Am. Ceram. Soc.* **1964**, *47*, 455−463.
(29) Parsons, G. N. Atomic Layer Deposition on Soft Materials. In*Atomic Layer Deposition of Nanostructured Materials*; Wiley-VCH Verlag GmbH & Co. KGaA, 2012; pp 271−300.
(30) Triani, G.; Campbell, J. A.; Evans, P. J.; Davis, J.; Latella, B. A.; Burford, R. P. Low Temperature Atomic Layer Deposition of Titania Thin Films. *Thin Solid Films* **2010**, *518*, 3182−3189.
(31) Färm, E.; Kemell, M.; Ritala, M.; Leskelä, M. Selective-Area Atomic Layer Deposition Using Poly(Methyl Methacrylate) Films as Mask Layers. *J. Phys. Chem. C* **2008**, *112*, 15791−15795.
(32) Aarik, J.; Aidla, A.; Mändar, H.; Sammelselg, V. Anomalous Effect of Temperature on Atomic Layer Deposition of Titanium Dioxide. *J. Cryst. Growth* **2000**, *220*, 531−537.
(33) Murdoch, G.; Bömmels, J.; Wilson, C. J.; Gavan, K. B.; Le, Q. T.; Tőkei, Z.; Clark, W. In *Feasibility Study of Fully Self Aligned Vias for 5nm Node BEOL*, 2017 IEEE International Interconnect Technology Conference (IITC); IEEE, 2017; pp 1−4.
(34) Puurunen, R. L. Surface Chemistry of Atomic Layer Deposition: A Case Study for the Trimethylaluminum/Water Process. *J. Appl. Phys.* **2005**, *97*, No. 121301.
(35) Knez, M. Diffusion Phenomena in Atomic Layer Deposition. *Semicond. Sci. Technol.* **2012**, *27*, No. 074001.
(36) Grillo, F.; Soethoudt, J.; Marques, E. A.; Martín, L.; Van Dongen, K.; van Ommen, J. R.; Delabie, A. Area-Selective Deposition of Ruthenium by Area-Dependent Surface Diffusion. *Chem. Mater.* **2020**, *32*, 9560−9572.
(37) Cremers, V.; Puurunen, R. L.; Dendooven, J. Conformality in Atomic Layer Deposition: Current Status Overview of Analysis and Modelling. *Appl. Phys. Rev.* **2019**, *6*, No. 021302.

https://doi.org/10.1021/acsami.0c22121
ACS Appl. Mater. Interfaces 2021, 13, 19398−19405

Publication 3

Atomically Thin Sheets of Lead-Free 1D Hybrid Perovskites
Feature Tunable White-Light Emission from Self-Trapped Excitons

Philip Klement, Natalie Dehnhardt, Chuan-Ding Dong, Florian Dobener,
Samuel Bayliff, Julius Winkler, Detlev M. Hofmann, Peter J. Klar,
Stefan Schumacher, Sangam Chatterjee, and Johanna Heine

Advanced Materials **33**, 2100518 (2021), DOI: 10.1002/adma.202100518

ADVANCED MATERIALS
www.advmat.de

Atomically Thin Sheets of Lead-Free 1D Hybrid Perovskites Feature Tunable White-Light Emission from Self-Trapped Excitons

*Philip Klement, Natalie Dehnhardt, Chuan-Ding Dong, Florian Dobener, Samuel Bayliff, Julius Winkler, Detlev M. Hofmann, Peter J. Klar, Stefan Schumacher, Sangam Chatterjee, and Johanna Heine**

Low-dimensional organic–inorganic perovskites synergize the virtues of two unique classes of materials featuring intriguing possibilities for next-generation optoelectronics: they offer tailorable building blocks for atomically thin, layered materials while providing the enhanced light-harvesting and emitting capabilities of hybrid perovskites. This work goes beyond the paradigm that atomically thin materials require in-plane covalent bonding and reports single layers of the 1D organic–inorganic perovskite $[C_7H_{10}N]_3[BiCl_5]Cl$. Its unique 1D–2D structure enables single layers and the formation of self-trapped excitons, which show white-light emission. The thickness dependence of the exciton self-trapping causes an extremely strong shift of the emission energy. Thus, such 2D perovskites demonstrate that already 1D covalent interactions suffice to realize atomically thin materials and provide access to unique exciton physics. These findings enable a much more general construction principle for tailoring and identifying 2D materials that are no longer limited to covalently bonded 2D sheets.

1. Introduction

Layered organic–inorganic perovskites offer considerable potential for solar cells and other optoelectronic devices as they retain the high-performing properties of 3D halide perovskites with high power conversion efficiency and improved long-term and environmental device stability.[1] Conceptually, these layered materials can be understood as cut-outs across different crystallographic directions of the parent perovskite AMX_3 (A = small organic or inorganic cation like Cs^+ or $CH_3NH_3^+$; M = divalent metal like Pb^{2+} or Sn^{2+}; X = Cl, Br or I). This is achieved by using larger organic cations like primary alkyl- or aryl ammonium ions.[2] The resulting 2D structure can be considered an ideal quantum well of one inorganic layer confined by two organic barriers. The optical properties of such quantum wells can be tuned by varying the thickness of the inorganic layer,[3] and the freedom in combining the inorganic and organic components of the material offers a rich chemical, structural, and optical tunability.[4] These materials pave the way to the design of 2D materials as the building blocks can be chosen deliberately. Established 2D materials provide an excellent platform for fundamental research and applications including fundamental physical phenomena such as polaritons,[5] superconductivity,[6] and charge-density waves[7] as well as applications such as water purification,[8] light-emitting diodes,[9] photovoltaics,[10] and sensing.[11] This wide range inherently infers that combinations of layered perovskites and 2D materials will provide advanced multi-functional structures combining many properties.

P. Klement, Dr. F. Dobener, Prof. D. M. Hofmann, Prof. P. J. Klar, Prof. S. Chatterjee
Institute of Experimental Physics I and Center for Materials Research (ZfM/LaMa)
Justus Liebig University Giessen
Heinrich-Buff-Ring 16, Giessen D-35392, Germany

The ORCID identification number(s) for the author(s) of this article can be found under https://doi.org/10.1002/adma.202100518.

© 2021 The Authors. Advanced Materials published by Wiley-VCH GmbH. This is an open access article under the terms of the Creative Commons Attribution-NonCommercial-NoDerivs License, which permits use and distribution in any medium, provided the original work is properly cited, the use is non-commercial and no modifications or adaptations are made.

DOI: 10.1002/adma.202100518

Dr. N. Dehnhardt, J. Winkler, Dr. J. Heine
Department of Chemistry and Material Sciences Center
Philipps-Universität Marburg
Hans-Meerwein-Straße, Marburg D-35043, Germany
E-mail: johanna.heine@chemie.uni-marburg.de
Dr. C.-D. Dong, Prof. S. Schumacher
Department of Physics and Center for Optoelectronics and Photonics Paderborn (CeOPP)
Paderborn University
Warburger Strasse 100, Paderborn D-33098, Germany
S. Bayliff
School of Physics and Astronomy
University of Minnesota
116 Church Street S.E., Minneapolis, MN 55455, USA
Prof. S. Schumacher
Wyant College of Optical Sciences
The University of Arizona
1630 E. University Blvd., Tucson, AZ 85721, USA

More recent additions to the family of 2D materials include layered 2D perovskites.[12–15] In principle, any layered material with only weak van der Waals forces acting between its comparatively strongly bound layers can be exfoliated.[16] The limiting factors and problems in the investigation of free-standing single layers of such layered 2D perovskites have been manifold: 1) Early reports suggested that the quantum well is effectively isolated by the organic layers,[17] which means that the properties of the single layer and bulk crystal should be the same. Further, 2) strong in-plane interactions in only two dimensions, typically realized by covalent bonds, were deemed mandatory for the formation of free-standing single layers. Even further, (3) the technical difficulty of separating and analyzing individual layers has led to only few reports.[13]

Going beyond the state-of-the-art, we successfully combine the concepts of layered perovskites and atomically thin materials to establish a to date inaccessible class of hybrid materials with unique exciton physics, namely self-trapping in low-dimensional materials. We present $[C_7H_{10}N]_3[BiCl_5]Cl$ (BBC), as a principle example of single crystalline organic–inorganic hybrid materials that feature only 1D, wire-like covalent interactions within their layers. This surpasses the conventional paradigm of in-plane covalent bonds being mandatory for atomically thin 2D materials. We find ultrathin crystals of excellent quality with spectrally broadband, white-light emission across the visible spectrum originating from self-trapped excitons (STEs). Ultrathin sheets reveal an extremely strong shift of the emission energies due to the thickness dependence of the exciton self-trapping. This suggests that single-crystalline compounds featuring lamellar supramolecular motifs can be understood as 2D materials, leading towards a general construction principle for identifying and creating tailored functional 2D materials even when no 2D covalent interactions are present within the individual layers.

2. Results and Discussion

2.1. Synthesis and Structural Characterization of BBC

An illustration of the concept of BBC shows the main interactions in the material (**Figure 1**a). The strong ionic and supramolecular interactions in the inorganic layer and the weak van der Waals interactions between individual layers corroborate the 2D nature of the compound. The reaction of benzylamine with a solution of Bi_2O_3 in concentrated hydrochloric acid yields large, colorless plates of BBC (Figure 1b). Most plates are rectangular in shape with truncated ends, reflecting the mechanically brittle structure. The product yield of this straight-forward synthesis was 52%. We have confirmed the single-crystal structure and high crystallinity of BBC by X-ray diffraction measurements (Figure S2, Supporting Information). BBC crystallizes in the $P2_1/c$ space group of the monoclinic crystal system, and exhibits a preferred orientation along the (100) direction, which reflects the layered structure and plate habit. The out-of-plane spacing between two layers is 1.7 nm. The lattice parameters are summarized in the Supporting Information (Table S1, Supporting Information). The crystal structure shows the hybrid nature of the compound (Figure 1c). Benzylammonium (BzA) cations are arranged in flat layers, with C—H···π interactions between the

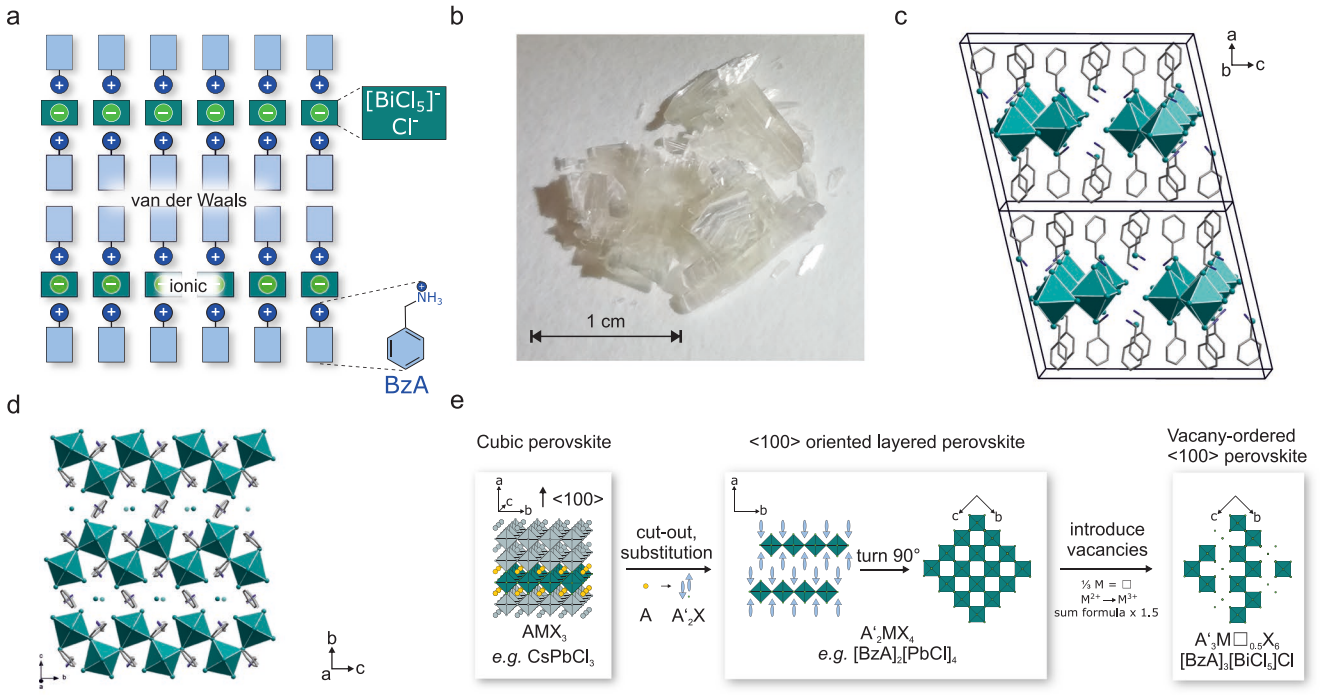

Figure 1. Concept, crystal structure, and derivation of BBC. a) Illustration of the layered structure of BBC with strong ionic and supramolecular interactions in the inorganic layer, and weak van der Waals interactions between individual layers. b) Photograph of large, colorless BBC crystals. c) Layered crystal structure of BBC with Cl atoms in green, C atoms in grey, and H atoms omitted for clarity. d) Individual layers are assembled from 1D chlorobismuthate chains. e) Schematic derivation of BBC as a cut-out of the perovskite aristotype.

© 2021 The Authors. Advanced Materials published by Wiley-VCH GmbH

benzene rings. This enforces the equally flat arrangement of the $[BiCl_5]^{2-}$ chloro-bismuthate chains, resulting in an overall lamellar structure. Additional chloride ions are found above and below the metalate-ion-plane, completing the compound's charge balance. The crystal structure can be viewed as a bulk arrangement of 1D quantum wires with the inorganic BzA cations surrounding individual chloro-bismuthate chains that are based on corner-sharing octahedral $BiCl_6$ units (Figure 1d). The motif in BBC is reminiscent of 2D lead-halide perovskites such as $(BzA)_2[PbCl_4]$[18] and conceptually derived from the cubic perovskite aristotype (Figure 1e). Within the cubic perovskite, each cation A is replaced by two larger organic cations A′ such as BzA and an additional halide ion X^- for overall charge balance. This way, <100>-oriented layered perovskites of composition A'_2MX_4 are derived. Next, a third of the metal atoms in each of the <100> layers is removed, and the charge on each metal is increased from 2+ to 3+ to maintain charge neutrality. The result is a vacancy-ordered <100> perovskite with *cis*-connected MX_5 chains and additional halide ions completing each individual layer. BBC is the first ordered example of a group 15 hybrid organic–inorganic halogenido metalate that is described as a vacancy-ordered 2D perovskite of the <100> family.[2,19] Only one singular, yet intrinsically disordered example of a hybrid iodido bismuthate of this family exists to date: $(H_2AEQT)M_{2/3}I_4$ (M = Bi or Sb; AEQT = 5,5‴-bis-(aminoethyl)-2,2′:5′,2″:5″,2‴-quaterthiophene);[20] it features statistically disordered vacancies at all metal positions and the use of a diammonium cation prevents exfoliation in this case.

2.2. Electronic Band Structure and Exfoliation of BBC

The conventional belief that 2D covalent interactions are an essential prerequisite for stable 2D materials suggests that the mechanical exfoliation should not be possible for BBC.[12] We investigate the mechanical exfoliation process of BBC despite this paradigm. Microscopic modeling evaluates its ability for exfoliation, any possible cleavage plane(s), and compares BBC to well-established 2D materials (Figure S4, Supporting Information). The required energy for expansions of the unit cell along the three crystallographic axes indicates the solute binding of BBC along the *a*-axis and determines the cleavage plane to the *b*-*c*-plane of the crystal. The calculated crystal structure of the single layer shows only a slight rearrangement of the organic molecules as the unit cell is expanded along the *a*-axis. This predicts excellent preservation of the individual sheets upon exfoliation.

The density functional theory (DFT) calculations also allow insight into the electronic properties of BBC. The density of states calculated by using the HSE06 hybrid functional yields a band-gap energy of 3.62 eV (**Figure 2**a), which increases to 3.67 eV when the thickness is reduced to a single layer (Figure 2b). The corresponding band structures show very narrow bandwidths and direct gaps located at the Γ-point (Figure S5a,b, Supporting Information). The flat bands indicate that the electronic states are highly localized. Only the conduction band (CB) shows some dispersion around the Γ-point indicating delocalization along the wires. The charge-density map of the CB confirms that the states are confined to the $[BiCl_5]^{2-}$ anions (Figure 2c), and mainly contributed by the Bi and Cl orbitals in the calculated density of states (Figure S5d,e, Supporting Information). The localization of the valence band (VB) slightly increases from the bulk crystal to the single layer. In the bulk crystal, the bands are formed by hybridization of C orbitals from the BzA cations with Cl orbitals from the $[BiCl_5]^{2-}$ anions as suggested by the charge-density map of the VB (Figure S5d, Supporting Information). In the single layer, the C orbitals shift to lower energies leaving the exclusive contribution by Cl orbitals and consequent localization to the $[BiCl_5]^{2-}$ anions. We find no indication for lattice distortion. These results indicate strong charge localization in the inorganic chains of BBC with neglectable interchain coupling, especially in the single layer. Therefore, upon photoexcitation each chloro-bismuthate chain can act as an efficient 1D luminescence center by trapping of excitons.

We have verified the existence of free-standing single layers of BBC by mechanically exfoliating single crystals yielding ultrathin sheets down to the single layer. The procedure is similar to the technique that is successfully applied to common van der Waals materials. Typical ultrathin BBC sheets on SiO_2/Si substrates exhibit lateral dimensions of a few micrometers—similar to other 2D materials (Figure 2d). Various samples of only a few unit cell thicknesses have been realized this way featuring reduced lateral dimensions (less than 1 μm). The structure appears mechanically brittle. The comparison of the expansion energies of the 2D sheets of BBC and common 2D materials like graphene and molybdenum disulfide (MoS_2) reveals that significantly less energy is required to expand the 2D sheet of BBC explaining our observations (Figure S4, Supporting Information). The ultrathin sheets are reasonably stable in air—at least on the order of days—and long-term stable in inert atmospheres like Ar and in vacuum, where they sustain repeated thermal cycling to cryogenic temperatures without damage. Degradation after 15 weeks of storage under ambient conditions becomes apparent by a reduced thickness and a deterioration of the surface topography (Figure S6, Supporting Information), and is likely caused by hydrolysis.[21] Optical bright-field microscopy and atomic force microscopy of ultrathin sheets reveal smooth and uniform surfaces highlighting the good crystal quality (Figure 2e). The thicknesses of the sheets range from several hundreds to only a few nanometer. The thinnest sheets are 3 nm thick (Figure 2f) which corresponds to a single layer of BBC as this is significantly less than twice the corresponding layer spacing along the *a*-axis of the bulk crystal. Apparently, substrate interactions increase the observed thickness of the first attached layer.[12,22]

2.3. Thickness-Dependent Optical Properties of Ultrathin BBC

BBC displays strong, broadband emission across the visible spectrum originating from STEs. The absorption spectrum (**Figure 3**a) shows the onset of absorption at 3.3 eV (375 nm), and a resonance at 3.5 eV (354 nm), which we identify with the fundamental bright exciton resonance. The increased band-gap energy compared to 3D perovskites is assigned to the increased quantum confinement in the 1D structure. The photoluminescence (PL) of bulk BBC crystals centers at E_{STE} = 1.87 eV

© 2021 The Authors. Advanced Materials published by Wiley-VCH GmbH

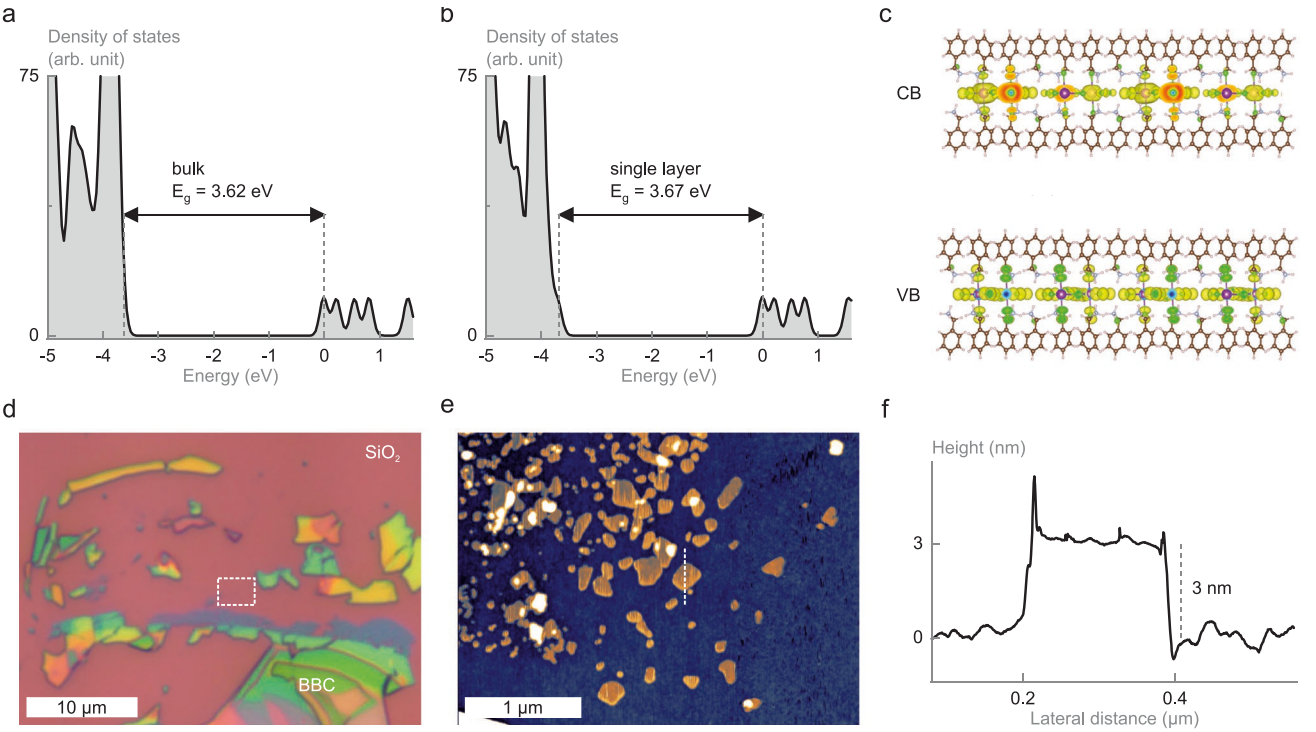

Figure 2. Electronic band-structure and exfoliation of BBC. a,b) Calculated density of states of bulk and single layer BBC. Bulk and single layer BBC exhibit bandgaps of 3.62 and 3.67 eV. The conduction band peaks are aligned to 0 energy for better comparability. c) Conduction band (CB) and valence band (VB) associated with charge-density maps of single layer BBC. CB and VB are mainly confined to the inorganic chloro-bismuthate chains. d) Typical bright-field microscopy image of mechanically exfoliated ultrathin BBC sheets on a SiO_2/Si substrate. e) AFM image of the area highlighted by the white rectangle in (c) showing single layers (orange). f) Height profile of a single layer highlighted by the white dashed line in (d). The thickness of the single layer is 3 nm.

(663 nm) with a large full width at half maximum (FWHM) of 0.53 eV (185 nm) making BBC a potential broadband emission material. The large Stokes shift of 1.6 eV (466 nm) is among the highest values reported for any solid-state light-emitting material.[23] Broadband emissions with large Strokes shifts are typically associated with STE, that form in materials with deformable lattice and localized carriers,[24–26], that is, strong electron-phonon coupling and the absence of deep defects within the bandgap.[27] An additional, much weaker PL feature with a comparatively small FWHM appears near 3 eV. We attribute this to the free exciton transition (FX), which is Stokes-shifted by 0.5 eV due to the strong electron-phonon coupling in the material.

We quantify the electron-phonon coupling by deriving the Huang–Rhys factor S from the temperature dependence of the PL within a configuration coordinate model (CCM).[25] While the peak PL emission energy shifts slightly toward lower energies with increasing lattice temperature, its bandwidth extends considerably with the FWHM increasing from 0.53 to 0.73 eV (185 to 260 nm) yielding a large $S = 45$ with the phonon frequency of the excited state $\hbar\Omega_e = 32$ meV (Figure S7a,b, Supporting Information). From these data, we estimate the exciton self-trapping time to $\tau = 2\pi/\Omega_e = 129$ fs, which indicates the ultrafast STE formation. The temperature dependence of the absorption yields the phonon frequency of the ground state $\hbar\Omega_g = 19$ meV (Figure S7c, Supporting Information), and the lattice-deformation energy $E_d = S\hbar\Omega_g = 0.86$ eV. We confirm the absence of deep defects within the bandgap by PL excitation (PLE) spectroscopy of the white-light emission at 1.9 eV (Figure 3b). The PLE intensity reveals a strong exciton peak at 3.4 eV followed by a continuum contribution peaking at 3.7 eV. The shape of the exciton peak is similar to low-dimensional Wannier-like absorption patterns[28,29] and reflects the low-dimensional structure of BBC.[4] The energy difference of the exciton resonance and the continuum of 0.3 eV yields an estimation of the exciton binding-energy of 10 to 75 meV for mixed-dimensional confinement.[4] Importantly, the PLE intensity decreases to nearly zero below the bandgap, and we observe no PLE intensity near 1.9 eV. A comparison of PLE spectra of the STE and FX emission reveals identical shapes and features indicating that the white-light emission originates from the same excited state (Figure S7e, Supporting Information). Further, the PL intensity increases linearly with the excitation power in the investigated range (Figure S7f, Supporting Information), indicating that there is neither a threshold for the onset of PL due to non-radiative recombination through defects at low excitation powers nor saturation of the absorption at high excitation powers or multi-photon absorption. These experimental observations of strong electron-phonon coupling and absence of any indications of strong defect emission confirm the origin of the white-light emission as STE rendering BBC a 2D material candidate with functionality as white-light source. We measured the PL lifetime of the STE state by time-resolved PL (Figure 3c). The transient shows a bi-exponential decay after the laser excitation

© 2021 The Authors. Advanced Materials published by Wiley-VCH GmbH

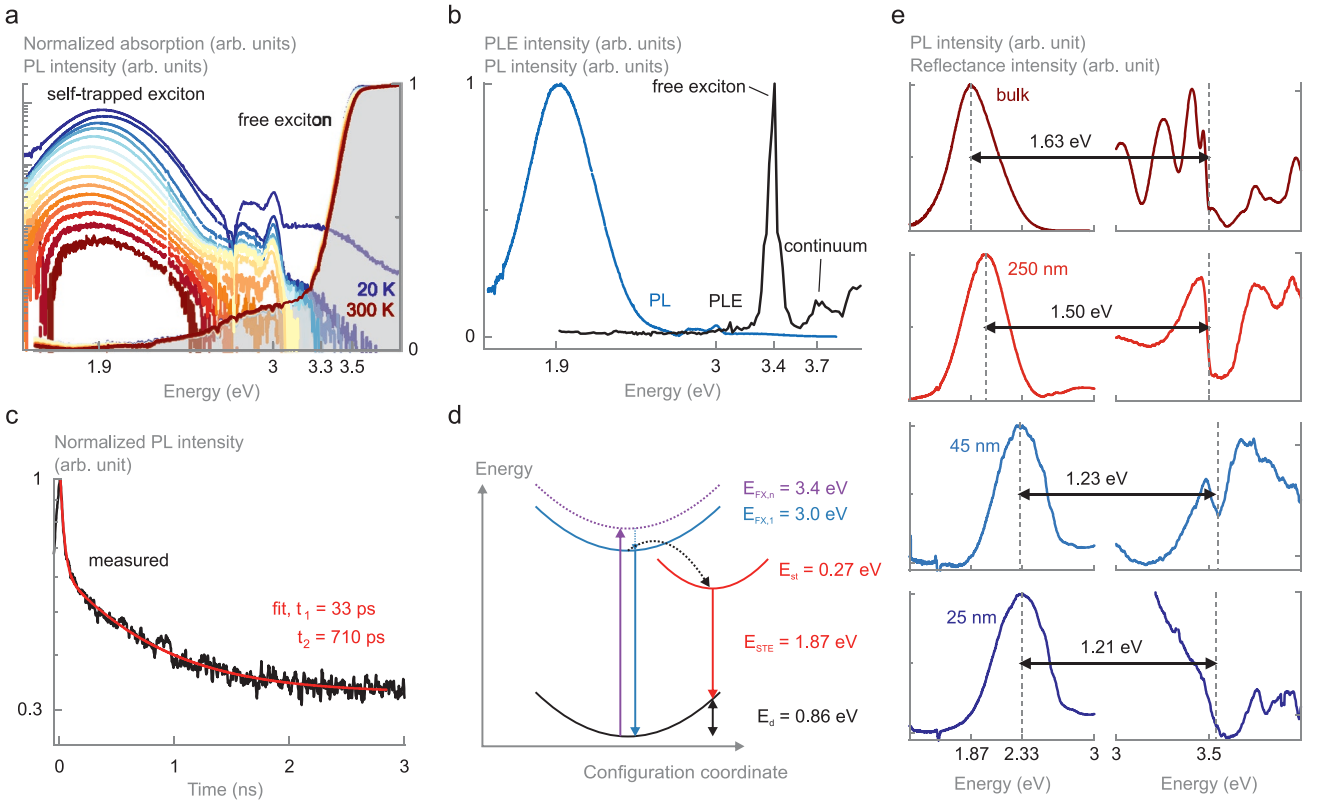

Figure 3. Thickness-dependent optical properties of self-trapped excitons in BBC. a) Absorption and photoluminescence (PL) of a bulk crystal as a function of temperature. PL spectra exhibit white-light emission across the visible spectrum from self-trapped excitons (STE) and a narrow emission from free excitons (FX). b) Photoluminescence excitation and PL spectra of a bulk crystal showing no defect-related emission. c) Time-resolved PL of the STE emission near 1.9 eV of a bulk crystal showing a luminescence lifetime of 710 ps. d) Configuration coordinate diagram of the STE and FX formation in BBC. The arrows represent lattice relaxations and optical transitions. e) Thickness-dependent PL and differential reflectance spectra of ultrathin BBC. The STE emission shifts to higher energies by 0.46 eV when the thickness decreases, whereas the bandgap only shifts by 0.04 eV.

with lifetimes of τ_1 = 33 ps and τ_2 = 710 ps, which are comparable to other few-layered Pb-based 2D perovskites.[12,15]

These experimental findings allow us to establish an energy-level diagram of BBC based on the CCM (Figure 3d). After photoexcitation at or above the exciton absorption resonance energy E_g = 3.4 eV, we find emission at E_{FX} = 3 eV and an ultrafast transfer to the self-trapped state which is calculated to 129 fs. The observation of a self-trapped state is consistent with the deformable lattice of BBC and the absence of a potential barrier for the formation of STE in 1D structures as opposed to 3D systems.[24] The self-trapping energies and the lattice-deformation energies are the differences of the excited-state energies and ground-state energy between the STE and FX and amount to E_{st} = 0.27 eV and E_d = 0.86 eV, respectively. STEs recombine after the PL lifetime of 710 ps with the emission energy $E_{STE} = E_{FX} - E_b - E_{st} - E_d = 1.87$ eV. The zero-phonon line (ZPL) $E_{ZPL} = E_{STE} + S\hbar\Omega_e = 3.1$ eV from the CCM coincides with the narrow PL feature at 3 eV confirming the identification with the FX. Importantly, the 1D structure of BBC allows for STE formation and the confinement of electrons and holes to the inorganic chain renders the STE transition radiative. Thus, BBC can be considered as a potential white-light emitter.

We examine the evolution of the characteristic lattice vibrations of the bulk crystal and several ultrathin sheets by resonant and non-resonant Raman spectroscopy (Figure S8, Supporting Information). The non-resonant Raman spectra are typical for 1D structures with an octahedral arrangement of halogen atoms with two chlorine bridges linking two adjacent bismuth atoms. We attribute the peaks at 284, 249, 237, and 161 cm^{-1} to Bi-Cl stretching vibrations ($2A_1$, B_1, E_1) and the peaks at 106 and 80 cm^{-1} to Ci–Bi–Cl bending vibrations.[30] The intensity of the peaks decreases with the sample thickness and eventually vanishes for ultrathin sheets indicating weak Raman scattering efficiencies. We find that the Raman spectra change significantly between resonant and non-resonant excitation. This provides corroborating yet more direct experimental evidence for self-trapping as we find that optical excitation deforms the lattice.

The unique combination of the chain-like 1D structure of BBC with the formation of STE and the layered crystal structure with exfoliation of ultrathin sheets make the investigation of the thickness dependence of the STE possible. We measure the PL and differential reflectance spectra of ultrathin sheets of BBC as a function of the sample thickness (Figure 3e). Bulk crystals and ultrathin sheets display spectrally broadband emission. The emission energy shifts by as much as 0.46 eV to higher energies from 1.87 (663 nm) to 2.33 eV (532 nm) as the sample thickness reduces, while the FWHM stays constant. The

© 2021 The Authors. Advanced Materials published by Wiley-VCH GmbH

occurrence and the magnitude of the shift are highly remarkable as the latter is at least one order of magnitude larger than that found for FX-related PL in 2D hybrid perovskites.[12,13,31] This presumably represents the first observation of a thickness-dependent shift of the STE emission in a perovskite material. We identify its origin from the variation of the differential reflectance: the band-gap energy shifts only slightly to higher energies by 0.04 eV from 3.50 (354 nm) to 3.54 eV (350 nm) in stark contrast to the STE PL energy. This is consistent with the results from our DFT calculations that show only a slightly increased carrier localization in the single layer (Figure 2 and Figure S5, Supporting Information) compared to the bulk. The Stokes shift, which is the sum of the exciton binding-energy, self-trapping energy, and lattice-deformation energy, reduces from 1.63 eV in the bulk crystal to 1.21 eV in the ultrathin sheet. We exclude increased quantum confinement and reduced dielectric screening in the ultrathin sheets as the origin of the STE PL shift as the bandgap is almost independent of the sample thickness in our experiments, and the exciton binding-energy was found to be independent of the sample thickness as well.[13,15] Consequently, the large STE PL shift is directly related to the thickness dependence of the STE and its vibrational coupling. Both, the self-trapping energy and the lattice-deformation energy decrease in ultrathin samples shifting the STE emission to higher energies rendering self-trapping of excitons weaker in the single-layer limit. The 1D hybrid material BBC thus provides an excellent platform for fundamental research and promising applications. The thickness dependence of the exciton self-trapping down to the single-layer limit is of fundamental interest. It may be used to tune the emission color by simply changing the crystal or film thickness. We anticipate that these results will encourage research on novel 1D hybrid materials for next-generation lighting technologies.

3. Conclusion

We successfully combine the concepts of layered perovskites and atomically thin materials and establish a new class of hybrid materials with unique exciton physics. The existence of single layers of BBC contradicts the apparent paradigm that atomically thin 2D materials require only 2D covalent interactions. BBC is a vacancy-ordered, layered perovskite of the <100> family and features only 1D, wire-like covalent interactions within its layers. The ionic and supramolecular interactions present in this compound are strong enough to allow for mechanical exfoliation of bulk crystals down to single layers. We find ultrathin crystals of excellent quality with white-light emission across the visible spectrum originating from STE that form due to the 1D structure. Ultrathin sheets reveal an extremely strong shift of the emission energy due to the thickness dependence of the exciton self-trapping, which allows the facile color tuning of white-light emitters by changing the film thickness. These findings enable a general construction principle for identifying and creating tailored, custom-functionalized 2D materials where specific functionalities are introduced both in the organic and the inorganic parts of the materials. This class of materials enables interface-controlled device integration of brightly luminescent 1D and 0D hybrid perovskites and offers a promising pathway for the non-covalent functionalization of classical 2D materials through heterostructures.

4. Experimental Section

Synthesis: Bi_2O_3 (233 mg, 0.5 mmol) was dissolved in 10 mL of concentrated hydrochloric acid (37%). A stoichiometric amount of benzylamine (0.33 mL, 3 mmol) was added. The solution was stirred and heated to reflux for 30 min, then left to cool to room temperature undisturbed. $[BzA]_3[BiCl_5]Cl$ (193 mg, 0.26 mmol, 52%) was obtained as large colorless crystals. CHN Data: Anal. Calcd for $C_{21}H_{30}BiCl_6N_3$, (M = 746.16 g mol^{-1}): C, 33.80; H, 4.05; N, 5.63%. Found: C, 33.83; H, 4.06; N, 5.64%.

Single Crystal X-Ray Data Brief: Monoclinic, space group $P2_1/c$ (no. 14), a = 17.0182(8) Å, b = 7.6205(4) Å, c = 22.4391(9) Å, β = 102.638(2)°, V = 2839.6(2) $Å^3$, Z = 4, T = 100 K, R_1 = 0.0565 ($I > 2\sigma(I)$), wR_2 = 0.1268 (all data). Additional details on data collection and structure refinement can be found in the Supplementary Information. CCDC 1952283 contains the supplementary crystallographic data for this paper. These data can be obtained free of charge from The Cambridge Crystallographic Data Centre via www.ccdc.cam.ac.uk/data_request/cif.

Modeling: DFT calculations were performed using projector-augmented wave potentials and plane-wave basis sets, as implemented in the VASP software package. The PBE functional and Tkatchenko–Scheffler method were used to describe exchange-correlation and dispersion interaction, respectively. HSE06 hybrid functional was used to calculate the density of states as well as the partial charge densities with spin-orbital coupling (SOC) included. In addition, band structure calculations were performed by using PBE functional with SOC.

Mechanical Exfoliation and Atomic Force Microscopy: Ultrathin sheets of $[BzA]_3[BiCl_5]Cl$ were produced by exfoliation of bulk single-crystals onto Si substrates with a 275 nm-thick wet-thermal oxide layer. Thin sheets were identified by optical contrast imaging and confirmed by atomic force microscopy (AFM, AIST-NT SmartSPM 1000). Noncontact tapping mode was used to avoid sample damage.

Optical Measurements: All optical measurements were conducted at cryogenic helium temperatures with the samples in vacuum. For PL and μ-PL measurements, samples were excited at 266 nm (4.66 eV). The spot diameters and excitation powers were 200 μm, 65 μW, and 1 μm, 1.4 μW, respectively. Radiation from a combined deuterium and tungsten lamp was used for absorption and μ-reflectance measurements (spot diameters of 300 and 1 μm, respectively). For PLE measurements, samples were excited with 50 fs pulses at a fluence of (2200 ± 375) μJ cm^{-2}. For μ-TRPL measurements, samples were excited with 120 fs pulses at 266 nm (1 μm spot diameter, 1.4 μW).

Detailed methods are given in the Supporting Information.

Supporting Information

Supporting Information is available from the Wiley Online Library or from the author.

Acknowledgements

This work is funded by the German Research Foundation (DFG) via the collaborative research center SFB 1083. S.C. acknowledges financial support by the Heisenberg programme (CH660/8). C.-D.D. and S.S. acknowledge funding through project SCHU 1980/13 and through the Heisenberg programme (No. 270619725). A grant for computing time at the Paderborn Center for Parallel Computing (PC^2) is also gratefully acknowledged. N.D. thanks the Fonds der Chemischen Industrie and the Studienstiftung des Deutschen Volkes for their support. S.B. thanks the DAAD/RISE program for a research internship. J.H. thanks Prof. Stefanie

© 2021 The Authors. Advanced Materials published by Wiley-VCH GmbH

Dehnen for her constant support. The authors thank Elisa Monte for the preparation of graphical materials.

Open access funding enabled and organized by Projekt DEAL.

Conflict of Interest

The authors declare no conflict of interest.

Data Availability Statement

The data that support the findings of this study are available from the corresponding author upon reasonable request.

Keywords

2D materials, dimensionality, exfoliation, hybrid perovskites, self-trapped excitons, white-light emission

Revised: February 25, 2021
Published online: May 5, 2021

[1] L. Etgar, *Energy Environ. Sci.* **2018**, *11*, 234.
[2] B. Saparov, D. B. Mitzi, *Chem. Rev.* **2016**, *116*, 4558.
[3] J.-C. Blancon, H. Tsai, W. Nie, C. C. Stoumpos, L. Pedesseau, C. Katan, M. Kepenekian, C. M. M. Soe, K. Appavoo, M. Y. Sfeir, S. Tretiak, P. M. Ajayan, M. G. Kanatzidis, J. Even, J. J. Crochet, A. D. Mohite, *Science* **2017**, *355*, 1288.
[4] D. B. Straus, C. R. Kagan, *J. Phys. Chem. Lett.* **2018**, *9*, 1434.
[5] T. Low, A. Chaves, J. D. Caldwell, A. Kumar, N. X. Fang, P. Avouris, T. F. Heinz, F. Guinea, L. Martin-Moreno, F. Koppens, *Nat. Mater.* **2017**, *16*, 182.
[6] V. Fatemi, S. Wu, Y. Cao, L. Bretheau, Q. D. Gibson, K. Watanabe, T. Taniguchi, R. J. Cava, P. Jarillo-Herrero, *Science* **2018**, *362*, 926.
[7] X. Xi, L. Zhao, Z. Wang, H. Berger, L. Forró, J. Shan, K. F. Mak, *Nat. Nanotechnol.* **2015**, *10*, 765.
[8] Z. Teng, N. Yang, H. Lv, S. Wang, M. Hu, C. Wang, D. Wang, G. Wang, *Chem* **2019**, *5*, 664.
[9] J. S. Ross, P. Klement, A. M. Jones, N. J. Ghimire, J. Yan, D. G. Mandrus, T. Taniguchi, K. Watanabe, K. Kitamura, W. Yao, D. H. Cobden, X. Xu, *Nat. Nanotechnol.* **2014**, *9*, 268.
[10] A. Pospischil, M. M. Furchi, T. Mueller, *Nat. Nanotechnol.* **2014**, *9*, 257.
[11] P. Klement, C. Steinke, S. Chatterjee, T. O. Wehling, M. Eickhoff, *2D Mater.* **2018**, *5*, 045025.
[12] L. Dou, A. B. Wong, Y. Yu, M. Lai, N. Kornienko, S. W. Eaton, A. Fu, C. G. Bischak, J. Ma, T. Ding, N. S. Ginsberg, L. W. Wang, A. P. Alivisatos, P. Yang, *Science* **2015**, *349*, 1518.
[13] O. Yaffe, A. Chernikov, Z. M. Norman, Y. Zhong, A. Velauthapillai, A. Van Der Zande, J. S. Owen, T. F. Heinz, *Phys. Rev. B* **2015**, *92*, 045414.
[14] S. Yang, W. Niu, A. L. Wang, Z. Fan, B. Chen, C. Tan, Q. Lu, H. Zhang, *Angew. Chem., Int. Ed.* **2017**, *56*, 4252.
[15] Q. Zhang, L. Chu, F. Zhou, W. Ji, G. Eda, *Adv. Mater.* **2018**, *30*, e1704055.
[16] V. Nicolosi, M. Chhowalla, M. G. Kanatzidis, M. S. Strano, J. N. Coleman, *Science* **2013**, *340*, 1226419.
[17] T. Ishihara, J. Takahashi, T. Goto, *Phys. Rev. B* **1990**, *42*, 11099.
[18] W. Q. Liao, Y. Zhang, C. L. Hu, J. G. Mao, H. Y. Ye, P. F. Li, S. D. Huang, R. G. Xiong, *Nat. Commun.* **2015**, *6*, 7338.
[19] L. Mao, C. C. Stoumpos, M. G. Kanatzidis, *J. Am. Chem. Soc.* **2019**, *141*, 1171.
[20] D. B. Mitzi, *Inorg. Chem.* **2000**, *39*, 6107.
[21] J. L. Xie, Z. Q. Huang, B. Wang, W. J. Chen, W. X. Lu, X. Liu, J. L. Song, *Nanoscale* **2019**, *11*, 6719.
[22] C. J. Shearer, A. D. Slattery, A. J. Stapleton, J. G. Shapter, C. T. Gibson, *Nanotechnology* **2016**, *27*, 125704.
[23] C. Zhou, H. Lin, H. Shi, Y. Tian, C. Pak, M. Shatruk, Y. Zhou, P. Djurovich, M. H. Du, B. Ma, *Angew. Chem., Int. Ed.* **2018**, *57*, 1021.
[24] K. S. Song, R. T. Williams, *Self-Trapped Excitons*, Springer, Berlin, Germany **1993**.
[25] W. Stadler, D. M. Hofmann, H. C. Alt, T. Muschik, B. K. Meyer, E. Weigel, G. Müller-Vogt, M. Salk, E. Rupp, K. W. Benz, *Phys. Rev. B* **1995**, *51*, 10619.
[26] J. Luo, X. Wang, S. Li, J. Liu, Y. Guo, G. Niu, L. Yao, Y. Fu, L. Gao, Q. Dong, C. Zhao, M. Leng, F. Ma, W. Liang, L. Wang, S. Jin, J. Han, L. Zhang, J. Etheridge, J. Wang, Y. Yan, E. H. Sargent, J. Tang, *Nature* **2018**, *563*, 541.
[27] S. Kahmann, E. K. Tekelenburg, H. Duim, M. E. Kamminga, M. A. Loi, *Nat. Commun.* **2020**, *11*, 2344.
[28] R. J. Elliott, *Phys. Rev.* **1957**, *108*, 1384.
[29] C. Tanguy, P. Lefebvre, H. Mathieu, R. J. Elliott, *J. Appl. Phys.* **1997**, *82*, 798.
[30] F. Cariati, G. Marcotrigiano, L. Menabue, F. Morazzoni, G. C. Pellacani, G. M. Zanderighi, *Spectrochim. Acta, Part A* **1978**, *34*, 801.
[31] R. Zhang, X. Mao, Y. Yang, S. Yang, W. Zhao, T. Wumaier, D. Wei, W. Deng, K. Han, *Angew. Chem., Int. Ed.* **2019**, *58*, 2725.

© 2021 The Authors. Advanced Materials published by Wiley-VCH GmbH

Other Publications

I co-authored the following publications during my graduate studies.

K. Kroth, **P. Klement**, L. Chen, S. Chatterjee, and P. J. Klar
Microscopic Origin of Near- and Far-Field Contributions to Tip-Enhanced Optical Spectra of Few-Layer MoS_2
Nanoscale **13**, 17116 (2021). DOI: 10.1039/d1nr02987h

N. Dehnhardt, J.-N. Luy, **P. Klement**, L. Schipplick, S. Chatterjee, R. Tonner, and J. Heine
Mixed Group 14-15 Metalates As Model Compounds For Doped Lead Halide Perovskites
Angewandte Chemie International Edition **60**, 3906 (2021). DOI: 10.1002/ange.202014696

P. Cop, E. Celik, K. Hess, Y. Moryson, **P. Klement**, M. T. Elm, and B. M. Smarsly
Atomic Layer Deposition of Nanometer-Sized CeO_2 Layers in Ordered Mesoporous ZrO_2 Films and Their Impact on the Ionic/Electronic Conductivity
ACS Applied Nano Materials **3**, 11, 10757−10766 (2020). DOI: 10.1021/acsanm.0c02060

N. Dehnhardt, **P. Klement**, S. Chatterjee, and J. Heine
Divergent Optical Properties in an Isomorphous Family of Multinary Iodido Pentelates
Inorganic Chemistry **58**, 10983–10990 (2019). DOI: 10.1021/acs.inorgchem.9b01466

P. Hille, F. Walther, **P. Klement**, J. Müßener, J. Schörmann, J. Kaupe, S. Mitić, N. W. Rosemann, S. Chatterjee, A. Beyer, K. I. Gries, K. Volz, and M. Eickhoff
Influence of the atom source operating parameters on the structural and optical properties of $In_xGa_{1-x}N$ nanowires grown by plasma-assisted molecular beam epitaxy
Journal of Applied Physics **124**, 165703 (2018). DOI: 10.1063/1.5050391

References

1. Krömer, H. Quasi-Electric Fields and Band Offsets: Teaching Electrons New Tricks (Nobel Lecture). *Int. J. Mod. Phys. B* **16**, 677–697 (2002).

2. Novoselov, K. S. *et al.* Electric Field Effect in Atomically Thin Carbon Films. *Science* **306**, 666–669 (2004).

3. Novoselov, K. S. *et al.* Two-Dimensional Atomic Crystals. *PNAS* **102**, 10451–10453 (2005).

4. Novoselov, K. S. *et al.* A Roadmap for Graphene. *Nature* **490**, 192–200 (2012).

5. Tan, C. *et al.* Recent Advances in Ultrathin Two-Dimensional Nanomaterials. *Chem. Rev.* **117**, 6225–6331 (2017).

6. Mak, K. F. & Shan, J. Photonics and Optoelectronics of 2D Semiconductor Transition Metal Dichalcogenies. *Nat. Photonics* **10**, 216–226 (2016).

7. Low, T. *et al.* Polaritons in Layered Two-Dimensional Materials. *Nat. Mater.* **16**, 182–194 (2017).

8. Xi, X. *et al.* Strongly Enhanced Charge-Density-Wave Order in Monolayer $NbSe_2$. *Nat. Nanotechnol.* **10**, 765–769 (2015).

9. Teng, Z. *et al.* Edge-Functionalized g-C_3N_4 Nanosheets as a Highly Efficient Metal-Free Photocatalyst for Safe Drinking Water. *Chem* **5**, 664–680 (2019).

10. Ross, J. S. *et al.* Electrically Tunable Excitonic Light-Emitting Diodes Based on Monolayer WSe_2 p-n Junctions. *Nat. Nanotechnol.* **9**, 268–272 (2014).

11. Pospischil, A., Furchi, M. M. & Mueller, T. Solar-Energy Conversion and Light Emission in an Atomic Monolayer p-n Diode. *Nat. Nanotechnol.* **9**, 257–261 (2014).

12. Nicolosi, V., Chhowalla, M., Kanatzidis, M. G., Strano, M. S. & Coleman, J. N. Liquid Exfoliation of Layered Materials. *Science* **340**, 72–75 (2013).

13. Jin, E. *et al.* Designed Synthesis of Stable Light-Emitting Two-Dimensional sp^2 Carbon-Conjugated Covalent Organic Frameworks. *Nat. Commun.* **9**, 1–10 (2018).

14. Rodríguez-San-Miguel, D., Amo-Ochoa, P. & Zamora, F. MasterChem: Cooking 2D-Polymers. *Chem. Commun.* **52**, 4113–4127 (2016).

15. López-Cabrelles, J. *et al.* Isoreticular Two-Dimensional Magnetic Coordination Polymers Prepared Through Pre-synthetic Ligand Functionalization. *Nat. Chem.* **10**, 1001–1007 (2018).

16. Dou, L. *et al.* Atomically Thin Two-Dimensional Organic-Inorganic Hybrid Perovskites. *Science* **349**, 1518–1521 (2015).

17. Yaffe, O. *et al.* Excitons in Ultrathin Organic-Inorganic Perovskite Crystals. *Phys. Rev. B* **92**, 1–7 (2015).

18. Zhang, Q., Chu, L., Zhou, F., Ji, W. & Eda, G. Excitonic Properties of Chemically Synthesized 2D Organic–Inorganic Hybrid Perovskite Nanosheets. *Adv. Mater.* **30**, 1–8 (2018).

19. Xu, X., Yao, W., Xiao, D. & Heinz, T. F. Spin and Pseudospins in Layered Transition Metal Dichalcogenides. *Nat. Phys.* **10**, 343–350 (2014).

20. Kolobov, A. V. & Tominaga, J. *Two-Dimensional Transition-Metal Dichalcogenides*. (Springer International Publishing, 2016).

21. Kuc, A., Zibouche, N. & Heine, T. Influence of Quantum Confinement on the Electronic Structure of the Transition Metal Sulfide TS_2. *Phys. Rev. B* **83**, 1–4 (2011).

22. Mak, K. F., Lee, C., Hone, J., Shan, J. & Heinz, T. F. Atomically Thin MoS_2: A New Direct-Gap Semiconductor. *Phys. Rev. Lett.* **105**, 2–5 (2010).

23. Saparov, B. & Mitzi, D. B. Organic–Inorganic Perovskites: Structural Versatility for Functional Materials Design. *Chem. Rev.* **116**, 4558–4596 (2016).

24. Zhang, F. *et al.* Advances in Two-Dimensional Organic-Inorganic Hybrid Perovskites. *Energy Environ. Sci.* **13**, 1154–1186 (2020).

25. Shi, E. *et al.* Two-Dimensional Halide Perovskite Nanomaterials and Heterostructures. *Chem. Soc. Rev.* **47**, 6046–6072 (2018).

26. Even, J. *et al.* Solid-State Physics Perspective on Hybrid Perovskite Semiconductors. *J. Phys. Chem. C* **119**, 10161–10177 (2015).

27. Straus, D. B. & Kagan, C. R. Electrons, Excitons, and Phonons in Two-Dimensional Hybrid Perovskites: Connecting Structural, Optical, and Electronic Properties. *J. Phys. Chem. Lett.* **9**, 1434–1447 (2018).

28. Ishihara, T., Takahashi, J. & Goto, T. Optical properties due to electronic transitions in two-dimensional semiconductors $(C_nH_{2n+1}NH_3)_2PbI_4$ *Phys. Rev. B* **42**, 11099–11107 (1990).

29. Mueller, T. & Malic, E. Exciton Physics and Device Application of Two-Dimensional Transition Metal Dichalcogenide Semiconductors. *npj 2D Mater. Appl.* **2**, 1–12 (2018).

30. Klingshirn, C. F. *Semiconductor Optics*. (Springer Berlin Heidelberg, 2012).

31. Haug, H. & Koch, S. W. *Quantum Theory of the Optical and Electronic Properties of Semiconductors*. vol. 4 (World Scientific, 2009).

32. Keldysh, L. Coulomb Interaction in Thin Semiconductor and Semimetal Films. *J. Exp. Theor. Phys. Lett.* **29**, 11, 658–660 (1979).

33. Raja, A. *et al.* Coulomb Engineering of the Bandgap and Excitons in Two-Dimensional Materials. *Nat. Commun.* **8**, 1–7 (2017).

34. Mathieu, H., Lefebvre, P. & Christol, P. Simple Analytical Method for Calculating Exciton Binding Energies in Semiconductor Quantum Wells. *Phys. Rev. B* **46**, 4092–4101 (1992).

35. Chernikov, A. *et al.* Exciton Binding Energy and Nonhydrogenic Rydberg Series in Monolayer WS_2. *Phys. Rev. Lett.* **113**, 1–5 (2014).

36. Stier, A. V., Wilson, N. P., Clark, G., Xu, X. & Crooker, S. A. Probing the Influence of Dielectric Environment on Excitons in Monolayer WSe_2: Insight from High Magnetic Fields. *Nano Lett.* **16**, 7054–7060 (2016).

37. Steinke, C., Wehling, T. O. & Rösner, M. Coulomb-Engineered Heterojunctions and Dynamical Screening in Transition Metal Dichalcogenide Monolayers. *Phys. Rev. B* **102**, 1–10 (2020).

38. Mak, K. F. *et al.* Tightly Bound Trions in Monolayer MoS_2. *Nat. Mater.* **12**, 207–211 (2013).

39. Rhodes, D., Chae, S. H., Ribeiro-Palau, R. & Hone, J. Disorder in Van der Waals Heterostructures of 2D Materials. *Nat. Mater.* **18**, 541–549 (2019).

40. Ross, J. S. *et al.* Electrical Control of Neutral and Charged Excitons in a Monolayer Semiconductor. *Nat. Commun.* **4**, 1473–1476 (2013).

41. You, Y. *et al.* Observation of Biexcitons in Monolayer WSe_2. *Nat. Phys.* **11**, 477–481 (2015).

42. Blancon, J.-C. *et al.* Extremely Efficient Internal Exciton Dissociation Through Edge States in Layered 2D Perovskites. *Science* **355**, 1288–1292 (2017).

43. Hong, X., Ishihara, T. & Nurmikko, A. V. Dielectric Confinement Effect on Excitons in PbI4-based Layered Semiconductors. *Phys. Rev. B* **45**, 6961–6964 (1992).

44. Song, K. S. & Williams, R. T. *Self-Trapped Excitons*. vol. 105 (Springer Berlin Heidelberg, 1993).

45. Henderson, B. & Imbusch, G. F. *Optical Spectroscopy of Inorganic Solids*. (Oxford Science Publications, 2006).

46. Huang, K. & Rhys, A. Theory of Light Absorption and Non-Radiative Transitions in F-Centres. *Proc. R. Soc. London. Ser. A. Math. Phys. Sci.* **204**, 406–423 (1950).

47. Stadler, W. *et al.* Optical Investigations of Defects in $Cd_{1-x}Zn_xTe$. *Phys. Rev. B* **51**, 10619–10630 (1995).

48. Li, S., Luo, J., Liu, J. & Tang, J. Self-Trapped Excitons in All-Inorganic Halide Perovskites: Fundamentals, Status, and Potential Applications. *J. Phys. Chem. Lett.* **10**, 1999–2007 (2019).

49. Huang, Y. *et al.* Reliable Exfoliation of Large-Area High-Quality Flakes of Graphene and Other Two-Dimensional Materials. *ACS Nano* **9**, 10612–10620 (2015).

50. Blake, P. *et al.* Making Graphene Visible. *Appl. Phys. Lett.* **91**, 10–13 (2007).

51. Lee, C. *et al.* Anomalous Lattice Vibrations of Single- and Few-Layer MoS_2. *ACS Nano* **4**, 2695–2700 (2010).

52. Puurunen, R. L. Surface Chemistry of Atomic Layer Deposition: A Case Study for the Trimethylaluminum/Water Process. *J. Appl. Phys.* **97**, 121301 (2005).

53. Aarik, J., Aidla, A., Mändar, H. & Uustare, T. Atomic Layer Deposition of Titanium Dioxide from $TiCl_4$ and H_2O: Investigation of Growth Mechanism. *Appl. Surf. Sci.* **172**, 148–158 (2001).

54. Cop, P. *et al.* Atomic Layer Deposition of Titania in Ordered Mesoporous Cerium Zirconium Oxide Thin Films: A Case Study. *J. Phys. Chem. C* **123**, 12851–12861 (2019).

55. Mackus, A. J. M., Merkx, M. J. M. & Kessels, W. M. M. From the Bottom-Up: Toward Area-Selective Atomic Layer Deposition with High Selectivity. *Chem. Mater.* **31**, 2–12 (2019).

56. Mameli, A. *et al.* Area-Selective Atomic Layer Deposition of SiO_2 Using Acetylacetone as a Chemoselective Inhibitor in an ABC-Type Cycle. *ACS Nano* **11**, 9303–9311 (2017).

57. Knez, M. Diffusion Phenomena in Atomic Layer Deposition. *Semicond. Sci. Technol.* **27**, (2012).

58. Stevens, C. E. *et al.* Superradiant Coupling Effects in Transition-Metal Dichalcogenides. *Optica* **5**, 749 (2018).

59. Klement, P., Steinke, C., Chatterjee, S., Wehling, T. O. & Eickhoff, M. Effects of the Fermi Level Energy on the Adsorption of O_2 to Monolayer MoS_2. *2D Mater.* **5**, 045025 (2018).

60. Klement, P. *et al.* Surface Diffusion Control Enables Tailored-Aspect-Ratio Nanostructures in Area-Selective Atomic Layer Deposition. *ACS Appl. Mater. Interfaces* **13**, 19398–19405 (2021).

61. Klement, P. *et al.* Atomically Thin Sheets of Lead-Free 1D Hybrid Perovskites Feature Tunable White-Light Emission from Self-Trapped Excitons. *Adv. Mater.* **33**, (2021).

62. Utama, M. I. B. *et al.* A Dielectric-Defined Lateral Heterojunction in a Monolayer Semiconductor. *Nat. Electron.* **2**, 60–65 (2019).

63. Otto, F. Control of Spin-Split Excitons in Two-Dimensional Semiconductors by Extrinsic Dielectric Screening. (Justus-Liebig-Universität Gießen, 2019).

64. Hao, S., Bellus, M. Z., He, D., Wang, Y. & Zhao, H. Controlling Exciton Transport in Monolayer $MoSe_2$ by Dielectric Screening. *Nanoscale Horizons* **5**, 139–143 (2020).

65. Feng, J., Qian, X., Huang, C. W. & Li, J. Strain-Engineered Artificial Atom as a Broad-Spectrum Solar Energy Funnel. *Nat. Photonics* **6**, 866–872 (2012).

List of Figures

Figure 1	TMDC Crystal Structure	4
Figure 2	TMDC Band Structure	5
Figure 3	Perovskite Crystal Structure	6
Figure 4	Dielectric Screening in 2D Materials	8
Figure 5	Quasiparticle Transitions in TMDCs	10
Figure 6	Exciton Self-Trapping	12
Figure 7	Distinction of ALD & CVD	15
Figure 8	TiO2 ALD Process	16
Figure 9	Optical Spectroscopy Setups	20
Figure 10	Internal Interface Creation	25

Selbstständigkeitserklärung

Ich erkläre:

Ich habe die vorgelegte Dissertation selbstständig und ohne unerlaubte fremde Hilfe und nur mit den Hilfen angefertigt, die ich in der Dissertation angegeben habe. Alle Textstellen, die wörtlich oder sinngemäß aus veröffentlichten Schriften entnommen sind, und alle Angaben, die auf mündlichen Auskünften beruhen, sind als solche kenntlich gemacht. Ich stimme einer evtl. Überprüfung meiner Dissertation durch eine Antiplagiat-Software zu. Bei den von mir durchgeführten und in der Dissertation erwähnten Untersuchungen habe ich die Grundsätze guter wissenschaftlicher Praxis, wie sie in der „Satzung der Justus-Liebig-Universität Gießen zur Sicherung guter wissenschaftlicher Praxis“ niedergelegt sind, eingehalten.

Gießen, 05.06.2021 Philip Klement